REPORT DOCUMENTATION PAGE

Form Approved OMB NO. 0704-0188

The public reporting burden for this collection of information is estimated to average 1 hour per response, including the time for reviewing instructions, searching existing data sources, gathering and maintaining the data needed, and completing and reviewing the collection of information. Send comments regarding this burden estimate or any other aspect of this collection of information, including suggesstions for reducing this burden, to Washington Headquarters Services, Directorate for Information Operations and Reports, 1215 Jefferson Davis Highway, Suite 1204, Arlington VA, 22202-4302. Respondents should be aware that notwithstanding any other provision of law, no person shall be subject to any oenalty for failing to comply with a collection of information if it does not display a currently valid OMB control number.
PLEASE DO NOT RETURN YOUR FORM TO THE ABOVE ADDRESS.

1. REPORT DATE (DD-MM-YYYY)	2. REPORT TYPE	3. DATES COVERED (From - To)
04-09-2013	Ph.D. Dissertation	-

4. TITLE AND SUBTITLE

Ultra High Quality Factor Microtoroid for Chemical and Biomedical Sensing Applications

5a. CONTRACT NUMBER

W911NF-12-1-0026

5b. GRANT NUMBER

5c. PROGRAM ELEMENT NUMBER

611103

6. AUTHORS

Woosung Kim

5d. PROJECT NUMBER

5e. TASK NUMBER

5f. WORK UNIT NUMBER

7. PERFORMING ORGANIZATION NAMES AND ADDRESSES

Washington University
Research Office
276 North Skinker Bldg., 2nd Floor
St. Louis, MO   63130 -4899

8. PERFORMING ORGANIZATION REPORT NUMBER

9. SPONSORING/MONITORING AGENCY NAME(S) AND ADDRESS(ES)

U.S. Army Research Office
P.O. Box 12211
Research Triangle Park, NC 27709-2211

10. SPONSOR/MONITOR'S ACRONYM(S)

ARO

11. SPONSOR/MONITOR'S REPORT NUMBER(S)

58381-EL-PCS.7

12. DISTRIBUTION AVAILIBILITY STATEMENT

Approved for public release; distribution is unlimited.

13. SUPPLEMENTARY NOTES

The views, opinions and/or findings contained in this report are those of the author(s) and should not contrued as an official Department of the Army position, policy or decision, unless so designated by other documentation.

14. ABSTRACT

Optical whispering gallery mode (WGM) microcavities have drawn attentions in various types of sensing, such as chemical- and bio-sensing. Even though various types of microcavity geometries have been investigated, research about on-chip WGM toroidal resonator has been discontinued for the sensing applications in aquatic environment. The strong benefits of the microtoroid are ultra-high-Q and small mode volume leading to high sensitivity to small change of environment, surrounding media refractive index change or light scatterer induced effective refractive

15. SUBJECT TERMS

resonator, whispering gallery mode, biomedical sensing, nanoparticle

16. SECURITY CLASSIFICATION OF:			17. LIMITATION OF ABSTRACT	15. NUMBER OF PAGES	19a. NAME OF RESPONSIBLE PERSON
a. REPORT	b. ABSTRACT	c. THIS PAGE			Lan Yang
UU	UU	UU	UU		19b. TELEPHONE NUMBER
					314-935-9543

Report Title

Ultra High Quality Factor Microtoroid for Chemical and Biomedical Sensing Applications

ABSTRACT

Optical whispering gallery mode (WGM) microcavities have drawn attentions in various types of sensing, such as chemical- and bio-sensing. Even though various types of microcavity geometries have been investigated, research about on-chip WGM toroidal resonator has been discontinued for the sensing applications in aquatic environment. The strong benefits of the microtoroid are ultra-high-Q and small mode volume leading to high sensitivity to small change of environment, surrounding media refractive index change or light scatterer induced effective refractive index change. By using this ultra high-Q WGM resonator, radius >75nm polystyrene nanoparticle are detected in aquatic environment. In addition to polystyrene nanoparticle sensing, individual synthetic hemozoin crystals are detected and its size is measured. The hemozoin crystal sensing ultimately leads to malaria infection diagnose. A sol-gel method fabricated microlaser, co-work with Lina He, extended the sensing capability, detecting >30nm radius polystyrene nanoparticle. Since the water experiment is challenging and tackling the difficulty is main task, theoretical investigations are performed about WGM resonance quality factor, resonator mode volume, and noise to minimum detectable particle size. The research described in this dissertation will shed light on advanced chemical- and bio-sensor developments.

WASHINGTON UNIVERSITY IN ST. LOUIS

School of Engineering and Applied Science

Department of Electrical and Systems Engineering

Dissertation Examination Committee:
Lan Yang, Chair
ShiNung Ching
Viktor Gruev
Arye Nehorai
Srikanth Singamaneni
Lihong Wang

Ultra High Quality Factor Microtoroid for Chemical and Biomedical Sensing Applications

by

Woosung Kim

A dissertation presented to the
Graduate School of Arts and Sciences
of Washington University in
partial fulfillment of the
requirements for the degree
of Doctor of Philosophy

August 2013
St. Louis, Missouri

UMI Number: 3568202

UMI

Dissertation Publishing

UMI 3568202

ProQuest

Contents

List of Figures

Acknowledgments

Years in Prof. Lan Yang's lab at Washington University in St. Louis are unforgettable moment. It is impossible to express with few words how much I appreciate the exceptional support from my companions. I am able to obtain fruitful experience and knowledge for my Ph.D, and ultimately finish this dissertation, owing to the support.

Without question, Prof. Lan Yang is the first personnel I would appreciate. Pursuing Ph.D with Prof. Yang is incredible memory. I would say that the most difficult part of my Ph.D is to be patient. Especially, I have to admit that progress of bio-experiment is not proportional to how much effort is committed. Prof. Yang is the person who admits all the possible outcomes, good or bad. Ultimately, with her incredible support, I become an active independent thinker from a passive follower. I deeply appreciate her guidance, patience, and support.

I appreciate my Ph.D committee members, Prof. Arye Nehorai, Prof. Lihong Wang, Prof. Viktor Gruev, Prof. Srikanth Singamaneni, and Prof. ShiNung Ching, for their kind support and fruitful guidance.

I also appreciate fruitful and pleasant discussion with our incredible lab mates, Dr. Sahin Kaya Ozdemir, Dr. Jiangang Zhu, Dr. Lina He, Faraz Moni, Bo Peng, and Huzeyfe Yilmaz.

ABSTRACT OF THE THESIS

Ultra High Quality Factor Microtoroid for Chemical and Biomedical Sensing Applications

by

Woosung Kim

Doctor of Philosophy in Electrical Engineering

Washington University in St. Louis, 2013

Research Advisor: Professor Lan Yang

Optical whispering gallery mode (WGM) microcavities have drawn attentions in various types of sensing, such as chemical- and bio-sensing. Even though various types of microcavity geometries have been investigated, research about on-chip WGM toroidal resonator has been discontinued for the sensing applications in aquatic environment. The strong benefits of the microtoroid are ultra-high-Q and small mode volume leading to high sensitivity to small change of environment, surrounding media refractive index change or light scatterer induced effective refractive index change. By using this ultra high-Q WGM resonator, radius >75nm polystyrene nanoparticle are detected in aquatic environment. In addition to polystyrene nanoparticle sensing, individual synthetic hemozoin crystals are detected and its size is measured. The hemozoin crystal sensing ultimately leads to malaria

infection diagnose. A sol-gel method fabricated microlaser, co-work with Lina He, extended the sensing capability, detecting >30nm radius polystyrene nanoparticle. Since the water experiment is challenging and tackling the difficulty is main task, theoretical investigations are performed about WGM resonance quality factor, resonator mode volume, and noise to minimum detectable particle size. The research described in this dissertation will shed light on advanced chemical- and bio-sensor developments.

Chapter 1

Introduction

Note that all theoretical and experimental discussions are based on aquatic environment in this dissertation. Other environments, such as air, should be mentioned.

1.1   Overview

Biosensors using optical platforms have drawn remarkable attention in various applications, such as scientific research, healthcare, environmental monitoring, and homeland security [1]. Here I introduce two main optical biosensors categories, optical imaging using fluorescence [2] and resonance based label free sensing [3].

Underlying mechanism of the fluorescence is following [4]. Certain wavelength light emission is excited by the absorption of shorter wavelength light. The phenomenon, Stokes shift, is initiated by the interaction between donor and acceptor molecules, photon absorption and lower energy photon emission. However, fluorescence microscopy has main two difficulties. First, it requires time consuming labeling process which might affect functionality of the target molecule. Second, even though the imaging scheme claims single molecule sensitivity, labeling one-by-one is quite challenging. The difficulty of individual labeling leads to the challenge of quantitative analysis. On the other hands, resonance based label-free sensing scheme doesn't require

labeling. Since the detection is based on environmental refractive index change due to light-matter interaction, individual nanoscale-object binding or target object concentration can be quantified. State of the art of the resonance based label-free biosensing is to detect tens of nanometer scale individual nanoscale-objects.

This dissertation will be focused on nanoparticle sensing in water which is equivalent to label-free biosensing in terms of sensing mechanism with an optical microresonator. Further discussion covers hemozoin crystal detection for potential malaria infection diagnosis. Among many sensing methodologies [5-8], this dissertation will focus on the whispering gallery mode resonator based optical sensing. Even though the sensor system requires numerous efforts in various subjects, such as fluidics design, signal transducer, sensing surface immobilization, and post-processing, mainly signal transducer part, where light and nanoparticle interact, will be discussed.

1.2   Chapter outline

Chapter 2 introduces whispering gallery mode (WGM) optical microresonator. It introduces the overview of various geometries and coupling methodologies. Fundamental theories about resonance mode volume, quality factor, and coupling equation are overviewed. Main device used in this dissertation is a silica microtoroid. Fabrication process of the microtoroidis is also depicted.

Chapter 3 discusses two sensing schemes, WGM single resonance shift and resonance splitting. Detailed theories for these two schemes are introduced. As an application, this chapter introduces single nanoparticle sensing and size measurement experimental results. For certain portion of the description, single resonance shift theory cites Prof. Arnold's group work. Mode splitting based theory and experimental work in this chapter is carried out by Jiangang Zhu et al.

Chapter 4 discusses a Rayleigh scatterer induced WGM splitting in water, the fundamental sensing scheme. Theoretical work and experimental results are presented. First, theoretical comparison between two geometries of WGM microresonators, microsphere and microtoroid, is carried out. Second, experimental result of nanoparticle induced mode splitting with a microsphere in aquatic environment is introduced. Third, using a microtoroid, certain concentration nanoparticle solution induced mode splitting in water is observed.

Chapter 5 discusses individual hemozoin crystal sensing for potential malaria infection diagnosis. First, as a perquisite experiment, single nanoparticle detection and size measurement are performed. Detailed theory and experimental results are shown. Second, the individual synthetic hemozoin crystal is detected and its size is measured based on WGM splitting scheme. Briefly, sensing parameters of hemozoin crystal, $2g$ and Γ, is numerically studied for certain situations.

Chapter 6 is for computational investigation of rod-shape scatterer optical properties. The rod-shape is selected due to similarity with hemozoin crystal. Discrete dipole approximation (DDA) provides comprehensive tool to understand rod-shape scatterer. By using DDA, difference between TE and TM mode polarizabilities is investigated as a function of scatterer posture angle. Furthermore, with fixed posture scatterer, change of polarization from TE to TM mode influencing scatterer polarizability is studied.

Chapter 7 is for remark. In this chapter, summary of dissertation and potential future work are introduced.

Chapter 2

Whispering gallery mode microresonator and coupling

Historically, Lord Rayleigh first described the whispering gallery mode (WGM) phenomenon that acoustic waves travel around the interior of St. Paul's Cathedral [9]. The WGM can be also applied to light propagation within a spherical resonator [10]. In a WGM optical microresonator, light circulates along the curved boundary between the resonator material and the surrounding medium by near-ideal total internal reflection shown in Figure 2.1. In Figure 2.1 (a), light path inside of the circular structure is schematically depicted. Eigenmode which is supported by the circular structure is also shown in Figure 2.1 (b) obtained by COMSOL simulation. Various types of WGM resonators are shown in Figure 2.1 (c), sphere [11], disk [12], toroid [13], ring [14], tube [15], and bottle shapes [16], permission from [17]. Each shape has its own advantage and applications. For instance, microtoroid shape WGM resonator has high quality factor given smaller mode volume, which leads to higher sensing sensitivity compared to other geometries. In addition, various types of coupling methods are shown in Fig. 2.1 (d), permission from [17]. Also each coupling methodology has its own characteristics. In this dissertation, microtoroid and tapered fiber are used.
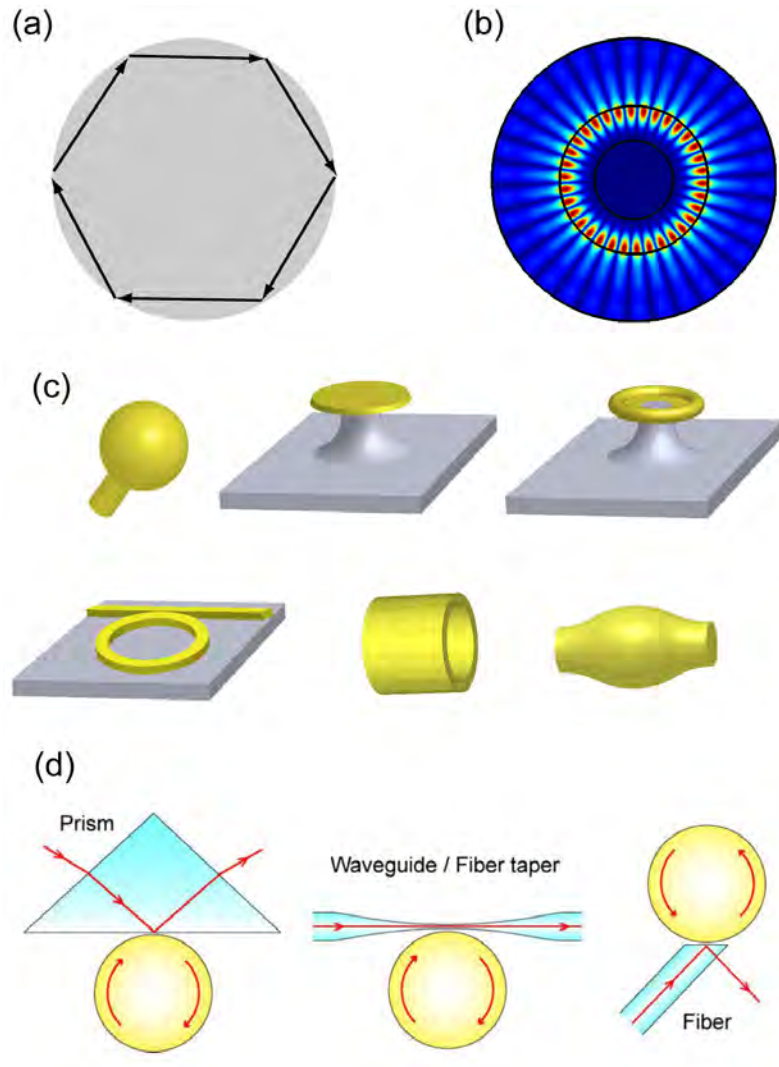
Figure 2.1. Schematics of WGM microresonator. (a) Total internal reflection illustration within a WGM microresonator. Light path is confined inside of the circular shape microresonator due to refractive index difference between resonator and environment. (b) Eigenmode illustration from COMSOL simulation. Electromagnetic field distribution is shown periodically confined inside of the WGM microresonator. (c) Various types of WGM resonators, permission from [17] (d) Various types of light in- and out-coupling schemes, permission from [17]

The WGM microresonator retains photon for long period of time, because of total internal reflection and low material loss. The long life time of photon results in narrow linewidth, and ultimately ultra high quality (Q) factor. The ultra high Q and small modevolume (V) of WGM resonators provide wide range of applications, such as optical filter [18], optical sensor [8, 19], frequency comb [20], and optical isolator [21]. Among these, enhanced light-matter interaction makes the detection of single nanoparticle possible [22]. Thus, optical WGM resonators have emerged as a promising sensing technology and have recently been under intensive investigation [8]. Fundamental theories of WGM microresonator and fabrication process of microtoroid are presented in this chapter.

2.1   Optical modes in WGM microsphere

Since analytical interpretation of the optical mode in a microtoroid is challenging, WGM microsphere optical mode is introduced for fundamental understanding of WGM. The modes of a spherical dielectric particle can be calculated by solving Helmholtz equation [23, 24]. A WGM micrsosphere shows propagating optical mode along its equator (Figure 2.2).
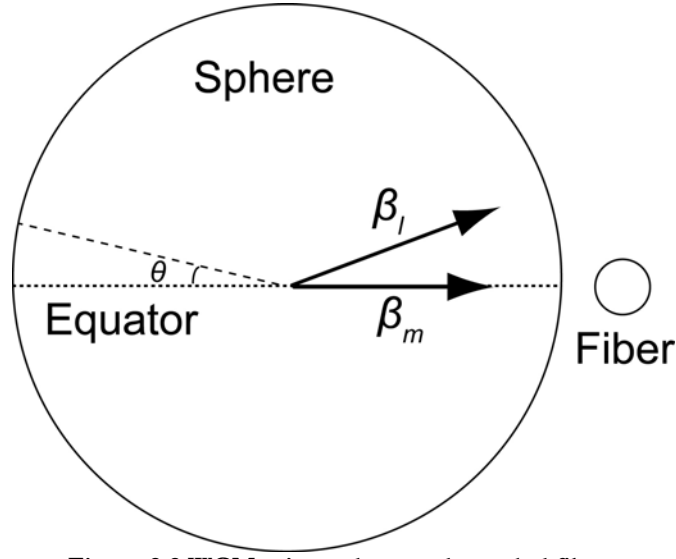
Figure 2.2.WGM microsphere and coupled fiber.

The propagating optical mode is excited by nearby coupled fiber. This dielectric microsphere has radius of R_0, homogeneous refractive index n_s, and it is surrounded by homogeneous environment n_0. Coordinates of the WGM microsphere are radial, r, azimuthal, φ, and polar directions, θ. The radius and refractive index of the fiber are defined as a and n, respectively. Mode numbers in this spherical coordinate are defined as l, m, n. Fundamental mode propagation constant, β_m, can be obtained from optical mode along the equator.

Under the assumption the direction of polarization is constant, optical modes are the separable solutions of Helmholtz equations in spherical coordinates. Outcome of this solution becomes spherical Bessel functions for radial axis, j_l, Eq. 2.2, and spherical harmonics in angular axis, H_N, Eq 2.3. The separable mode solution can be written as

$$\Psi_{l,m,n}(r, \theta, \phi) = N_s \psi_r(r) \psi_\theta(\theta) \psi_\phi(\phi) \qquad (2.1)$$

Individual components belonging to Eq. 2.1 also can be written as

$$\psi_r(r) = \begin{cases} j_l(kn_s r), & r \leq R_0 \\ j_l(kn_s R_0) exp[-\alpha(r - R_0)], & r > R_0 \end{cases} \qquad (2.2)$$

$$\psi_\theta(\theta) = exp\left[-\frac{m}{2}\theta^2\right] H_N(\sqrt{m}\theta) \qquad (2.3)$$

$$\psi_\phi(\phi) = exp[\pm jm\phi] \qquad (2.4)$$

$$N_S = \left\{ \sqrt{\frac{\pi}{m}} 2^{N-1} N! R_0^2 \left[\left(1 + \frac{1}{\alpha_s R_0}\right) j_l^2(kn_s R_0) - j_{l-1}(kn_s R_0) j_{l+1}(kn_s R_0) \right] \right\}^{-1/2} \qquad (2.5)$$

$$\alpha_s = \sqrt{\beta_l^2 - k^2 n_0^2} \qquad (2.6)$$

$$\beta_l = \sqrt{\frac{l(l+1)}{R_0}} \qquad (2.6)$$

$$N = l - m \qquad (2.7)$$

$$k = \frac{2\pi}{\lambda} \qquad (2.8)$$

2.2   Critical parameters for WGM resonator

For sensing capability analysis, WGM quality factor (Q) and mode volume (V) are critical parameters. Q factor is related with optical mode loss as written below.

$$Q_0 = \omega \frac{E_{stored}}{P_{diss}} \qquad (2.9)$$

, where ω is resonance frequency, E_{stored} is stored energy in WGM resonator, P_{diss} is dissipated power from the resonator. It can also be related with photon life time within the resonator, τ.

$$\tau = \frac{E_{stored}}{P_{diss}} \qquad (2.10)$$

Multiple factors are contributing to the comprehensive Q factor, Q_{total}, intrinsic material loss, Q_{ini}, surface scattering loss, Q_{scat}, surface absorption loss, Q_{abs}, radiation loss, Q_{rad}, and coupling loss, $Q_{coupling}$. Total Q factor is can be written as [11, 25-27]

$$Q_{total}^{-1} = Q_{ini}^{-1} + Q_{scat}^{-1} + Q_{abs}^{-1} + Q_{rad}^{-1} + Q_{coupling}^{-1} \qquad (2.11)$$

Material loss is material dependency of the resonator. Surface scattering loss comes from surface inhomogeneity due to imperfection fabrication process or environmental external effect. Absorption loss occurs due to presence of adsorbed water on the surface of resonator. Radiation loss is due to light bending at the curvature of the resonator, which is resonator radius dependent. Coupling loss is from external coupling

between resonator and coupling tool, such as waveguide bus or prism. In practical measurement, Q factor is measured by the combination of center resonance frequency and its linewidth (full width at half maximum), $Q = \frac{\omega}{\delta\omega}$.

Mode volume is another critical parameter for WGM resonator characterization. Because it determines how well light is confined given the size of resonator, it implies how responsive the confined light to environmental changes is. Even though there are multiple different definitions about the mode volume, in this dissertation typical WGM resonator mode volume definition will be used, shown in Eq. 2.12 [28, 29]. Mode volume indicates normalized optical mode energy by its maximum energy within the WGM resonator. It can be written as

$$V = \frac{\int \varepsilon(r)|\vec{E}(r)|^2 d^3 r}{max\left(\varepsilon(r)|\vec{E}(r)|^2\right)} \tag{2.12}$$

where $\varepsilon(r)$ is the resonator material permittivity and $|\vec{E}(r)|$ is the electric field in the resonator. For sensing application, smaller mode volume results in higher sensitivity given same Q factor, since more light is confined within a smaller volume. In other words, light-matter interaction is stronger in a small cavity compared to a large cavity. In physical interpretation, ratio of Q factor to mode volume, V, is related to Purcell factor ($\sim Q/V$). The Purcell effect is light spontaneous emission enhancement phenomenon when the emitter is in a cavity [30].

2.3   WGM microtoroid fabrication

SiO_2 microtoroid is fabricated by using a traditional lithography method [13]. Top SiO_2 2µm thickness layer supported by silicon pillar forms the SiO_2 microtoroid after the following fabrication process shown in Figure 2.3. Initially, with traditional photolithography, a layer of photoresist is spun coated, 3000rpm for 30sec shown in red layer in the Figure 2.3. 80~200µm in diameter circular pad is patterned with a photomask, UV exposure, and photoresist development, consequently. 2µm thickness SiO_2 layer is etched away by hydrofluoride (HF) for 15mins until the etching can be inspected by forming hydrophobic surface. Since refractive index of SiO_2, $n_{silica} = 1.54$, is lower than Si, $n_{silicon} = 3.49$, SiO_2 should be isolated from Si surface. Otherwise, light is leaked from SiO_2 to Si. In order to isolate SiO_2 layer from Si surface, XeF_2 gas etching is used. XeF_2 gas etching is isotropic etching and multiple iterations of gas etching and nitrogen purging generate undercut below SiO_2. Microdisk fabricated by the gas etching will turn to microtoroid by CO_2 reflow process. High power CO_2 laser smooth the SiO_2 surface and forms donut shape structure, microtoroid. Ultimate microtoroid shape is shown in Figure 2.4. From top view of it, major (D) and minor (d) diameters are defined as marked. Top of the microtoroid is tapered fiber for light coupling.
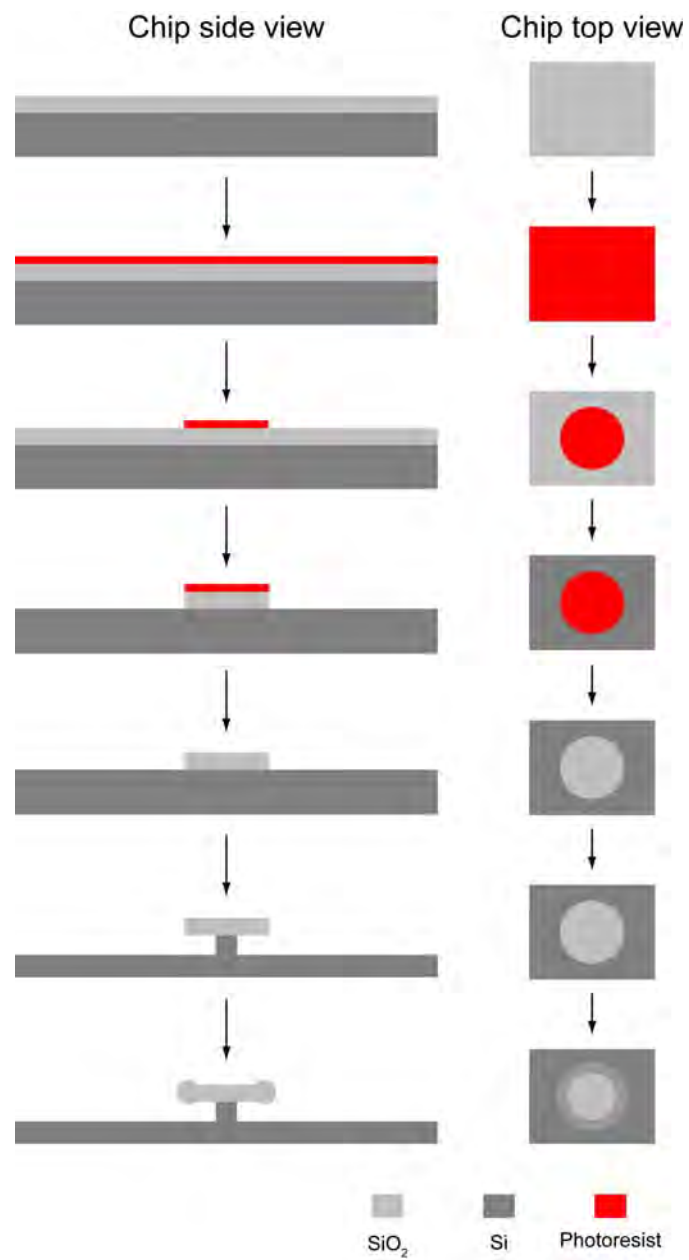
Figure 2.3.Microtoroid fabrication process
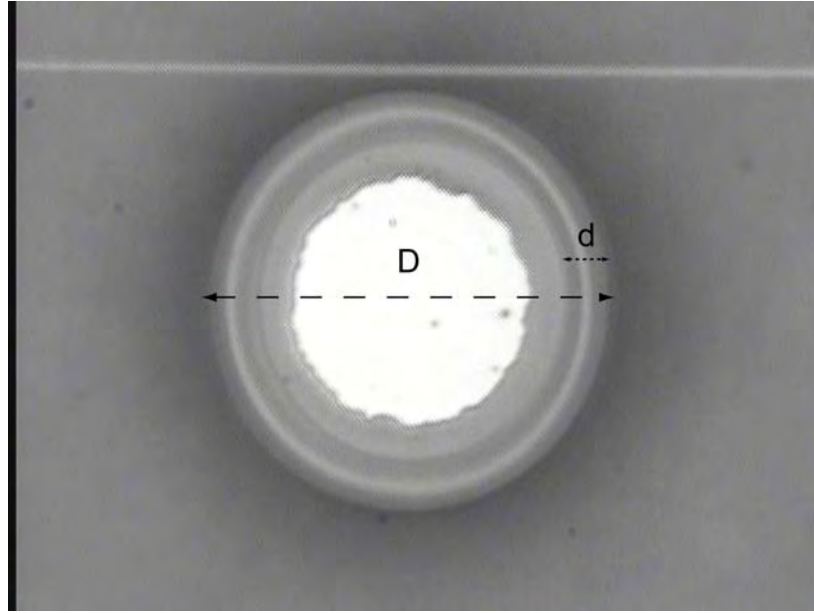
Figure 2.4. Microtoroid image

2.4   Three coupling regimes between tapered fiber and microtoroid

In this dissertation, light is coupled to silica toroid through tapered single mode fiber. Coupling between microtoroid and tapered fiber is shown in Figure 2.5 [31]. When the evanescence tailed light from the tapered fiber is proximate enough to microtoroid, the fundamental optical mode of the fiber will experience overlap of microtoroid WGM. Depending on the distance, coupling efficiency between WGM resonator and the tapered fiber alters. This coupling scheme has three different coupling regimes, under-coupling, over-coupling, and critical coupling [26, 32]. Here, let's discuss in which condition we would see a specific coupling regime.
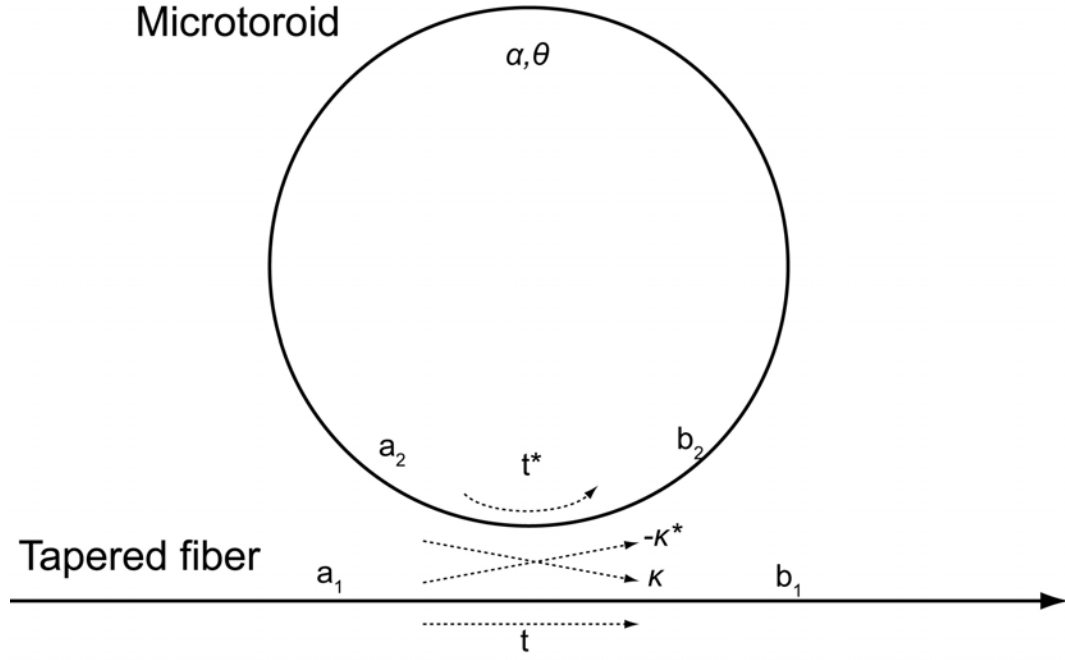
Figure 2.5.Coupling schematic between the tapered fiber and microtoroid. Each character is described in the text individually.

From Figure 2.5, I can describe a relationship between input and output complex amplitudes a_i and b_i as

$$\begin{vmatrix} b_1 \\ b_2 \end{vmatrix} = \begin{vmatrix} t & \kappa \\ -\kappa^* & t^* \end{vmatrix} \begin{vmatrix} a_1 \\ a_2 \end{vmatrix} \tag{2.13}$$

where t and κ are coupling coefficients in the direction of the arrows in Figure 2.5. Under the assumption that there is no additional power dissipation occurs at the coupling area, two coupling coefficients forms following equation.

$$|\kappa^2|+|t^2| = 1 \tag{2.14}$$

To be simplify the problem, we can set $a_1 = 1$, so that all other parameters are normalized to a_1. Coupled amplitude in microtoroid will experience phase shift and damping.

$$a_2 = \alpha e^{i\theta} b_2 \qquad (2.15)$$

α is damping rate of the amplitude and θ is phase shift at certain location of the microtoroid. We can obtain b_1 and a_2 based on Eq. 2.13~2.15

$$|b_1|^2 = \frac{\alpha^2+|t|^2-2\alpha|t|\cos{(\theta+\phi_t)}}{1+\alpha^2|t|^2-2\alpha|t|\cos{(\theta+\phi_t)}}, \; |a_2|^2 = \frac{\alpha^2(1-|t|^2)}{1-2\alpha|t|\cos(\theta+\phi_t)+\alpha^2|t|^2} \qquad (2.16)$$

where ϕ_t is phase shift of out-coupling region. When $(\theta + \phi_t) = 2\pi m$, resonance occurs. At the resonance, Eq. (2.16) becomes

$$|b_1|^2 = \frac{(\alpha-|t|)^2}{(1-\alpha|t|)^2}, \; |a_2|^2 = \frac{\alpha^2(1-|t|^2)}{(1-\alpha|t|)^2} \qquad (2.17)$$

A special case of that damping rate is equal to internal coupling rate, $\alpha = |t|$, output amplitude becomes zero, $|b_1| = 0$. This condition is known to be 'critical coupling', because of perfect destructive interference between transmitted field, ta_1 and internal field, κa_2.

In order to understand other coupling regime, external and intrinsic quality factors should be understood. The coupling relationship time course in the microtoroid can be written as

$$\frac{da_2}{dt} = -\left(i\omega_c + \frac{(\alpha+\kappa)}{2}\right)a_2 - \sqrt{\kappa}a_1 \qquad (2.18)$$

where ω_c is cavity resonance frequency. When the system reaches a steady-state, transmission is given as

$$|b_1|^2 = \frac{|a_1 + \sqrt{\kappa}a_2|^2}{|a_1|^2} = 1 - \frac{\alpha\kappa}{(\Delta\omega)^2 + \left(\frac{\alpha+\kappa}{2}\right)^2} \qquad (2.19)$$

where $\Delta\omega$ is the detuning frequency. From the Equation (2.19), we can extract intrinsic and external quality factors at the resonance condition, $\alpha = t$.

$$Q_0 = Q_{ex} = \frac{\omega_c}{\alpha} \qquad (2.20)$$

The three coupling regimes are defined as below.

(1) Under coupling regime: Distant location of tapered fiber from the cavity is not able to couple light into cavity. In this case, external quality factor is much bigger than intrinsic quality factor. Until these two quality factors are

matched each other, coupling regime is not reached yet to critical coupling. This coupling regime is defined as under coupling regime.

(2) Critical coupling regime: When intrinsic and external quality factors are equal shown as zero transmission power. It is defined as critical coupling regime.

(3) Over coupling regime: If the tapered fiber approaches closer than the critical coupling point, transmission comes back to non-zero. It occurs because tapered fiber and cavity modes overlap more and external quality factor decreases. It is defined as over coupling regime.

Chapter 3

Two main sensing schemes with WGM microresonator

In this chapter, I will introduce two main sensing schemes, single resonance shift and mode splitting. Single resonance shift is heavily studied in Prof. Arnold's group work [33]. Most of mode splitting sensing work is done in our lab [19].

3.1   Single resonance shift

The single resonance shift sensing scheme is fundamentally explained by change of light path length and refractive index. Underlying mechanism is similar to surface plasmon resonance sensing scheme [34]. In a simple form, resonance condition is satisfied as $m\lambda = 2\pi nR$, where R is effective radius of the light path and n is effective refractive index that light experiences. If effective refractive index of the environment changes, it affects resonance wavelength of the cavity. In case of changing light path length, it also results in different resonance wavelength. Thus, this relationship can be written as [3]

$$\frac{\Delta\lambda}{\lambda} = \frac{\Delta R}{R} + \frac{\Delta n_e}{n} \qquad (3.1)$$

Figure 3.1 shows representative cavity resonance before (a) and after (b) environmental change. In this example, environmental change induces resonance frequency red-shift, which indicates either increased effective radius of light path or/and effective refractive index.
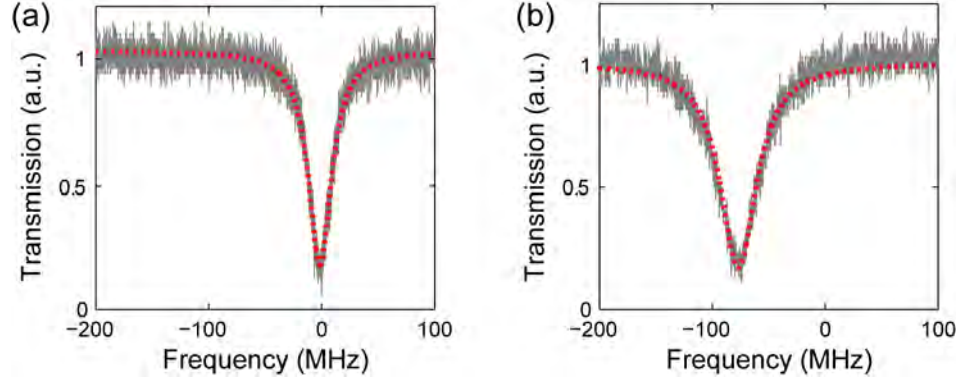
Figure 3.1. Single resonance frequency shift. (a) Before and (b) after environmental change, transmission shows cavity resonance frequency

When it is employed to nanoparticle sensing, single resonance frequency shift is explained by overall dissipated energy to a nanoparticle.

$$\hbar \Delta\omega \cong -\frac{\alpha_{ex}}{2}\langle E(r,t)^2 \rangle \qquad (3.2)$$

, where $\Delta\omega$ is resonance shift, α_{ex} is the single nanoparticle polarizability, $E(r,t)^2$ is the averaged electric field square at the location of the nanoparticle. Equation (3.2) can be expressed as frequency shifted energy compared to total energy.

$$\left(\frac{\Delta\omega}{\omega}\right) \cong \frac{-\alpha_{ex}|E(r)|^2}{2\varepsilon_0 \int \varepsilon(r)|E(r)|^2 dV} \qquad (3.2)$$

20

, where ε is dielectric constant of the vacuum and at the location of the nanoparticle.

Thus, resonance frequency shift shows partial change of energy compared to overall energy. In special conditions, the nanoparticle size can be extracted. The special conditions are maximum resonance shift and known microsphere size. If the resonance shift is the maximum, particle size can be known.

$$r_0 \cong \sqrt[3]{\frac{(n_s^2-n_m^2)(n_p^2+2n_m^2)}{2n_m^2(2n_s)^{1/2}(n_p^2-n_m^2)}} R^{5/6}\lambda^{1/6}\left(\frac{\Delta\lambda}{\lambda}\right)_{max}^{1/3} \qquad (3.2)$$

, where n_s is microsphere refractive index, n_m is environmental refractive index, n_p is the particle refractive index, and R is the microsphere radius.

However, particle size measurement based on single resonance frequency shift has a limitation, because it depends on maximum shift. Simply, what is the percentage to see maximum resonance shift out of 100 particle binding events? Even we concluded it is maximum resonance shift, is it possible to see larger amount of shift with newly upcoming nanoparticles?

Here, I introduce the statistical possibility to observe maximum resonance shift. This computational study is based on the following conditions, 46µm radius silica

microsphere, 660nm wavelength laser, and 80nm radius polystyrene nanoparticle. In order to compute possible resonance shift range upon binding of nanoparticle, field maximum and minimum on a microsphere are obtained from COMSOL simulation. Maximum frequency shift according to the COMSOL simulation result shows 76.6 fm. Given the frequency shift range, 10000 binding events are randomly tried. Out of ten thousand trials, maximum observed resonance shift is recorded. This procedure is repeated multiple times, called as observations. Figure 3.2 shows variation of nanoparticle size estimation, depending on various factors. Figure 3.2 (a) shows that arbitrary observation refreshes resonance frequency maximum shift. In other words, maximum frequency shift that is defined in an observation of ten thousand times of binding events is no longer maximum frequency shift, if another observation shows bigger frequency shift. In accordance to the figure, in this specific situation at least 150 independent observations should be performed so that more accurate maximum shift should be observed, 76.6 fm. Furthermore, within an observation, multiple binding events increase overall resonance frequency shift, implicating continuously changing reference resonance frequency, shown in Figure 3.2 (b). It means that instability of the reference frequency can cause a problem, if the reference frequency becomes beyond free spectral range. Figure 3.2 (c) shows the variation of saturation observation in order to have the maximum shift. In other words, how many observations are required to detect actual maximum frequency shift depending on threshold level. This threshold level means arbitrary decision level based on theoretical maximum shift. For example, lower threshold requires less observation for the maximum shift. Lastly, Figure 3.2 (d) shows nanoparticle radius estimation based on the resonance frequency maximum shift.

Thus, the nanoparticle size measurement requires comprehensive understanding of the parameters and number of the independent experiments (observations). Otherwise, size estimation is always in question.
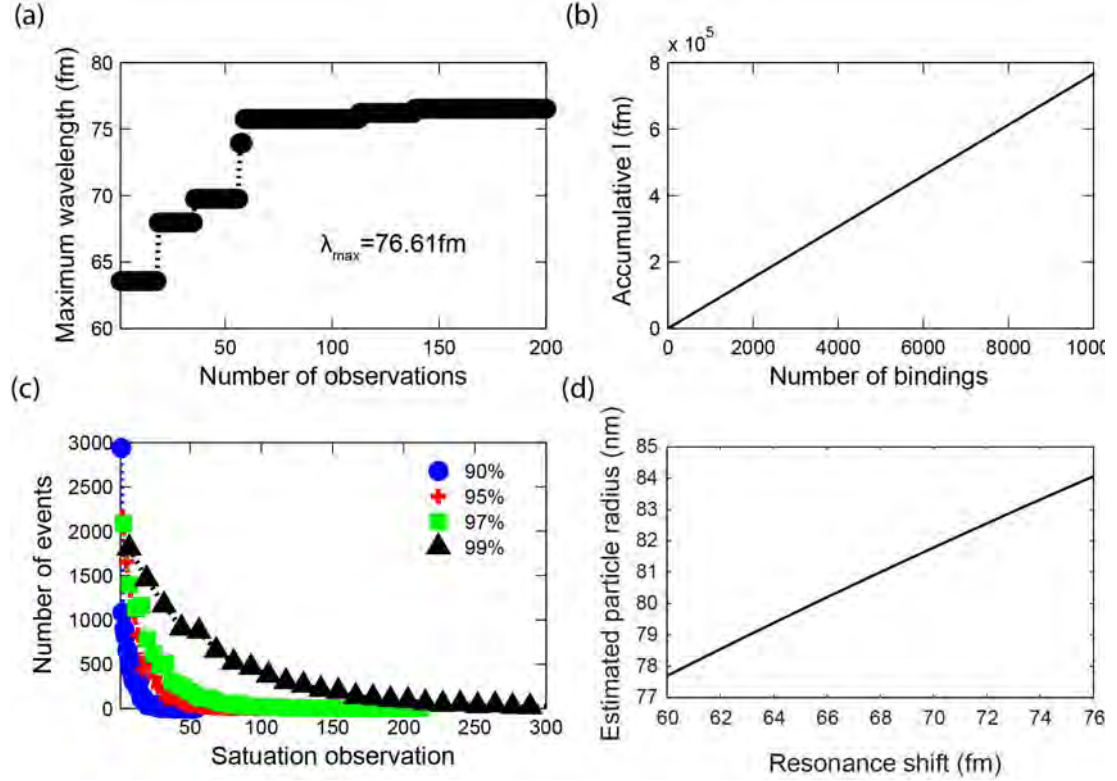
Figure 3.2. Maximum resonance shift statistics. (a) Maximum resonance frequency shift out of ten thousand unbiased random binding events is updated in each observation. Until ~150 observations, real maximum resonance shift is not captured. (b) Accumulative resonance shift as a function of number of observations shows ascending relationship. It indicates that reference resonance frequency is instable so that decision making of maximum shift be challenging. (c) A relationship between number of observations and maximum shift depending on threshold level is shown. Lower threshold for maximum shift decision shows faster termination of observation. (d) Nanoparticle radius estimation based on the observed maximum shift.

Another limitation of the resonance frequency maximum shift based nanoparticle size estimation is upon resonance mode volume information. It requires explicit mode volume information, which is feasible for microsphere platform. However, it is challenging for other sensing platform, such as microtoroid, because of lack of analytical understanding of it. Due to this reason, a study that claims single particle size estimation based on the maximum resonance frequency shift with a microtoroid is questionable [35].

To clarify the role of the microtoroid size for nanoparticle size measurement accuracy by using maximum resonance shift method, I performed a series of simulations and depicted the results in Figure 3.3. COMSOL simulations are performed to estimate the resonance frequencies and the mode volumes for various size microtoroids. Each particle is assumed to be on the mode maxima of the mocrotoroid and the maximum spectral shift is obtained. The maximum resonance shift is used for further processing. Note that the particle is assumed to be polystyrene ($n = 1.45$) and all values are averaged ones from minor diameters, $3\sim6\mu m$. Figure 3.3 (a) depicts that the maximum spectral shift decreases as the major diameter of microtoroid increases with different decay rate depending on the particle size. I find that a relationship between the microtoroid major diameter D and the maximum shift $\Delta\lambda_{max}$ can be a function, $\Delta\lambda_{max} \propto aD^{-b}10^{-6}$. The parameter b shows slight variation depending on particle size; however, I could not observe a significant change in $\Delta\lambda_{max}$ with the parameter variation. Thus, within the reasonable range of b, I take $b = 2.017$. On the other hand,

the parameter a is a function of the particle size and strongly affects $\Delta\lambda_{max}$. Through curve fitting, I find that particle size dependency of a can be $a(R) = 1.87 \times R^3$ (Figure 3.3 (b)). For example, polystyrene particles of R=90nm results in $a = 1.36 \times 10^{-21}$ and $b = 2.017$. Putting all together, I arrive at the expression $\Delta\lambda_{max} = 1.87 \times R^3 \times D^{-2.017} 10^{-6} (fm)$ for the maximum shift induced by a particle of radius R deposited on a microtoroid of major diameter, D. Figure 3.3 (c) depicts overall dependency from the obtained function. Thus, to estimate particle size information from the observed maximum shift, one needs to know the microtoroid size and should have enough data to be statistically confident that the measured maximum shift represents the actual maximum shift. Only with the sufficient conditions, one can use this expression to estimate the particle size.
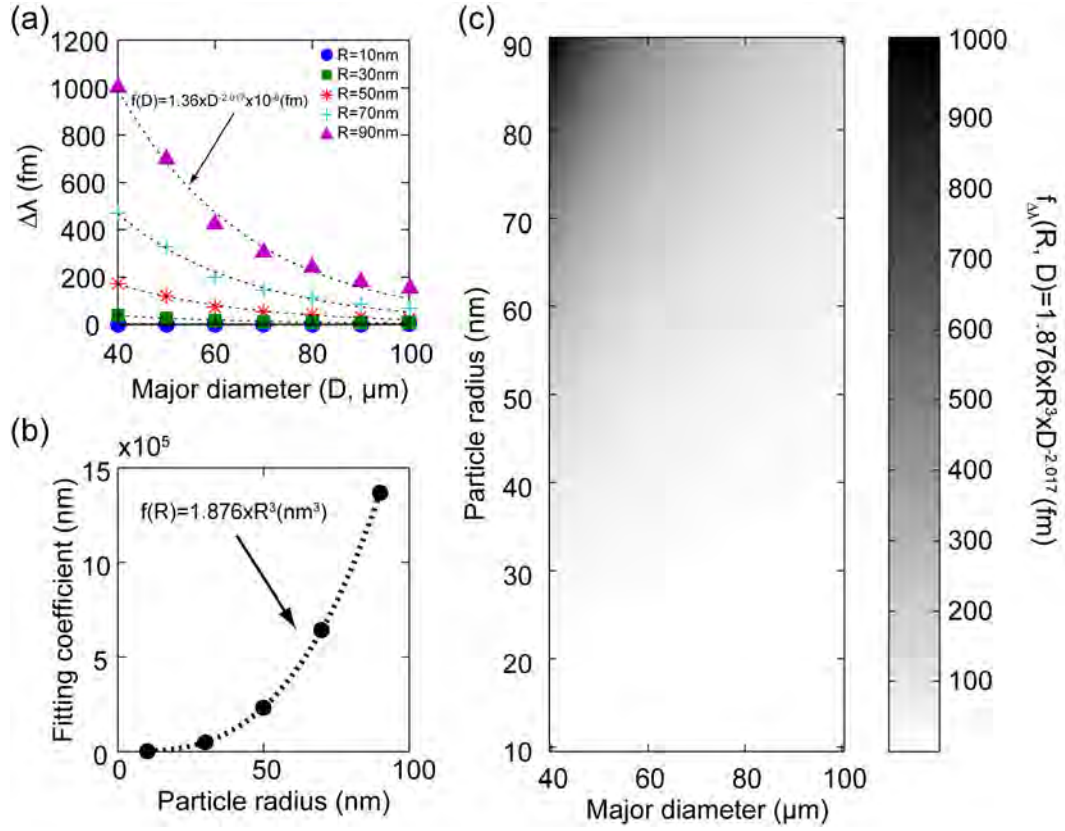
Figure 3.3. Maximum frequency shift dependency to particle size and mirotoroid major diameter. (a) Maximum resonance frequency shift varies depending on particle radius and microtoroid diameter. (b) Given a specific microtoroid major diameter, maximum resonance frequency shift shows a relationship as a function of nanoparticle size. (c) Overall maximum resonance shift with a microtoroid is governed by a function of microtoroid major diameter and nanoparticle radius.

3.2   Mode splitting

3.2.1 Scatterer polarizability

The mode splitting is induced by a scatterer [19, 36]. The scatterer lifts up WGM into two different resonance frequencies. The observed mode splitting transmission line can be characterized by coupling strength $2g$ and additional loss Γ, which are related with polarizability of the scatterer. Thus, prior to introducing the theories and experimental works, polarizability of the scatterer needs to be studied [37, 38].

First of all, it should start from electrostatics boundary-value problem. Non-charge environment Laplace equation in spherical coordinates (r, θ, ϕ) can be written as

$$\frac{1}{r}\frac{\partial^2}{\partial r^2}(r\Phi) + \frac{1}{r^2 sin\theta}\frac{\partial}{\partial\theta}\left(sin\theta\frac{\partial\Phi}{\partial\theta}\right) + \frac{1}{r^2 sin\theta}\frac{\partial^2\Phi}{\partial\phi^2} = 0 \qquad (3.3)$$

The potential can be written as follow, under the assumption that the potential is a separable form

$$\Phi = \frac{U(r)}{r}P(\theta)Q(\phi) \qquad (3.4)$$

From the Laplace equation in (3.3), by substituting (3.4) and multipling $r^2\frac{sin^2\theta}{UPQ}$, we can obtain the following equation

$$r^2 sin^2\theta\left[\frac{1}{U}\frac{\partial^2 U}{\partial r^2} + \frac{1}{Pr^2 sin\theta}\frac{\partial}{\partial\theta}\left(sin\theta\frac{\partial P}{\partial\theta}\right)\right] + \frac{1}{Q}\frac{\partial^2 Q}{\partial\phi^2} = 0 \qquad (3.5)$$

27

Since ϕ dependence is isolated, we can set $\frac{1}{Q}\frac{\partial^2 Q}{\partial\phi^2} = -m^2$. Consequently, the solution

becomes $Q = e^{\pm im\phi}$. Another isolation can be led by setting r dependence as $\frac{1}{U}\frac{\partial^2 U}{\partial r^2} =$

$\frac{l(l+1)}{r}$. It has the solution $U = Ar^{l+1} + Br^l$. Only θ dependence is remained, with

following equation

$$\frac{1}{sin\theta}\frac{\partial}{\partial\theta}\left(sin\theta\frac{\partial P}{\partial\theta}\right) + \left[l(l+1) - \frac{m^2}{sin^2\theta}\frac{\partial P}{\partial\theta}\right] = 0 \qquad (3.6)$$

The equation (3.6) is Legendre equation. The equation has solution, $P_l(x) =$

$\frac{1}{2^l l!}\frac{\partial^l}{\partial x^l}(x^2 - 1)^l$, here, $x = cos\theta$.

For simplicity, we can consider azimuthal symmetry, $m = 0$. Thus, general solution of

the Laplace equation, (3.3), becomes

$$\phi(r,\theta) = \sum_{l=0}^{\infty}\left[A_l r^l + B_l r^{-(l+1)}\right]P_l(cos\theta) \qquad (3.7)$$

Now, let's consider our dielectric sphere (permittivity: ε_p) problem with radius a in an

environment (permittivity: ε_e) with uniform electric field, E_0. This problem should start

from defining the inside and outside potentials. Since the potential inside shoud be

finite, B_l should be 0 for all l. Thus, inside and outside potentials are defined as

following:

$$\phi_{in}(r, \theta) = \sum_{l=0}^{\infty} A_l r^l P_l(cos\theta) \qquad (3.8)$$

$$\phi_{out}(r, \theta) = \sum_{l=0}^{\infty} \left[C_l r^l + D_l r^{-(l+1)} \right] P_l(cos\theta) \qquad (3.9)$$

At infinity, potential becomes $\phi = -E_0 r cos\theta = -E_0 r P_l(cos\theta)$. Then, we find that the only nonvanishing C_l is $C_1 = -E_0$. A and D can be determined by boundary condition at $r = a$,

$$\text{Tangential: } \frac{\partial \phi_{in}}{\partial \theta}\bigg|_{r=a} = \frac{\partial \phi_{out}}{\partial \theta}\bigg|_{r=a} \qquad (3.10)$$

$$\text{Normal: } \varepsilon_p \frac{\partial \phi_{in}}{\partial r}\bigg|_{r=a} = \varepsilon_e \frac{\partial \phi_{out}}{\partial r}\bigg|_{r=a} \qquad (3.11)$$

From (3.10-3.11), we can obtain, A and D

$$A_1 = -E_0 + \frac{D_1}{a^3} \qquad (3.12)$$

$$A_l = \frac{D_l}{a^{2l+1}}, l \neq 1 \qquad (3.13)$$

$$\frac{\varepsilon_p}{\varepsilon_e} A_1 = -E_0 + \frac{D_1}{a^3} \qquad (3.14)$$

$$\frac{\varepsilon_p}{\varepsilon_e} l A_l = -(l+1)\frac{D_l}{a^{2l+1}}, l \neq 1 \qquad (3.15)$$

Since $l \neq 1$ leads $A_l = D_l = 0$, remaining coeffiecients are A_1 and D_1. Therefore, if we organize the coefficients with E_0, the potentials become

$$\phi_{in}(r,\theta) = -\frac{3\varepsilon_e}{\varepsilon_p+2\varepsilon_e}E_0 r cos\theta \qquad (3.16)$$

$$\phi_{out}(r,\theta) = -E_0 r cos\theta + \frac{\varepsilon_p-\varepsilon_e}{\varepsilon_p+2\varepsilon_e}E_0\frac{a^3}{r^2}cos\theta \quad (3.17)$$

Equation (3.16) provides a constant electric field parallel to to the applied field

$$E_{in} = \frac{3\varepsilon_e}{\varepsilon_p+2\varepsilon_e}E_0 \qquad (3.18)$$

Polarization $P = (\varepsilon_p - \varepsilon_e)E_{in} = 3\varepsilon_e\frac{\varepsilon_p-\varepsilon_e}{\varepsilon_p+2\varepsilon_e}E_0$ leads to the dipole moment,

$$p = \frac{4}{3}\pi R^3 P = 4\pi R^3 \varepsilon_e\frac{\varepsilon_p-\varepsilon_e}{\varepsilon_p+2\varepsilon_e}E_0. \qquad (3.19)$$

The molecular polizability, α, is defined as the ratio of the dipole moment to ε_0 times the applied field, E_0. Thus, the polizability becomes

$$\alpha = 4\pi R^3\frac{\varepsilon_e}{\varepsilon_0}\frac{\varepsilon_p-\varepsilon_e}{\varepsilon_p+2\varepsilon_e} \qquad (3.20)$$

3.2.2 Mode splitting mechanism

Presence of a Rayleigh scatterer, which radius is smaller than wavelengh, within a range of the cavity field evanescent tail results in mode splitting. Here, I introduce the fundamental mechanism of the mode splitting sensing scheme [19, 25, 36, 39].
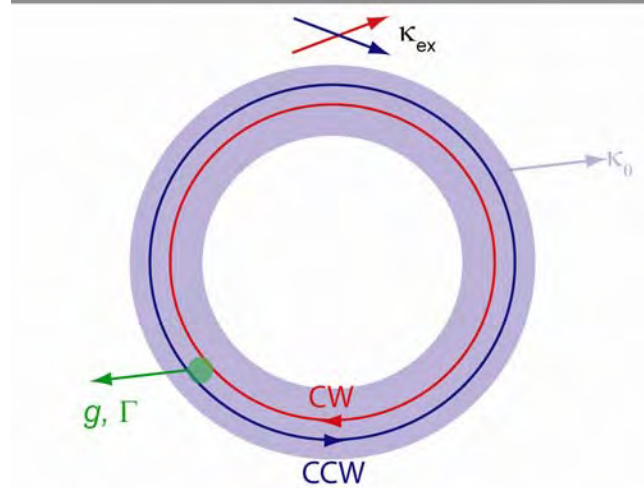
Figure 3.4. Schematic of WGM two degenerate modes. CW is clockwise, CCW is counter clock-wise, κ_0 is WGM intrinsic damping rate, κ_{ex} is coupling damping rate, g is coupling strength between CW and CCW modes, Γ is additional damping due to the Rayleigh scatterer, depicted as green circle.

The WGM resonator is capable of supporting two degenerate modes shown in Figure 3.4, which share resonance frequency, mode volume, and other properties, except propagation directionality. One propagates clock-wise and other is on counter clock-wise. Once nanoparticle enters into the mode volume, two degenerate modes start to couple each other. The two degenerate modes, a_{CW} and a_{CCW}, have following rate equations [40],

$$\frac{da_{cw}}{dt} = -\left[-i(\omega_c + g) + \frac{\Gamma+\kappa_0+\kappa_1}{2}\right]a_{cw} - \left(\frac{\Gamma}{2} + ig\right)a_{ccw} - \sqrt{\kappa_1}a_{cw}^{in} \qquad (3.21)$$

$$\frac{da_{ccw}}{dt} = -\left[-i(\omega_c + g) + \frac{\Gamma+\kappa_0+\kappa_1}{2}\right]a_{ccw} - \left(\frac{\Gamma}{2} + ig\right)a_{cw} - \sqrt{\kappa_1}a_{ccw}^{in} \qquad (3.22)$$

, where $\kappa_0 = \frac{c}{Q_0}$ is intrinsic damping rate due to intrinsic property of the WGM

resonator, $\kappa_1 = \frac{c}{Q_{ext}}$ is coupling rate between tapered fiber and WGM resonator, Q_{ext} is

external Q, g is the coupling strength between two degenerate WGMs, and Γ is the

additional damping due to the scatterer. The coupling strength and additional damping

rate are following [36],

$$g = -\frac{\alpha f(r)^2 \omega_c}{2V}, \Gamma = \frac{\alpha^2 f(r)^2 \omega_c{}^4}{6\pi v^3 V} \qquad (3.23)$$

, where $f(r)$ is the field distribution at a specific location on the WGM resonator, v is

the speed of light within an environment. At steady state, equation (3.21) and (3.22) can

be converted as below, if we define the normal mode, $a_{\pm} = \frac{(a_{cw} \pm a_{ccw})}{\sqrt{2}}$ with the given

input, $a_{\pm}{}^{in} = \frac{(a_{cw}{}^{in} \pm a_{ccw}{}^{in})}{\sqrt{2}}$,

$$\left[-i(\Delta - 2g) + \frac{2\Gamma+\kappa_0+\kappa_1}{2}\right]a_+ + \sqrt{\kappa_1}a_+^{in} = 0 \qquad (3.24)$$

$$\left[-i\Delta + \frac{\kappa_0+\kappa_1}{2}\right]a_- + \sqrt{\kappa_1}a_-^{in} = 0 \qquad (3.25)$$

32

, where $\Delta = \omega - \omega_c$ is detuning frequency. If we set '+' as symmetric mode and '−' as asymmetric mode, we can see that the symmetric mode is affected. The symmetric mode resonance frequency is shifted by $2g$ and its linewidth is damped by 2Γ, while asymmric mode remains unaffected. Assuming light is coupled from only CW direction, the reflected and transmitted can be depicted as below,

$$r = \frac{\kappa_1(ig+\Gamma/2)}{\beta^2-(ig+\Gamma/2)^2}, \quad t = 1 - \frac{\kappa_1\beta}{\beta^2-(ig+\Gamma/2)^2} \qquad (3.26)$$

, where $\beta = -\Delta + ig + \Gamma/2$.

In actual experimental situation, transmission is captured through the output side of tapered fiber. In the presence of Rayleigh scatterer, transmission contains two Lorentzian functions.

$$T(\omega) = 1 - \frac{A_1 \gamma_1^2/4}{(\omega-\omega_1)^2+\gamma_1^2/4} - \frac{A_2 \gamma_2^2/4}{(\omega-\omega)^2+\gamma_2^2/4} \qquad (3.27)$$

, where ω_1 and ω_2 are resonance frequencies for each mode. By measuring linewidth difference and resonance frequency difference between two modes, Rayleigh scatterer

radius can be obtained. As explained previously, resonance frequency difference correlates with coupling strength, $2g$, between two WGMs and linewidth difference indicate the additional damping, 2Γ, due to Rayleigh scatterer. These two parameters lead to Rayleigh scatterer size measurement. If we take a close look of these two parameters, we realize that field distribution at a specific location and specific mode volume information are not necessary. By taking ratio of these two parameters, $\dfrac{\Gamma}{g} = \dfrac{8\alpha\pi^2 n_e^3}{3\lambda^3}$, field distribution and mode volume variables are disappeared. Only remained parameter is the scatterer polarizability, α. From equation (3.20), radius of the Rayleigh scatterer can be extracted.

$$\alpha = \frac{3\lambda^3 \Gamma}{8\pi^2 n_e^3 g} = 4\pi R^3 \frac{\varepsilon_e}{\varepsilon_0} \frac{\varepsilon_p - \varepsilon_e}{\varepsilon_p + 2\varepsilon_e} \qquad (3.28)$$

$$R = \frac{\lambda}{2\pi n_e} \sqrt[3]{\frac{3\Gamma\varepsilon_0}{4g\varepsilon_e} \frac{\varepsilon_p + 2\varepsilon_e}{\varepsilon_p - \varepsilon_e}} \qquad (3.29)$$

Chapter 4

Mode splitting based Rayleigh scatterer sensing

WGM resonator can sense and count Rayleigh scatterer based on mode splitting sensing scheme introduced in previous chapter. Demonstrations in air are published by Mazzei et al. [36] and Zhu et al. [19]. In this chapter, I demonstrate nanoparticle induced mode splitting in water.

4.1   Multiple nanoparticle sensing with microtoroid

Note that multiple nanoparticle induced mode splitting is demonstrated with a microtoroid [41].

4.1.1 Summary

Scatterer induced modal coupling and the consequent mode splitting in a WGM resonator is demonstrated in aqueous environment. The rate of change in splitting as particles enter the resonator mode volume strongly depends on the concentration of

particle solution. The higher is the concentration, the higher is the rate of change. Polystyrene nanoparticles of radius 50 nm with concentration as low as $5 \times 10^{-6} \, wt\%$ have been detected using the mode splitting spectra. Observation of mode splitting in water paves the way for constructing advanced resonator based sensors for measuring nanoparticles and biomolecules in various environments.

4.1.2 Introduction

In a WGM optical resonator, light circulates along the curved boundary between the resonator material and the surrounding medium by near-ideal total internal reflection. At each revolution the light propagating inside the resonator interacts with the surrounding scatterers or dipoles. The ultrahigh quality factor (Q) and small mode volume (V) of WGM resonators provide enhanced light-matter interaction making the detection of even single binding events possible [22]. Optical WGM resonators thus have emerged as a promising sensing technology and have recently been under intensive investigation [8].

The detection method, based on measuring shift in resonance wavelength of a single WGM, has been largely used to recognize biomolecules and subwavelength particles directly adsorbed on the resonator surface. Arnold et al. [42] demonstrated that the resonance wavelength of a WGM in a microsphere shifts in response to the excess

polarizability induced by a molecule entering the resonator mode volume and discussed the possibility of single-protein detection using this reactive mechanism. Following this work, Armani et al. [43] observed using a microtoroid single molecule sensitivity attributed to a thermo-optic effect. A recent theoretical work by Arnold and co-workers [33] has shown that under the experimental conditions employed the thermo-optic effect results in a smaller shift than the reactive effect, and a new mechanism is necessary to explain the observations. Vollmer et al. [3] demonstrated single virus detection using a microsphere. Meanwhile, WGM resonators of various shapes, such as microring [44], microdisk, microsphere [45], and microcapillary [46, 47], have been used to detect a wide range of large biomolecules, biomarkers, bacteria, and viral particles.

Mode splitting in high-Q WGM resonators has emerged as an alternative to resonance frequency shift method and has been demonstrated to yield label-free and highly sensitive detection of particles with radii as small as 30 nm with single particle resolution [19]. Mode splitting occurs due to the coupling of counter-propagating doubly degenerate WGMs via the scattering of light from a subwavelength scatterer entering the resonator mode volume [25, 39, 40]. This modal coupling lifts the degeneracy and creates two standing wave modes whose resonance frequencies and linewidths differ by

$2g = -\frac{\alpha f(r)^2 \omega}{V}$ and $2\Gamma = \frac{\alpha^2 f(r)^2 \omega^4}{3\pi v^3 V}$, respectively. Here, the polarizability α is defined

as $\alpha = 4\pi R^3 n_e^2 \frac{n_p^2 - n_e^2}{n_p^2 + 2n_e^2}$ for a single particle of radius R and refractive index n_p in the

surrounding medium of refractive index n_e, $f(r)$ is the normalized mode distribution, v

is the speed of light in the medium, and $\omega = \frac{2\pi c}{\lambda}$ is the angular frequency of the

resonant, λ and c being the wavelength of WGM before splitting and the speed of light in vacuum, respectively [19, 36]. Polarizability of a scatterer is calculated as $\alpha = \frac{3\lambda^3 \Gamma}{8\pi^2 n_e^3 g}$ from which one can estimate the size. Advantages of mode splitting method over the resonance frequency shift method are the accurate estimation of the size regardless of the location of the particle in the resonator mode volume and the robustness of the mode splitting spectra against interfering perturbations (e.g., laser and detector noises, temperature fluctuations which uniformly affect the resonator) [48].

Up to date, all the experiments on mode splitting have been performed in air where it is easier to satisfy the mode splitting resolvability criterion $2|g| > \Gamma + \omega/Q$. Demonstration of mode splitting in other media such as aquatic environment would open new possibilities for diverse applications, such as biochemical and biomolecular sensing, detection and characterization of nanoparticles in liquid solutions. In this section, I introduce the demonstration of mode splitting in aquatic environment using a high-Q microtoroidal resonator and investigate the effect of particle concentration on mode splitting spectrum.

4.1.3   Experiment and result

The WGM optical microresonators used in our experiments are silica microtoroids (diameter: 80~100μm) fabricated using a three-step process as follows: (i) photolithography to form circular silica pads over silicon wafer; (ii) selective isotropic

etching of silicon with xenon difluoride gas to form undercut silica microdisks; and (iii) CO_2 laser reflow to turn microdisks into microtoroid [13]. A schematic diagram of our experimental setup is shown in Figure 4.1. Light from a tunable laser λ=670 nm is coupled into and out of the microtoroid using a fiber taper. The gap between the resonator and the fiber taper is controlled by a three dimensional nanopositioning system. A photodetector connected to an oscilloscope is used to monitor the transmission spectra while the wavelength of the laser is scanned. After characterizing the microtoroid in air, I immersed the chip and the fiber taper into a microaquarium filled with water and placed a cover slip on the top. The power before and after the taper section was measured as ~0.6 mW and ~0.4 mW, respectively. The taper-resonator gap is adjusted to minimize thermal effects. The power coupled into the resonator is estimated as ~0.18 mW which is sufficient to exert carousel forces for the binding of particles to the resonator [49]. After the characterization of the resonator in water, solution containing polystyrene (PS) nanoparticles (PS: refractive index n=1.59 and average size R=50 nm) was injected into the microaquarium.
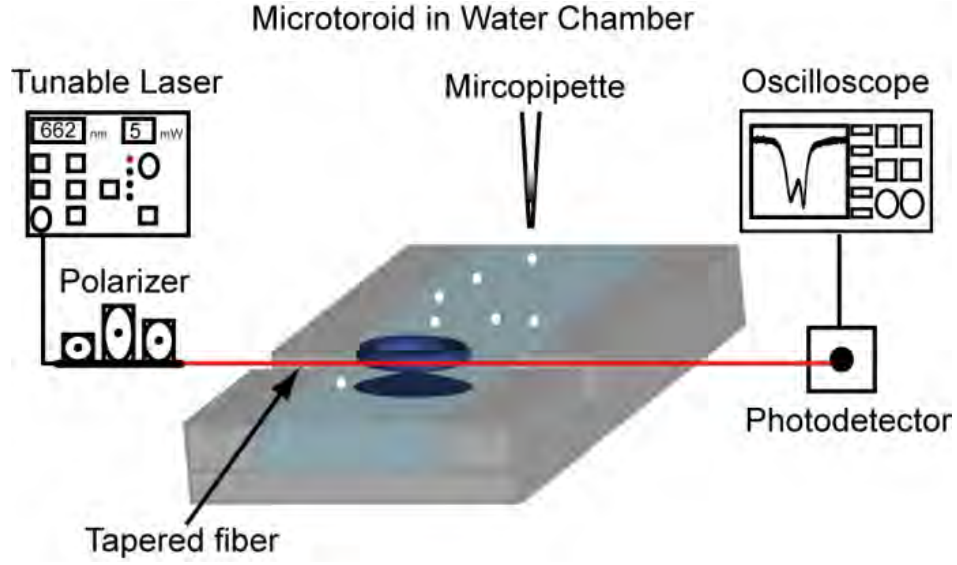
Figure 4.1. Schematics of the experimental setup. Micropipette is used to inject nanoparticles into the microaquarium.

The evanescent tail of the resonant WGM probes the water environment and interacts with the particles once they enter the mode volume or bind onto the toroidal surface. This then leads to modal coupling which shows itself as a doublet (split modes) in the transmission spectra. Figures 4.2 (a) and (b) show typical transmission spectra obtained for a microtoroid in air and in water, respectively, before the nanoparticle solution is injected. The higher loss in water shows itself as a tenfold decrease in the Q of the resonator, i.e., the quality factor reduced from $Q_{air}{\sim}7 \times 10^6$ in air to $Q_{water}{\sim}7 \times 10^5$ in water. Upon the arrival of a PS particle into the mode volume, the single resonant mode observed in the transmission spectra undergoes mode splitting which leads to a doublet. The splitting spectrum shown in Figure 4.2 (c) has $2|g| = 440.9 \, MHz$ and $\Gamma = 1.9 \, MHz$. For a single R=50 nm PS particle, we theoretically estimate $2|g| = 12.3 \, MHz$ assuming that the particle resides on the mode maximum, $f(r) = 0.36$.

This is much smaller than the measured value in Figure 4.2 (c) suggesting multiple particle binding. Based on a multiple scatterer model [50, 51], we estimate that at least N=25 particles are needed to lead to a splitting of $2|g| = 440.9\ MHz$.
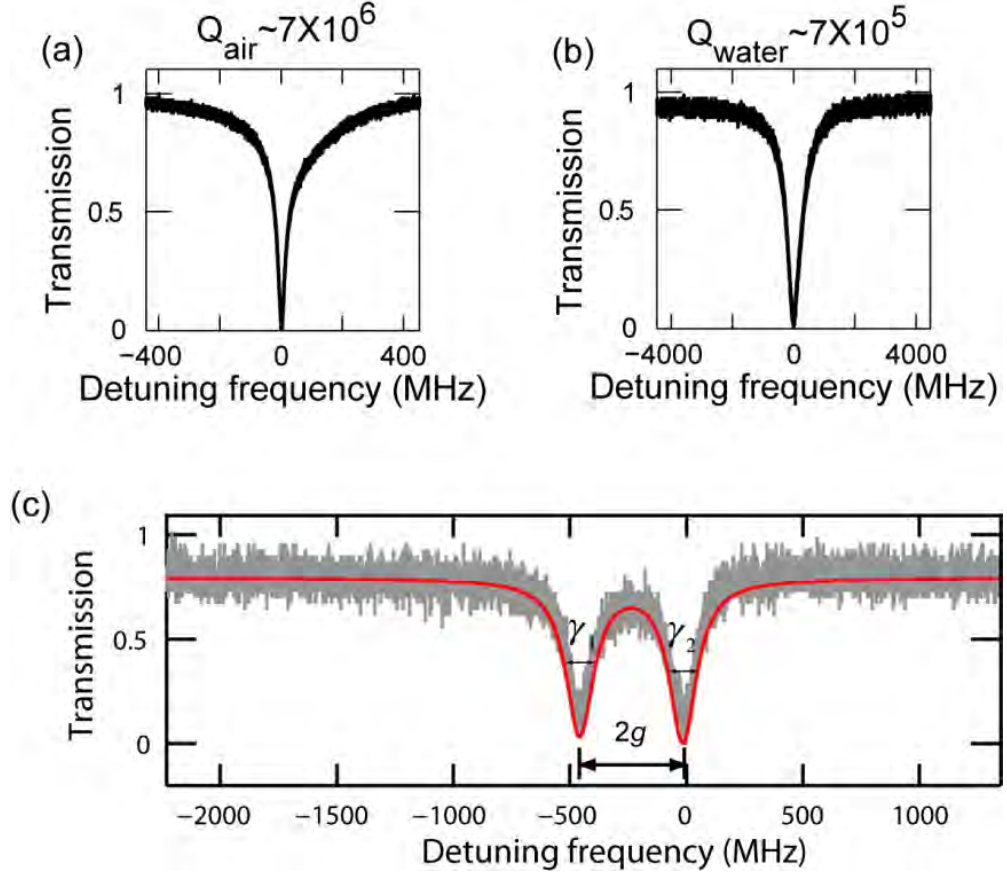
Figure 4.2. Transmission spectra obtained for a microtoroid during the measurements in (a) air and (b) water before nanoparticle injection and (c) in water after nanoparticle injection. The doublet in (c) is the manifestation of mode splitting.

Next, we test the response of the system to various concentrations of PS particles. Figures 4.3 (a) and (b) show a series of transmission spectra obtained for concentrations of $5 \times 10^{-3} wt\ \%$ and $5 \times 10^{-6} wt\ \%$, respectively. Before the injection of the particle

solution, there is no observable mode splitting. After particle injection, it takes a while for the particles to diffuse into the region closer to the resonator. As soon as a particle enters the resonator mode volume, a doublet is formed in the transmission spectra. As more particles bind, the amount of mode splitting $2g$ and the additional linewidth broadening Γ changes. Our theoretical studies and experiments in air on multiparticle binding have shown that at each single particle event $2g$ and Γ undergo discrete jumps to higher or lower values depending on the location of the particle on the mode volume. This allows to resolve single binding events. However, I could not observe such discrete jumps in these experiments. Instead, mode splitting and linewidths increased continuously until there was no observable change in mode splitting or until mode splitting became unresolvable due to increasing dissipation as particle binding continued. Using the multiple scatterer model [50, 51], I estimate that at least N=15 (N=60) and N=4 (N=29) particles are needed to observe the amount of mode splitting shown in the first (last) doublet spectra of Figures 4.3 (a) and (b), respectively.
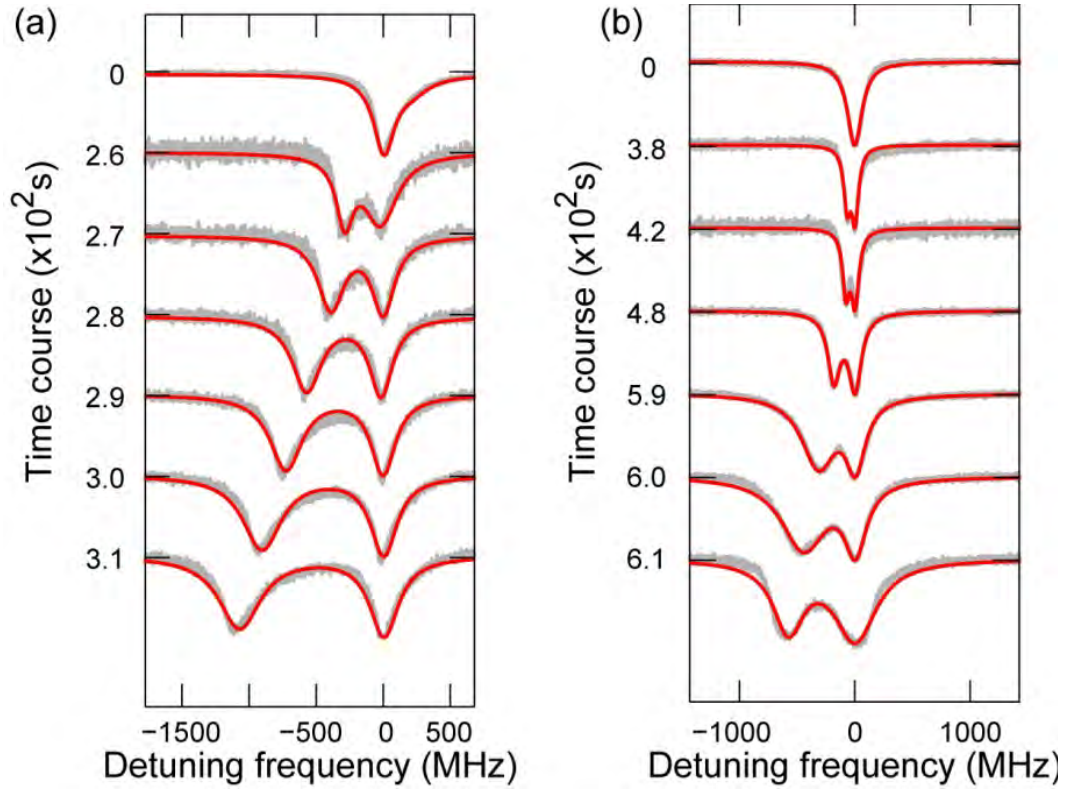
Figure 4.3. A series of transmission spectra obtained for consecutive depositions of nanoparticles (PS, R=50 nm) into the resonator mode volume for particle concentrations of $5 \times 10^{-3} wt$ % (left) and $5 \times 10^{-6} wt$ % (right).

Figure 4.4 depicts the time-evolution of the amount of mode splitting $2g$ for different solution concentrations. Data acquisition was performed until mode splitting becomes unresolved. It is clearly seen that when the concentration is increased, the slope which quantifies the average binding rate increases too. At very high concentration ($10\ wt$ %), due to the larger number of particles in the microaquarium, binding rate is very high which leads to faster coverage of the resonator surface and shorter time for $2g$ to reach its maximum value. During this time $2g$ and Γ continuously increase until a critical value of surface coverage (critical number of particles bind to the surface) is reached.

43

Beyond this point, $2g$ suddenly starts decreasing while Γ keeps on increasing. Thus, the split modes approach to each other with ever increasing linewidths and eventually merge together preventing our system to resolve them.
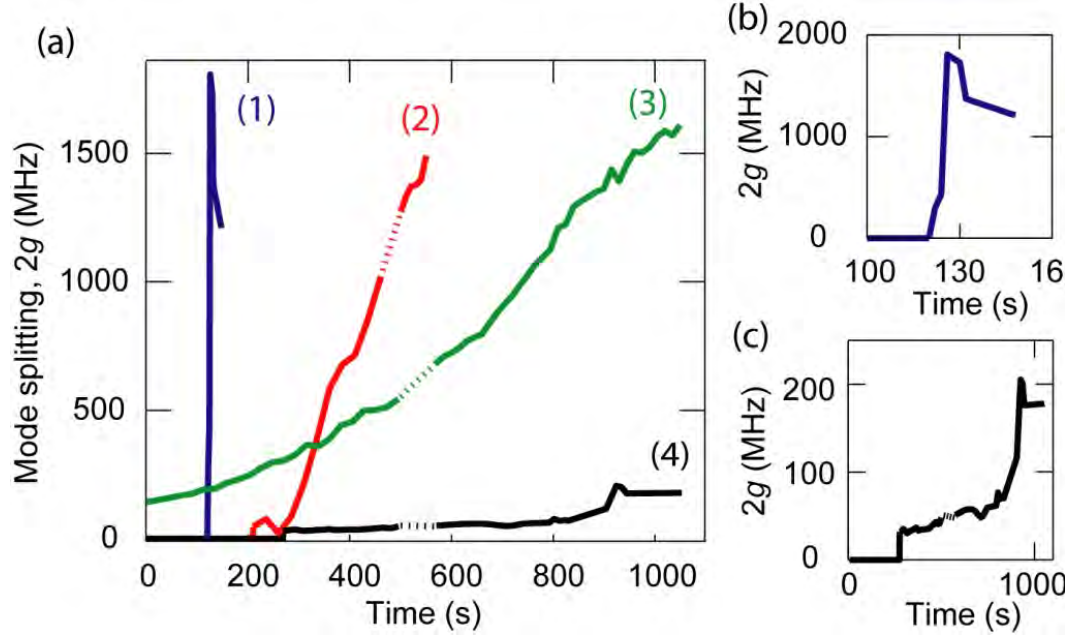
Figure 4.4. Effect of concentration on the amount of mode splitting for PS particles of R=50nm at concentrations (1) $10\ wt$ %, (2) $5 \times 10^{-3}\ wt$ %, (3) $6.5 \times 10^{-4}\ wt$ %, and (4) $5 \times 10^{-6}\ wt$ % in (a). Enlarged plots of the results in (1) and (4) are depicted, respectively, in (b) and (c). Nonzero $2g$ at zero-time (before the injection of PS particles) of (3) is due to intrinsic mode splitting which is caused by scattering centers formed due to surface inhomogeneity and contaminations.

For lower concentrations ($5 \times 10^{-3}wt$ %, $6.5 \times 10^{-4}wt$ %, and $5 \times 10^{-6}wt$ %), on the other hand, binding rate and the number of particles expected to interact with the WGM field are smaller. We observe that at these low concentrations, the critical surface

coverage is not reached during the measurement duration. Therefore, both $2g$ and Γ increase on average; however the rate of increase in Γ with the number of binding particles is so high that the linewidth of low frequency resonant mode undergoes continuous largening which eventually makes it impossible to resolve.

These observations in Figure 4.4 clearly show the concentration dependent binding phenomenon and they coincide with the results of our numerical studies that on average $2g \propto \sqrt{N}$ and $\Gamma \propto \sqrt{N}$. Thus, as the particles continuously enter the mode volume and bind to the resonator, $2g$ increases until a critical number of particles whereas Γ always increases. Chantada et al. discussed [51] that beyond this critical number mode splitting starts decreasing and finally becomes zero.

The probability of simultaneous binding of several particles onto the resonator surface is smaller in lower concentrations, i.e., the probability of one particle binding event is higher. Thus, one would expect to resolve single particle binding events for the resonators used in our experiments. Indeed, footprints of such events, although not as clear as one would expect, are seen in Figure 4.4 for concentrations $6.5 \times 10^{-4} wt$ % and $5 \times 10^{-6} wt$ %. When we look at the evolution of $2g$ much closer, we see that although on average there is a continuous increase, $2g$ shows small up and down jumps which is a consequence of the fact that $2g$ is dependent on the location of the particle on the mode volume, i.e., depending on the location of the incoming particles with respect to the position of the particles already on the resonator surface, $2g$ may

45

decrease or increase. This observation suggests that with much faster data acquisition and much lower concentration, I could accomplish single particle resolution.

4.1.4 Conclusion

In conclusion, I have demonstrated scattering induced mode splitting in ultra-high-Q toroidal microcavities in aqueous environment. These results will open the way for detection of proteins, biomolecules, and nanoparticles in aqueous environment or biomarkers in serum samples using mode splitting phenomenon which provides a highly sensitive self referencing method of detection. I believe that accomplishing these tasks at single particle resolution is within our reach with a faster data acquisition system and a more controlled fluid injection mechanism.

4.2 Observation and characterization of mode splitting in microsphere

4.2.1 Summary

Whispering gallery mode (WGM) optical resonators utilizing resonance shift (RS) and mode splitting (MS) techniques have emerged as highly sensitive platforms for label-free

detection of nanoscale objects. RS method has been demonstrated in various resonators in air and liquid. MS in microsphere resonators has not been achieved in aqueous environment up to date, despite its demonstration in microtoroid resonators. Here, I demonstrate scatterer-induced MS of WGMs in microsphere resonators in water. I determine the size range of particles that induces MS in a microsphere in water as a function of resonator mode volume and quality factor. The results are confirmed by the experimental observations.

4.2.2 Introduction

Whispering gallery mode (WGM) microresonators have been widely studied and used for the label-free detection of nanoparticles, viruses and pathogens [3, 8]. Resonance shift (RS) method, which is based on monitoring the spectral shift in a single resonance mode caused by the change in effective polarizability of the resonator surrounding, has been applied not only for the detection of individual synthetic nanoparticles and virions but also for the detection and characterization of biological phenomena in very small samples. Mode splitting (MS) method, on the other hand, relies on the splitting of a single resonance mode of a WGM resonator into two by scatterer-induced coupling between two frequency counter-propagating degenerate modes [36]. It was recently demonstrated as a highly sensitive alternative to RS method [19]. This self-reference method allows not only the detection at single particle resolution but also the single-shot measurement of particle size. A crucial step in effective use of RS or MS for

47

detecting and studying biomolecules is their demonstration and characterization in various surroundings including air and aqueous environment.

RS method has been the workhorse of sensing applications of WGM resonators, and has been demonstrated in almost all existing WGM resonator geometries including microspheres, microrings, and microtoroids in air, water and buffer solutions [8]. Studies of MS, however, have long been limited to microspheres and microtoroids in air, and only recently was achieved in a microtoroid water [41].

Up to date, demonstration of MS in microspheres and microrings in aquatic environment has not been reported, although Teraoka and Arnold have discussed the conditions under which MS can be observed in spherical resonators [52]. For the MS to become a versatile and effective method for sensing applications, its realization in different WGM resonator geometries and in various environments is very important. Here, I report nanoparticle induced MS in high-Q microsphere resonators in water, and investigate the parameters that affect the observation of MS in such structures.

4.2.3 Experiment and result

I performed experiments using microsphere resonators with different sizes and polystyrene (PS) particles of various radii. Microspheres were fabricated by melting the tip of a tapered silica fiber with CO_2 laser. Light from a tunable laser in 660 nm band is

coupled into and out of the microspheres using tapered fibers. After the characterization in air, the microsphere-taper system was immersed in a deionized water droplet of $\sim$ 50µl. PS nanoparticle samples of 2µl was added to the droplet from a solution of concentration $\sim 2 \times 10^{-11} wt\%$. Transmission spectra were collected continuously for 10~15 min. If MS was not observed, an additional 2µl from the solution was added to increase the particle concentration and hence increase the probability of MS. This was continued until MS was observed.

Transition from air to an aquatic environment shows its first effect on the resonator Q, which degrades due to increased absorption losses in water. This can be partially compensated by working with resonators having resonances in the wavelength band where water absorption is minimal. For example, switching the wavelength from 1.5 μm band to 660 nm leads to more than 1000-fold decrease in absorption coefficient of light in water. Figure 4.5 shows the measured transmission spectra and the corresponding Q factors in both air and water for five microspheres of diameters D=63~200µm. We observe that transition from air to aquatic environment significantly affects the Q of the microspheres with smaller diameter, while the effect on larger microspheres is slight if not unobservable. For example, while the Q of the microsphere with D=63µm experiences a 1000-fold decrease, the change in the Q of the microsphere with D=100µm is less than tenfold, and Q does not change significantly for the microsphere with D=200µm. This can be explained by the increased radiation leakage and bending loss as the size of the microsphere becomes smaller in addition to the absorption in water which affects resonators of all sizes. Note

that the MS seen in Figure 4.5 for the microsphere of D=80μm in air cannot be

resolved when the resonator is immersed in water.
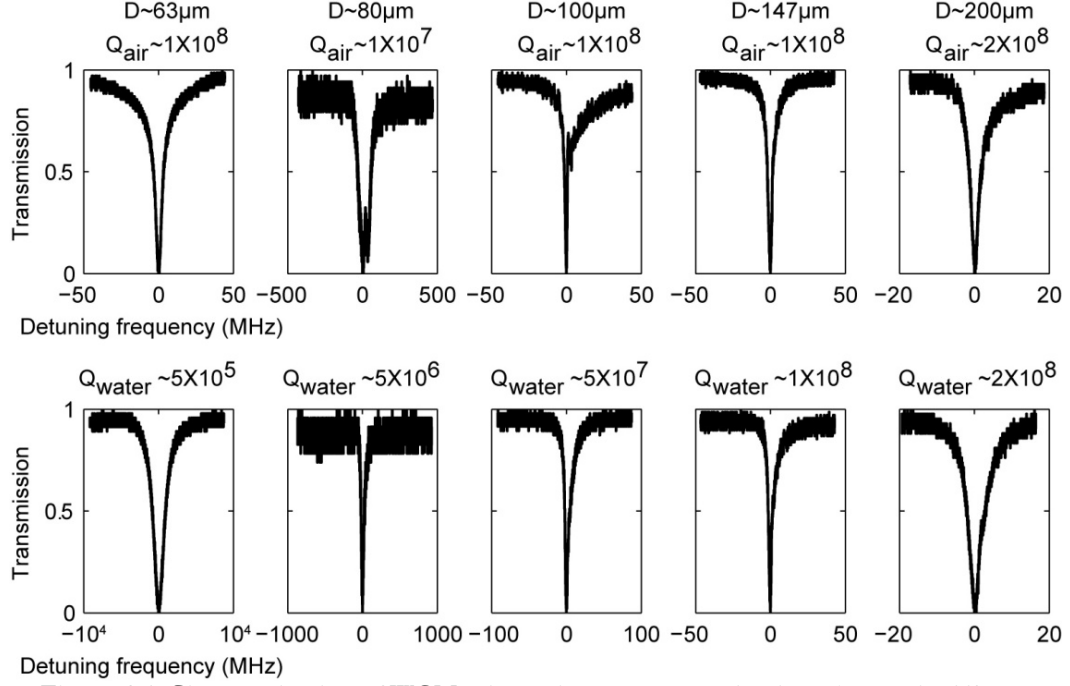
Figure 4.5. Characterization of WGM microsphere resonators in air and water in 660 nm

wavelength band. Q_{air} and Q_{water} are quality factor of the microspheres in air and in water.

Mode volume, which quantifies the confinement of a WGM field in the resonator and

its extension in the surrounding, is another parameter affected by the transition from air

to water. Figure 4.6 reveals the effect of the resonator size, wavelength, and the

surrounding media on the confinement and the distribution of the WGM fields.

Confinement in air $(n_{air} = 1)$ is stronger than in water $(n_{water} = 1.33)$, because

refractive index contrast between the resonator $(n_{silica} = 1.44)$ and air is larger than

that between the resonator and water. It is clear in Figure 4.6 that V_{water} is always larger

than V_{air}; however, the difference is smaller for larger microspheres and for visible light. For example, at λ=660nm, mode volume of a microsphere of D=63 (200)μm increases by 2.6 (0.6)% in water. For the microsphere of D=63μm and λ=1550nm, mode volume in water is 58% larger than that in air, whereas for D=200μm the increase is only 0.1%. Similarly, the value of the normalized field distribution, $f(r)$, at microsphere surface is higher in water and its value decreases with increasing D.
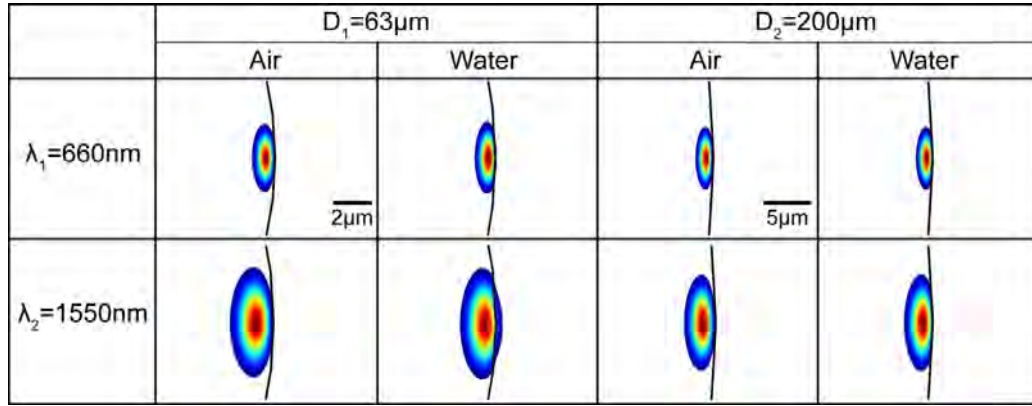
Figure 4.6. Numerical simulation results showing the confinement of fundamental WGM modes in microspheres of different sizes in water and air at two different wavelength bands.

The effect of transition from air to on the MS experiments becomes clearer when we look at the condition to resolve MS which is denoted as $2|g| > \Gamma + \omega/Q$ [53]. Here, $2g = -\frac{\alpha f(r)^2 \omega}{V}$ and $2\Gamma = \frac{\alpha^2 f(r)^2 \omega^4}{3\pi v^3 V}$ are the amount of scatterer-induced MS and additional loss, respectively, ω is the angular resonance frequency of the WGM before the scatterer, Q is the quality factor, v is the speed of light in the surrounding medium, and ω/Q represents the linewidth of the prescatterer resonance mode. The

polarizability α is defined as $\alpha = 4\pi R^3 n_e^2 \frac{n_p^2 - n_e^2}{n_p^2 + 2n_e^2}$ for a spherical particle of

radius R and refractive index n_p in a surrounding environment of n_e. It is clear that a

spherical particle of radius R has a larger polarizability in air than in water because the

refractive index contrast between the surrounding and the particle is larger in air,

i.e., $\frac{n_p^2 - n_{air}^2}{n_p^2 + 2n_{air}^2} > \frac{n_p^2 - n_{water}^2}{n_p^2 + 2n_{water}^2}$. Thus, if all other parameters are kept constant, the smallest

detectable particle size using MS method is larger in water than in air.

Experimental results presented in Figure 4.7 show the dependence of $2g$ on the size of

the microsphere and the nanoparticle. For a fixed particle size, the splitting $2g$

decreases as the size of the microsphere is increased. Moreover, for a fixed size of

microsphere, there exists a particle size which leads to the largest $2g$, i.e., particles with

much smaller or larger size leads to decrease in $2g$. Numerical simulations show a

similar tendency.
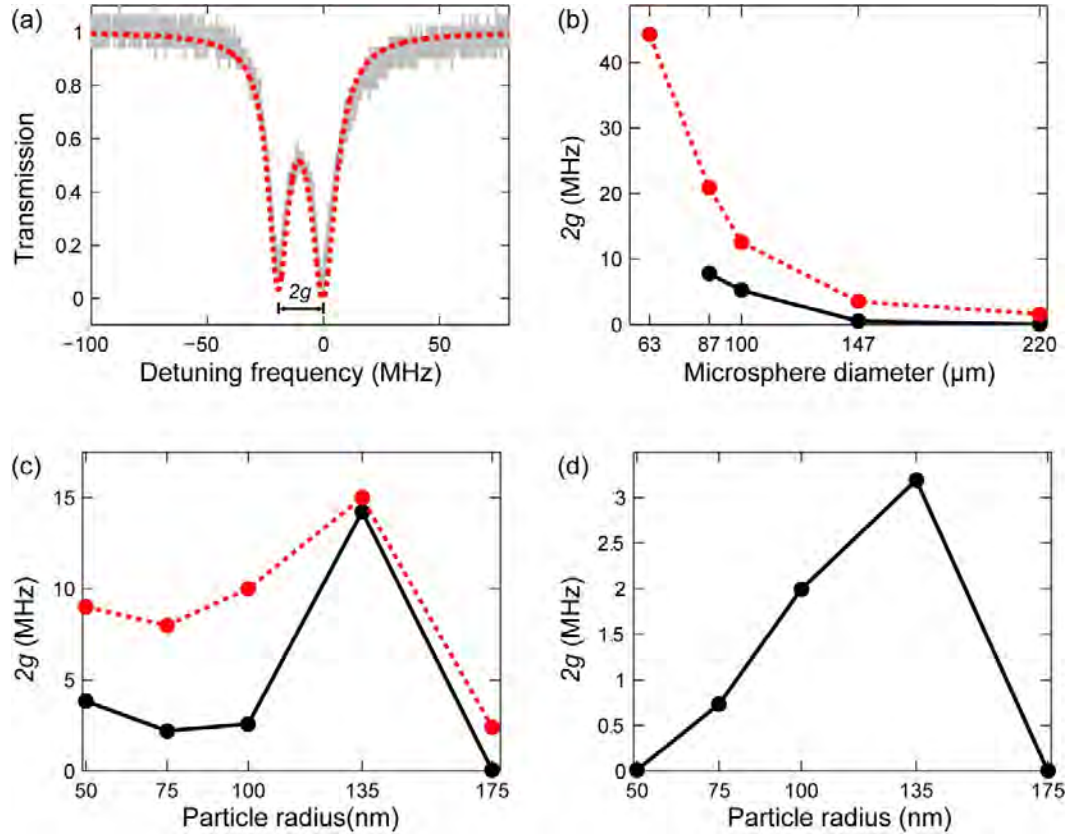
Figure 4.7. Nanoparticle-induced MS in a microsphere resonator placed in water. (a) A typical MS spectrum observed in a microsphere of diameter D=87μm for PS nanoparticle of R=50 nm. The amount of MS is $2g = 19.4\text{MHz}$. Dashed curve is the Lorentzian fit to the experimental data. (b) $2g$ vs the size of microsphere resonator for nanoparticles of R=50 nm. (c) $2g$ vs the nanoparticle size for microspheres of size D~89μm (d) $2g$ vs the nanoparticle size for microspheres of size D~214 μm. In (b) and (c), dashed curves are simulation results.

For a given Q there is a threshold R beyond which the MS process is dominated by scatterer-induced losses, that is $\Gamma \gg \omega/Q$. Then, $2|g| > \Gamma$ should be satisfied to ensure resolvability of MS, which, in turn, requires $\alpha < 6\pi(v/\omega)^3$. There is an upper limit for R beyond which Γ reaches so large values (i.e., $\Gamma > 2|g|$) that MS can no

longer be resolved. On the other hand, for very small R, cavity-related losses starts dominating, that is $\Gamma \ll \omega/Q$. Then the condition to resolve MS becomes $2|g| > \omega/Q$ which requires that $\alpha > VQ^{-1}f(r)^{-2}$. Thus, in order to detect smaller particles, one needs to assure higher Q/V and higher $f(r)^2$ at the particle location. Then for a given Q/V, there is a critical value of α, hence R, below which MS cannot be resolved.

It is obvious that observing MS in water is more difficult than that in air, because a particle of size R has smaller polarizability, and a microsphere of size D has larger V but smaller Q in water. One cannot make V arbitrarily small because this will further reduce Q. Detecting a nanoparticle with polarizability α using a microsphere resonator in water requires careful fabrication of the resonator such that the delicate balance between α, Q, V, and $f(r)^2$ quantified by $\alpha > VQ^{-1}f(r)^{-2}$ is satisfied.

The MS resolvability relation, $2|g| > \Gamma + \omega/Q$, corresponds to a second order inequality in α whose solution is depicted in Figure 4.8. The contours in Figure 4.8 denote the size ranges of the nanoparticles and microsphere resonators which satisfy the MS resolvability condition for a given Q of the resonator. Figure 4.8 confirms the results of Figure 4.7 and above discussions showing that the range of particle polarizability (i.e., size if the refractive index is known or vice versa) for observable MS depends on the size and quality factor of the microsphere resonator. In Figure 4.8, I also include the results of nanoparticle detection experiments reported in the literature for microsphere resonators using the RS technique. It is clearly seen that the reported Q

and D of the microspheres do not allow a resolvable MS for the nanoparticles tested in those works. For example, Shopova et al. [54] has reported that although detection of single PS nanoparticles of radii R=40 nm has been achieved using RS technique using a microsphere of D=70μm and $Q \sim 10^6$, MS could not be observed. Our resolvability criterion suggests that with the reported Q and D, one cannot observe MS with particles of R=40 nm because such particles will fall outside the detectable particle size range of 120nm<R<195nm. Thus, it is not surprising that the authors could not see MS in their experiments. Similarly, in my experiments with a microsphere of D=200μm and $Q \sim 10^8$, I could not detect PS particles of R=50nm which falls out of the size range 57nm<R<207nm predicted by the MS resolvability condition for the used microsphere. The same PS particle could be detected with a smaller microsphere of D~90μm and $Q \sim 5 \times 10^7$ as it falls in the range of detectable particle size of 37nm<R<208nm. These results showing the delicate relation among microsphere size, particle size, and the Q-factor of the resonator agree well with the predictions of Teraoka and Arnold [52].
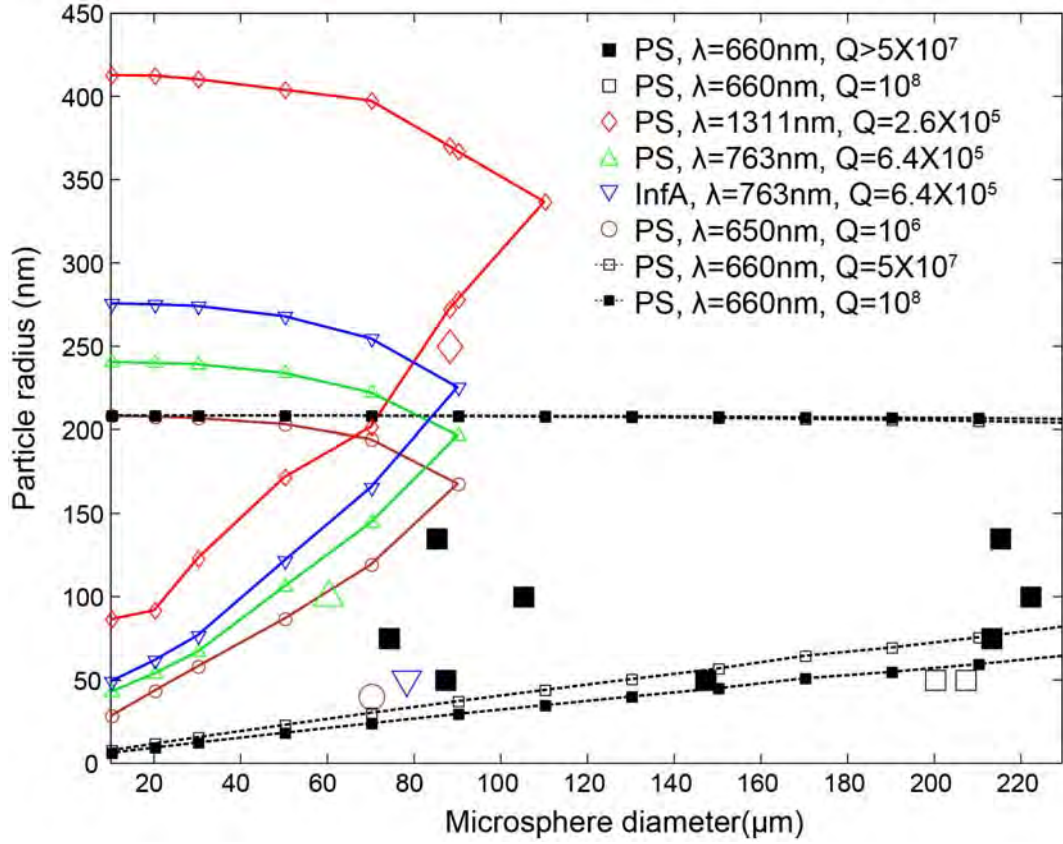
Figure 4.8. Constant Q contours bounding the size range of nanoparticles which can induce MS in microspheres resonators of different diameters in water. The boundaries are calculated from the MS resolvability criterion using Q, λ, and D from our experiments (dashed contours and square markers) and those from Vollmer et al.'s and Shopova et al.'s (solid contours. MS could not be observed for the data points lying outside the contours denoted by the same marker. The only data which induced MS are the ones represented by filled squares.

Figure 4.9 clearly shows that V_{sphere} is always larger than V_{toroid} for D>10μm. This agrees well with the results of Arnold et al. [33] Larger V makes it more difficult to observe MS in microspheres. To induce MS for a given particle size, a microsphere

having the same diameter as a microtoroid requires higher Q. A microtoroid having the same Q and the same major diameter as a microsphere can detect smaller particles.
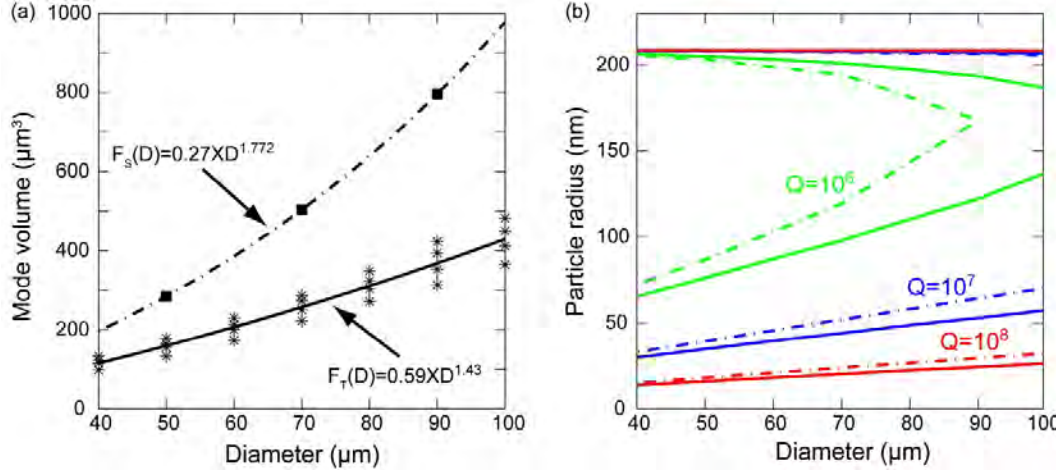
Figure 4.9. Numerical simulation results showing the comparison of (a) mode volume and (b) MS resolvability criterion for microsphere (dashed) and microtoroid with minor diameter d=5μm (solid) resonators in water as a function of their major diameter at λ=660nm band. The *'s in (a) indicate d=3~6μm. In (b) constant Q contours bound the size range of particles which can induce MS.

4.2.4 Conclusion

In conclusion, I observed MS in a microsphere in aquatic environment, and systematically analyze the relation between the size and quality factor of the resonator and the detectable range of particle size using the MS technique. I also discuss why nanoparticle induced MS could not be observed in earlier experiments in aqueous

medium, and provide a relation to optimize the microsphere size and quality factor for the targeted range of particle sizes.

Chapter 5

Single nanoparticle and individual pseudo-biological sample sensing

In this chapter, I present single nanoparticle and individual synthetic hemozoin crystal sensing and sizing. Main purpose of this demonstration is to show that mode splitting sensing scheme can be used for biosensing application for individual nano-scale object sensing. It is published in [55].

5.1   Summary

I report the detection and the size measurement of single nanoparticles (i.e. polystyrene) in aquatic environment using mode splitting in a whispering gallery mode (WGM) optical resonator, namely a microtoroid resonator. Using this method I achieved detecting and measuring individual synthetic hemozoin nanocrystals—a hemoglobin degradation by-product of malarial parasites—dispersed in a solution or in air. The results of size measurement in solution and in air agree with each other and with those obtained using scanning electron microscope and dynamic light scattering. Moreover, I compare the sensing capabilities of the degenerate (single resonance) and non-degenerate (split mode, doublet) operation regimes of the WGM resonator.

5.2   Introduction

Rapid detection and measurement of biological and synthetic nanoparticles, bioanalytes, and nanoscale biological material in ultra-small sample size and with single nano-object resolution are of significant importance for diagnostic and prognostic applications, environmental monitoring, food safety, and homeland security. In recent years, different sensor platforms exhibiting enhanced detection capabilities, based on monitoring the shift in the frequency of optical, mechanical and plasmonic resonances, have been developed [34, 56, 57]. Here, I report the use of resonance mode splitting in a whispering-gallery-mode (WGM) microtoroidal optical resonator placed in aquatic environment as a platform for label-free detection and measurement of individual nanoscale objects. In particular, I present detection and size measurement of polystyrene (PS) nanoparticles and synthetic hemozoin nanocrystals with single particle/crystal resolution.

Hemozoin is a crystalline metabolite of *Plasmodium* parasites, a causing agent of malaria disease. Despite global eradication strategies all over the world, malaria still kills almost 1 million people each year, urging rapid sensitive diagnosis techniques and effective treatment regimens. It has been recently postulated that detection of hemozoin crystals can be readily exploited for rapid diagnosis of malaria parasites, because hemozoin is continuously produced and released from red blood cells and captured by immune cells of the host during blood circulation of *Plasmodium* parasites [58-60]. Hemozoin is formed inside the acidic digestive vacuoles of intraerythrocytic parasites. The parasites

utilize host-hemoglobin and release free-heme (Fe^{2+}-protoporphyrin IX) which is subsequently converted into insoluble crystals called hemozoin (Fe^{3+}-protoporphyrin IX) as a result of the detoxification process. Recent reports have revealed that optical detection techniques such as third harmonic generation imaging (THG) and tip-enhanced Raman scattering (TERS) can detect hemozoin crystals inside the infected blood cells [61, 62]. However, it is obvious that the level of the signal obtained in these techniques is very much dependent on the number of parasites and hence on the amount of hemozoin, i.e., the larger the amount of hemozoin is, the higher the detected signal intensity is. Moreover, the level of hemozoin circulating in immature forms is very low, making it difficult to detect. Thus, there is a clear need to improve the detection limits of hemozoin crystals to the single nanocrystal/molecule resolution to detect even trace amounts of hemozoin circulating in the blood or serum.

The interests in WGM microresonators have been continuously increasing since the first reports on the detection of streptavidin-to-biotin binding [57] and DNA hybridization [63] by monitoring the resonant frequency shifts in microsphere resonators. These initial works were followed by the demonstrations of single virion and single particle detection using microspheres [3]. The underlying physics of these works rely on the shift of the resonance frequency due to a change in the effective polarizability of the resonator-surrounding compound system upon the entering of a particle, molecule or virion into the resonator mode volume [3, 8]. In spectral shift method (i.e., also known as reactive shift method), individual events are detected accurately; however, size measurement of detected individual particles is hindered by the

dependence of the amount of resonance shift on the position of the particle in the mode volume of the resonator. Thus, statistical techniques are employed, e.g., maximum frequency shift observed in an ensemble measurement is used to estimate the size of particles in the ensemble [49]. Statistically significant number of measurements should be performed to have high confidence in assigning an observed shift to be the maximum shift. Moreover, size estimation from resonance shift requires the knowledge of resonator mode volume.

Recently, mode splitting technique has been proposed and used as a highly sensitive and robust platform to detect individual nanoscale materials and take single shot size measurement one-by-one on each detected material. In contrast to the reactive shift method, in mode splitting method, in which a single resonance mode splits into two when a nanoscale object, such as a nanoparticle or a virus, enters into the mode volume, size of each detected object can be estimated in a single-shot measurement; neither the position of the object in the mode volume nor the prior information of the WGM volume is required for the measurement [19]. The early works performed in dry environment were followed by the demonstration of mode splitting in microtoroid [41] and microsphere [55] resonators in aquatic environment. However, whether the splitting was induced by a single particle or not could not be confirmed. Recently, Lu et al. have shown single particle induced mode splitting in a microtoroid placed in water [35]. In order to minimize the noises introduced into the transmission spectra by spectral fluctuations of the tunable laser, whose wavelength is scanned to monitor the resonance shifts and mode splitting, the authors used a thermally stabilized reference

interferometer. He et al., on the other hand, reported single particle induced mode splitting in water using an active microresonator driven above lasing threshold [64]. However, none of these works provided the polarizability and hence the size measurement of each detected nanoparticle in aquatic environments.

Here, for the first time, I report the detection and size measurement of individual nanoparticles (PS and synthetic hemozoin) in aquatic environment using mode splitting in a passive (no active gain medium) microtoroid resonator without the need for stabilization or noise cancellation interferometers. Moreover, I quantify the differences between the spectral shift and mode splitting methods and the regimes of quality (Q) factor and particle size where one or both of these methods can be effectively used.

5.3 Materials and methods

5.3.1 Materials

Polystyrene nanoparticles were purchased from Thermo Scientific with mean radius of R=75nm with standard deviation of σ=2.2nm. The coefficient of variation (CVs) defined as the ratio of the standard deviation to mean value, for these particles is 2.9%. Ultrapure DI water was obtained from Sigma-Aldrich. Silica wafers used for the fabrication of the microtoroids were purchased from WRS Materials.

5.3.2 Methods

5.3.2.1 Microtoroid and taper fiber fabrication process

Microtoroids were fabricated from silica-on-silicon wafer through a three step process as described previously [13]; (i) Standard photolithography for patterning circular silica disks on silicon wafer, (ii) Xenon difluoride (XeF_2) for selective isotropic etching of silicon to form undercut structure with silica disk over silicon pillar, and (iii) CO_2 reflow to transform the disk to a torus forming silica microtoroid on silicon pillar. A microtoroid is defined by its major and minor diameters. For my experiments, I fabricated microtoroids of minor diameters d=7~10μm and major diameters D=50~80μm.

5.3.2.2 Taper fiber fabrication process

Taper fiber for coupling light into and out of the microtoroid resonator was fabricated by heating-and-pulling a single mode silica fiber under hydrogen flame. The jackets of single mode silica optical fibers were removed and the exposed clad was cleaned with isopropyl alcohol. The fiber was then placed on a home-made holder with fiber clips at two ends, and positioned above hydrogen flame. Pulling speed and distance were controlled by two servo motor controllers. Tapering process was continuously

monitored under microscope. Optical fiber taper with diameters approximately 1μm was fabricated.

5.3.2.3 Preparation of synthetic hemozoin

Synthetic hemozoin, chemically shown to be identical to natural hemozoin [65], was purified from hemin chloride using an acid-catalyzed method which produces smaller and ~200nm in size homogenous crystals as described earlier [60, 66] Briefly, 45mg hemin chloride was dissolved in 4.5ml 1N NaOH and neutralized with 1N HCl. With the addition of acetic acid (until the pH reached 4.8, at a constant temperature of 60ºC with magnetic stirring), the mixture then was allowed to precipitate at room temperature overnight. The precipitate was subjected to a wash with 2% SDS-buffered with 0.1M sodium bicarbonate (pH 9.1) and subsequent extensive washes with 2% SDS, and then six to eight washes with distilled water. A stock solution in distilled water was prepared and stored at 4ºC. The hemozoin was dried, weighed and the concentration was calculated in either mM or mg/ml. FTIR and powder X-ray diffraction pattern of the synthetic hemozoin confirmed the chemical composition and structure as previously described [66]. Figure 5.1 shows the different stages after the infection of an erythrocyte with a rodent parasite *P. yoelii* and the FESEM images of synthetic hemozoin visualized using ultra-high-resolution FESEM.
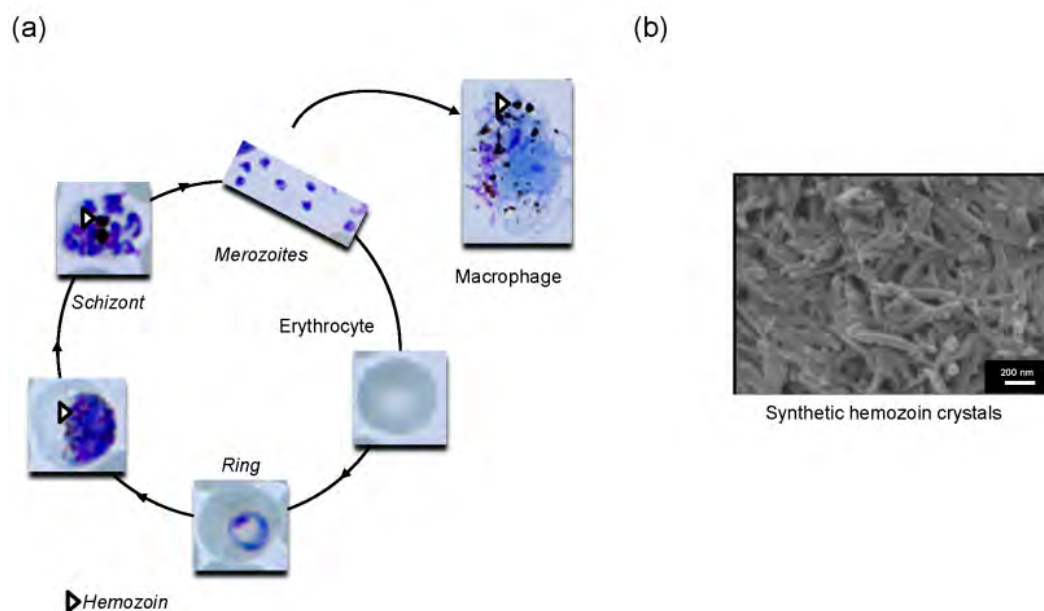
Figure 5.1. (a) Hemozoin is continuously produced by *Plasmodium* parasites inside the erythrocytes. *Plasmodium* parasites have a repetitive life cycle within the erythrocytes of the mammalian host (erythrocytic blood-stage). Hemozoin is produced primarily within trophozoite-stage parasites and is almost continuously released into the blood stream during malaria infection. Released hemozoin is readily captured by immune system cells such as macrophages. Figure shows the life cycle of rodent parasite *P. yoelii*. (b) SEM pictures of synthetic hemozoin purified from hemin chloride.

5.3.2.4 Delivery of the particles and hemozoin crystals to the resonator mode volume

For experiments performed in water, the solution containing the hemozoin crystals or the nanoparticles was continuously pumped into and out of the aquatic chamber (see Figure 5.2) used in the experiments at a rate of 1ml/min. I chose a flow path such that

the particles pass proximity of the resonator, entering its mode volume or occasionally adsorbed to the resonator surface.

For hemozoin and PS particle experiments performed in air, I used the setup reported in our previous work [19], which consists of an atomizer and a differential mobility analyzer (DMA) connected to a micro-nozzle (diameter: 20μm). The DMA is one of the most commonly used equipments that classifies and measures the size of nanoparticles, based on their electrical mobility [19, 67]. The atomizer is used to disperse the nanoparticles or the hemozoin crystals from the particle suspension. Droplets produced by the atomizer are passed through a Po^{210} radioactive neutralizer which removes the electrical charges on the particles and then sent to a diffusion dryer with silicone-gel as the desiccant for removing the solvent in the droplets. The particle stream is then sent through a Kr^{85} radioactive particle charger to place a well-defined charge distribution on the particles as a function of their size. Afterwards, the particles flow to the DMA which consists of a flow channel between an assembly of two concentric cylindrical electrodes, separated with air gap. An electric field is applied between the electrodes. The particle flow, introduced near one of those electrodes, is joined by a larger sheath flow. As the particles are carried along the channel by this combined flow, the particles of appropriate charge polarity migrates across the channel under the voltage difference between the electrodes. The rate of the migration depends on the electrical mobility of the particles, which in turn, depends on the size and electrical charge of the particle. If all the particles in the flow have the same charge, then particles having a specific mobility will be all of the same size. Moreover, the smaller the particle and/or the

higher the electrical charge is, the higher the electrical mobility is. A small slit then

allows the particles having a specific electrical mobility within a narrow range to exit.

Thus, particles whose electrical mobility matches the position of the outlet slit at a

certain applied voltage pass the DMA. For a given DMA configuration, the electrical

mobility in the DMA to outlet the particles at a certain location is given as

$$Z_p = \frac{q_e + q_m}{4\pi \Lambda V} \qquad (5.1)$$

where q_e and q_m are the flow of sheath air at the DMA entry and the exit, respectively,

and Λ is a constant depending on the DMA configuration given as

$$\Lambda = \frac{L}{ln(r_2/r_1)} \qquad (5.2)$$

with L, r_1, and r_2 denoting the length of the DMA, and the radii of the inner and outer

electrodes from the DMA capacitor, respectively. On the other hand, the electrical

mobility, Z_p, of a singly charged particle with diameter d is given as

$$Z_p = \frac{eC_d}{3\pi \eta d} \qquad (5.3)$$

where e is the charge of an electron, η is the viscosity of the gas and C_d is the

Cunningham slip correction which approaches to one for a particle larger than the mean

free path of the gas and increases with decreasing particle size. For particles exiting the

DMA, Eqs. 5.1 and 5.3 are equal. Thus by changing the applied voltage, V, particles within a certain diameter range can be made to exit the DMA.

In my experiments, the particles exiting the DMA are then deposited through the micro-nozzle onto the microtoroid resonator which was placed a few hundreds of microns away from the nozzle. The flow rate was set to be $0.02cm^3/s$ so that there is no more than one particle deposition event within the detection window of 0.1s. Moreover the concentration of the hemozoin crystals or the nanoparticles in the solution was adjusted to be ~100fM to further suppress simultaneous deposition of multiple particles. With these settings, I observed on average one particle or crystal binding event in every 5s.

For accurate size measurements, it is important that no aggregation takes place, because aggregations will lead to larger size readings. In order to prevent or minimize aggregations, I used water bath sonication for 5 minutes prior to each experiment performed in water and in air. Moreover, since I have worked with samples of very low concentration (~100fM), the likelihood of collisions and interactions which may lead to aggregation is low (i.e., the higher concentration of the particles or crystals in the suspension, the higher the probability of aggregation). Indeed, I also performed dynamic light scattering (DLS) and SEM measurements and could not see strong indication of aggregation (i.e., DLS size measurement distribution indicates the degree of aggregation).

5.3.2.5 Experimental set-up

The experimental setup used during the measurements in aquatic environment is similar to our previous work [41] as shown in Figure 5.2. The chip containing the microtoroid resonators is immersed in an aquarium which is placed on 3D translational stage to finely tune the distance between the resonator and the taper fiber. Light from a 670nm tunable diode laser was delivered to the resonator through a fiber taper. The output wavelength of the laser is continuously scanned at a rate of 5Hz. Among the four tunable lasers (660nm, 980nm, 1460nm and 1550nm wavelengths) I chose the visible wavelength laser (λ=670nm) because light absorption in water is weaker in the visible band than the near-infrared band. A silicon PIN photodetector with 125MHz bandwidth connected to an oscilloscope was placed at the output end of the optical fiber to monitor the transmission spectra. When the laser wavelength satisfies the resonant condition, the light is coupled into the WGM of the microtoroid resonator causing a resonance dip in the transmission. The wavelength at which the dip occurs corresponds to the resonance wavelength. The measurement system was controlled by a computer using Labview. When a nano-scale object enters the field of the resonator, the resonance splits into two forming a doublet in the transmission spectra. A two-Lorentzian curve fitting is applied as soon as the transmission is acquired to the computer to obtain the resonance frequencies and linewidths of the doublets. After obtaining these parameters, the polarizability and then the size of each detected nano-object are estimated.
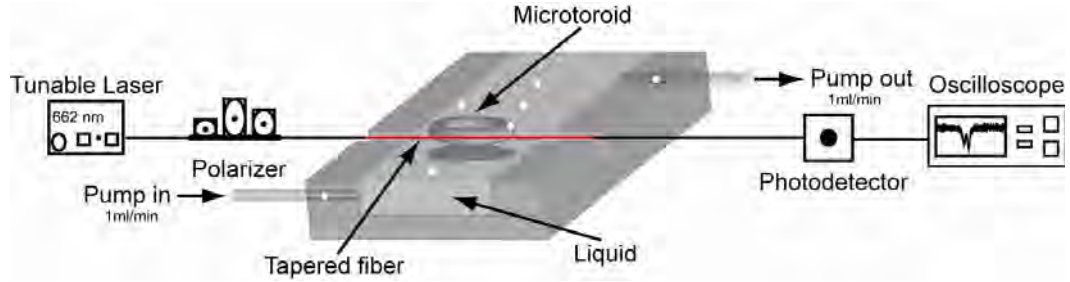
Figure 5.2. Schematics of the setup used in mode-splitting based single particle detection and measurement experiments in aquatic environment. A high-Q whispering gallery mode microtoroid resonator is placed in an aquatic chamber (dimension: 3.2cm×1cm×0.5cm). The solution including hemozoin crystals or nanoparticles is pumped into and out of the chamber at a rate of 1ml/min using a micropump.

5.3.2.6 Evaluating the performance of mode splitting method

The performance of mode splitting method in estimating the size of each detected particle is evaluated by comparing the estimated sizes with the size distribution obtained from dynamic light scattering (DLS, Malvern Zetasizer Nano) system and from scanning electron microscope (SEM, Nova 2300, FEI) images, as well as with the data provided by the manufacturers of the nanoparticles. Moreover, for the measurements performed in air, I used a DMA which selects the deposited particles based on their electrical mobility with approximately 5% size deviation. In the following, I present the basics of size measurement by DMA, DLS, and SEM.

Differential Mobility Analyzer (DMA) selects particles of certain electrical mobility. It can be also used to make size measurements. From Eqs. 5.1 and 5.3, we have

$$d = \frac{eC_d}{3\eta} \frac{4\Lambda V}{q_e + q_m} \qquad (5.4)$$

for a given DMA configuration and applied voltage. Since C_d depends on the size of the particles, this relation should be iteratively solved to estimate the size. The DMA used in our experiments selectively delivers nanoparticles within approximately 5% size deviation based upon the electric mobility of the nanoparticle [68]. We should emphasize here once more that the size selected and/or estimated in a DMA is the electrical mobility size.

Dynamic Light Scattering (DLS) is a well-established technique for measuring the size and size distribution of small, typically sub-micron, particles (e.g., dielectric or metallic nanoparticles, molecules, proteins, polymers, etc.) dispersed in a liquid environment [69]. Particles in a dispersion are in a constant, random motion known as Brownian motion (i.e., the larger the particle, the slower the Brownian motion). When such dispersion is illuminated by a coherent light source (i.e., a laser), time-varying intensity fluctuations, 'dynamic speckles', in which the position of each speckle is seen to be in motion, are observed due to the destructive or constructive interference between the light scattered from moving particles whose distances from each other are constantly varying. The rate

at which these fluctuations take place yields the velocity of the Brownian motion and hence the particle size. Thus, in principle, DLS measures the Brownian motion, which is then related to the size through the Stokes-Einstein relationship. In a typical DLS measurement, the rate of changes in the scattered light intensity can be obtained by comparing the intensity $I(t)$ at time t to the intensity $I(t + \tau)$ at a later time $t + \tau$. Making this comparison over a long measurement time T yields the intensity correlation function $G_2(\tau)$

$$G_2(\tau) = \frac{1}{T}\int_0^T I(t)I(t + \tau)d\tau \qquad (5.5)$$

which describes the dynamics of the particle motion but does not yield information on their correlated motions. This information can be obtained from the electric field correlation function $G_1(\tau)$

$$G_1(\tau) = \frac{1}{T}\int_0^T E(t)E(t + \tau)d\tau \qquad (5.6)$$

which is related to the measured $G_2(\tau)$ through Siegert relationship

$$G_2(\tau) = B[1 + \beta|G_1(\tau)|^2] \qquad (5.7)$$

and has an exponential form with decay rate

$$G_1(\tau) = e^{-\Gamma\tau} \qquad (5.8)$$

for a system undergoing Brownian motion. In Eq. 5.7, B and β are baseline and instrumental response which are determined experimentally. The decay constant Γ is related to diffusivity (D)

$$\Gamma = Dq^2 \qquad (5.9)$$

where

$$q = \frac{4\pi n}{\lambda} sin\frac{\theta}{2} \qquad (5.10)$$

reflects the distance the particle travels. Thus, D can be determined from experimentally measured Γ if the angle θ and the refractive index n are known. Finally, the particle size for spherical particles is extracted from the Stokes-Einstein relation, which relates D to thermodynamics and hydrodynamics as

$$D = \frac{kT}{6\pi\eta r} \qquad (5.11)$$

where k is the Boltzman's constant, T is the temperature, η is the viscosity and r is the radius of the particle. Thus, size is determined from D if T and η are known. If the system is monodisperse, then the mean effective diameter of the particles is determined.

It should be noted here that size estimated in DLS is based on the translational diffusion of the particle within the dispersion, thus it is referred to as the hydrodynamic size (i.e., the size of a sphere having the same diffusion coefficient as the particle being measured).

For SEM measurements, a number of particles are deposited onto a microtoroid resonator using the DMA and then the resonator was taken to SEM. Particle size (geometric size) was estimated by processing the acquired particle images with a built-in toolkit of the SEM. This is done by calculating the circle equivalent diameter by measuring the area of the image of the particle and then back-calculating the diameter of a circle with the same area. This method depends on the edge-contrast settings and on which view is captured. Thus, obtained results may not be directly comparable with other size measurement methods, especially when the particles are non-spherical.

It is clear that each of the above methods gives the size of a particle just by one quantity (e.g., a number and a unit) regardless of its shape. If all the particles measured have the same shape, this is unambiguous. However, when the particles have different and/or irregular shapes, one single quantity to describe the size may cause ambiguity. However, usually the shapes of the particles to be measured are not given or are not known exactly. Thus, in particle size measurement and aerosol technology, an equivalent diameter or radius has been introduced and used to give the particle size by one quantity regardless of their different shapes [70]. Using equivalent diameters, various irregularly shaped particles can be evaluated on the basis of a single consistent measurement. An

equivalent spherical diameter (or radius) is the diameter (or radius) of a sphere which has a certain size-dependent property with the particle being measured. This size-dependent property depends on the measurement technique used for the determination of the particle size. Different techniques measure different properties of the particle, and thus produce different size distributions for identical samples. In DLS the estimated hydrodynamic size for non-spherical particles is the size of spherical particles which has the same translational diffusion as the particle being measured. Thus, changes in the particle shape, such as the length of a rod-like particle, affect the diffusion speed of the particle. On the other hand, different shape changes, such as the diameter of a rod-like particle, which hardly affects the diffusion speed, may not be detected and hence the size estimation will not change. In DMA, the estimated size is the equivalent electrical mobility diameter that is the size of spherical particles which has the same electrical mobility as the particle under test. In SEM or TEM, the estimated size can be the equivalent circle diameter, which is the diameter of a sphere whose projected area is the same as the projected particle image.

Thus, in many applications, where the exact shape of the particles are not known, the estimated size is the size of a sphere which has the same measured property (e.g., translational speed, polarizability, view or image) as the particle under test. Thus, in this work I follow the same methodology and assign the measured size as the size of a spherical particle having the same measured polarizability as the particle being measured using mode splitting in a WGM microtoroid resonator. In short, here I measure the equivalent polarizability diameter.

5.4   Results and discussions

5.4.1 Basis for WGM optical resonance sensors

A WGM resonator supports the propagation of light via total internal reflection if the optical path length is an integer multiple of the wavelength of the WGM light, that is $2\pi n_{eff} R = m\lambda$, where n_{eff} is the effective refractive index of the medium experienced by the WGM field, R is the radius of the resonator, m is an integer number, and λ is the wavelength of the light. The evanescent tail of the WGM field probes the surroundings of the resonator and responds to the changes in the surroundings. The interaction of the evanescent WGM field and the analyte, which can be a biomolecule, a synthetic or biological particle, an aerosol, a protein, etc., enables the detection of the analyte or the changes taking place in the analyte without labeling.

Any changes in the surroundings, due to either a change in the refractive index or analyte molecules, particles or proteins entering the WGM evanescent field, lead to excess polarizability which is reflected in the transmission spectrum of the resonator either as a resonance shift (reactive shift) generally accompanied by linewidth broadening or as mode splitting. Figure 5.3 shows two typical experimental spectra depicting spectral shift (Figure 5.3(a)) and mode splitting (Figure 5.3(b)) phenomena observed with a microtoroid resonator.

WGM resonators, in particular the microtoroid resonators used in my experiments, have very high Q factors $(> 10^7)$, thus photons circulate over thousands of times within the circular boundary of the microtoroids, immensely increasing the interaction length between the evanescent field and the analyte. At the same time, the microscale mode volumes and very small mode areas of microtoroid resonators lead to unprecedented levels of light intensity, which further enhances the interaction, and thus improves sensitivity.
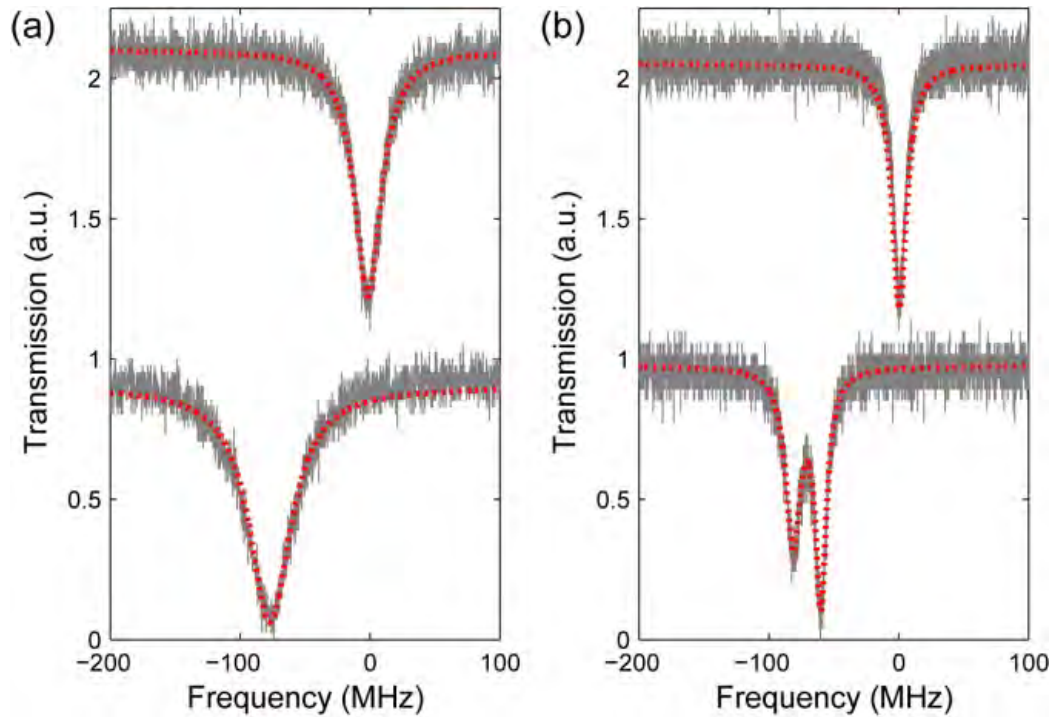
Figure 5.3. Reactive shift (resonance shift) and mode splitting spectra. As a response to a binding particle, a single WGM resonance (a) shifts to a lower frequency and experiences linewidth broadening or (b) undergoes mode splitting where two spectrally shifted resonances of different linewidths are obtained in the transmission spectra. Upper spectra are obtained before particle binding.

5.4.2 Theory of detection and measurement of nano-scale objects using mode splitting

WGM resonators support two modes of the same frequency but different propagation directions, i.e., frequency degenerate modes. In the presence of a scattering center (e.g., scatterer, nanoparticle, biomolecule, virus, or any structural inhomogeneity and surface

roughness, etc.), the WGM field interacts with the scattering center leading to elastic scattering, which mixes light fields of the counter-propagating modes within the cavity. Meanwhile, a portion of the light is lost to the environment. If the interaction strength is strong enough, the frequency degeneracy of the WGM resonator is lifted [25, 36, 40], leading to two spectrally different resonances (Figure 5.3(b)). Central frequencies and linewidths of these split resonances are different but are related to each other via

$$2g = -\frac{\alpha f(r)^2 \omega}{V} \qquad (5.12)$$

and

$$2\Gamma = \frac{\alpha^2 f(r)^2 \omega^4}{3\pi v^3 V} \qquad (5.13)$$

which define the spectral distance between the split modes (i.e., interaction strength), and the linewidth difference (i.e., due to scatterer-induced additional loss) between the split resonances, respectively. In these expressions, the effect of the particle is denoted by the particle polarizability α defined as

$$\alpha = 4\pi R^3 n_e^2 \frac{n_p^2 - n_e^2}{n_p^2 + 2n_e^2} \qquad (5.14)$$

, where spherical particle radius is R, particle refractive index is n_p, surrounding environment refractive index is n_e. The resonator related parameters are the pre-splitting initial angular frequency ω, the quality factor Q, mode volume V, the speed of light v in the medium, and the WGM field distribution characterized by $f(r)$. It is clear that mode splitting spectra carry the polarizability information from which size can be estimated accurately if n_p is known.

In mode splitting method, there is a transition from single resonance to a doublet (split resonances) or a change in the mode splitting spectra characterized by $2|g|$ and Γ, if a particle enters the mode volume. Polarizability of the particle is estimated by comparing the spectral properties of the splitting spectra just before and after the arrival of the particle using

$$\alpha = \frac{3}{8\pi^2}\left(\frac{\lambda}{n_e}\right)^3 \left|\frac{\gamma_N - \gamma_{N-1}}{\delta_N - \delta_{N-1}}\right| \qquad (5.15)$$

where γ_i and δ_i are the sum of the linewidths and resonance frequencies of the split modes after the arrival of the i-th particle, respectively. Zhu et al. have used this method to estimate the polarizability or size of gold, polystyrene, and influenza virus in dry environment [50].

The most interesting feature of the mode splitting method is that once the particle is detected, its polarizability can be estimated without knowing where the particle is

located in the mode volume. Moreover, since both of the split modes reside in the same resonator, they are affected similarly by the noise sources. Thus, the effects of these noises are automatically minimized, if not eliminated, without need for external referencing or stabilization schemes that increase complexity of the measurements, because one mode acts as a reference to the other mode. Mode splitting then provides a self-referencing platform.

In summary, mode splitting is a result of the scatterer-induced lifting of the inherit frequency degeneracy of WGM resonators. If mode splitting does not take place, then the frequency degeneracy of the WGM survives and transmission spectra show single resonance. Therefore, mode splitting method which relies on the spectral properties of split modes corresponds to "non-degenerate" sensing scheme whereas spectral shift method (reactive shift method) which relies on the shift in resonance frequency of a single mode (i.e., no mode splitting) corresponds to "degenerate" sensing scheme.

5.4.3 What determines the splitting spectra and the sensing performance?

Recent experiments and our study on nanoparticle detection using WGM resonators in dry and aquatic environments have shown that in some experiments only a spectral shift accompanied with linewidth broadening is noticed, whereas in some other experiments clear split modes are observed for the particles of the same size and refractive index [41, 50, 54, 55]. This, naturally, brings the question of under what conditions mode splitting

or the spectral shift takes place and what is achievable in each of these methods, in other words, what makes one preferable over the other.

The strength of the interaction of the WGM field with the nanoparticle (i.e., whether the particle is located at a strong or weak field region), the amount of excess polarizability (i.e., size of the particle and the refractive index contrast between the particle and the environment), quality factor of the resonator (i.e., linewidth of the resonance), and the noise level (e.g., laser frequency and amplitude fluctuations, wavelength scanning noise, electronic noise, etc) in the system determine whether resonance shift or mode splitting is observed and resolved in the transmission spectrum. In order to observe mode splitting, the interaction between the WGM field and the scatterer, such as a nano-scale object or material, should be strong enough to overcome the total loss (e.g., sum of the resonator and particle related losses) of the system. This condition can be re-stated as $2|g| > \Gamma + \omega/Q$, from which mode splitting quality factor is defined as $Q_{sp} = |2g|/(\Gamma + \omega/Q)$ [53]. In practical settings, various noise sources, such as laser intensity and frequency fluctuations, detector noise, taper-cavity gap fluctuations, and signal processing noise strongly affect the accuracy of measuring the resonance frequencies and the linewidths of the split modes. This, in turn, affects the Q_{sp} and the resolvability of mode splitting, as well as the accuracy of single-shot size measurement using mode splitting. In the presence of noise, higher Q_{sp} values are required to resolve splitting and to make highly accurate size measurements.

Figure 5.4(a) shows the expected the transmission spectra for Q_{sp} values in the range 0.6~1.2. It is seen that as Q_{sp} increases, the features of split modes become clearer. Thus, both the linewidths and the resonance frequencies of the split modes can be extracted using the curve fitting algorithm with high accuracy. For smaller values of Q_{sp}, it becomes difficult to extract the features accurately as the error in Lorentzian fitting to extract the resonance frequencies and the linewidth broadening increases with decreasing Q_{sp}. This leads to error in size estimation. For example, when $Q_{sp} = 0.6$, only one resonance mode with strongly broadened linewidth is observed. In such a case, either mode splitting is buried within the broad linewidth or it really has not taken place. I cannot discriminate between these two cases; therefore, it is difficult to arrive at an accurate conclusion.

I measured noise level in our system in aquatic environment before splitting took place (i.e., before nanoparticle binding while there was still a single resonance in the transmission spectra) in order to quantify its effects on the measurement results. I continuously acquired transmission spectra and performed Lorentzian curve fitting on selected resonance modes, and analyzed the statistics of the measured linewidth and resonance frequency. Resonance frequencies were repeatedly extracted with high accuracy for the selected modes. However, the same cannot be said for the linewidth measurements. I observed that the main source of error in our scheme is the linewidth measurement.

Standard deviations σ of linewidth measurements for resonance modes when the microtoroid was immersed in aquatic environment are depicted in Figure 5.4(b) and Figure 5.4(c). It is seen that for low Q modes (i.e., modes with larger linewidths), σ is larger and the dependency can be approximated by $\sigma = 0.47 \times \mu^{0.62}$ where μ is mean value of the measured single mode linewidth. Figure 5.4(d) depicts the dependence of the coefficient of variation, which is defined as the ratio of standard deviation σ to the mean value μ, on the Q value. The best fit to this experimentally obtained data gives the relation $\sigma/\mu = 3 \times Q^{0.34} \times 10^{-4}$.

For the range of nanoparticle sizes I aim to detect, linewidth broadening is much smaller than the amount of mode splitting, that is $2|g| > \Gamma$, and the quality factor of the resonance modes does not change much. Considering this point together with the results of the above experiments, I conclude that measuring $2|g|$ or the spectral shift is easier than measuring Γ in our system. Therefore, in the presence of noise linewidth measurement is the limiting factor for the accuracy of particle size measurement.

In order to accurately estimate the size of a detected nanoparticle, linewidth broadening 2Γ induced by the particle should be greater than the noise level (standard deviation) of measuring the linewidth difference. If the noise sources are neglected, I can measure any $\Gamma > 0$ without any problem. In the case of noise, however, the mode splitting observability criterion becomes much stricter, because in this case the scatterer induced

linewidth broadening should be larger than the fluctuations of the linewidth differences of the split modes.
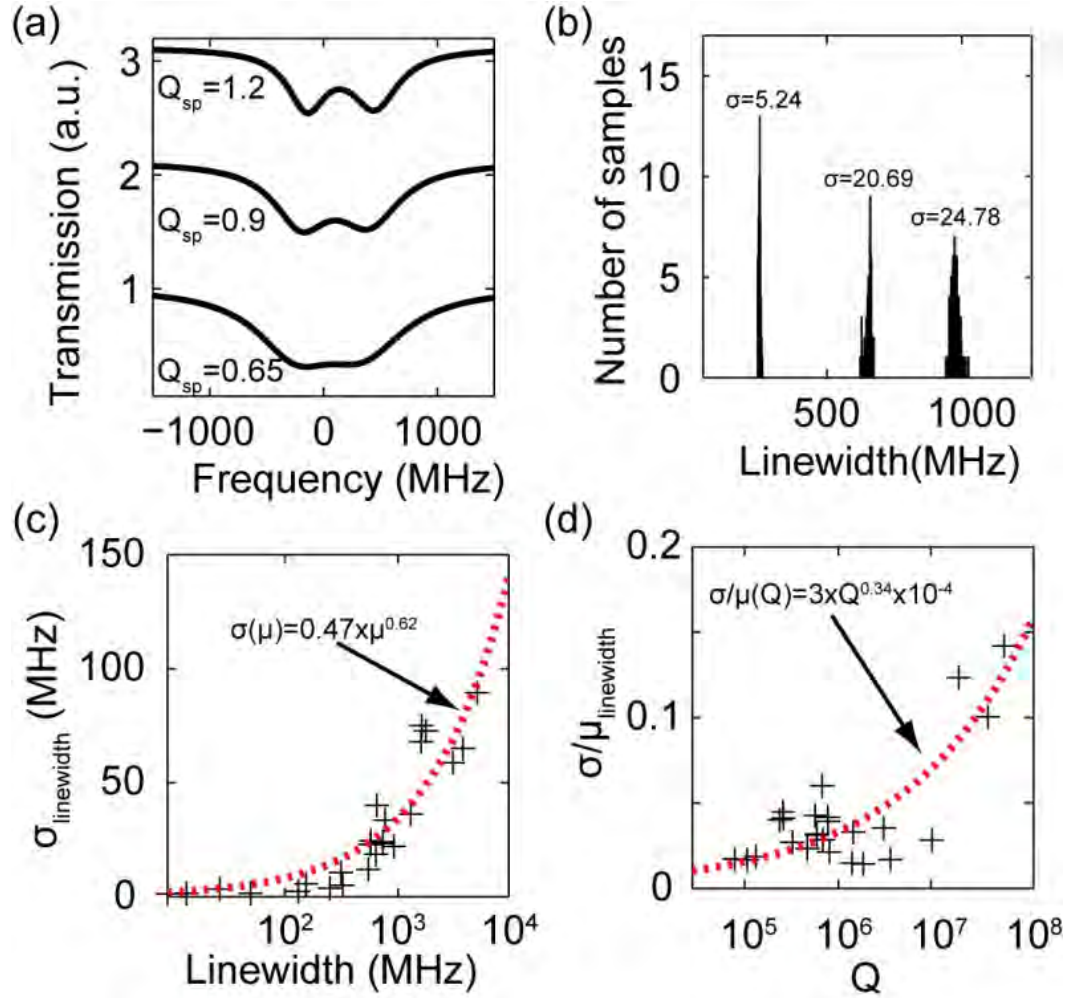
Figure 5.4. Resolvability characterization (a) Resolvability of the split modes in the transmission spectra and its relation with the splitting quality, Q_{sp}. The higher the Q_{sp} the better the resolvability of the doublets. (b) Standard deviation, σ, of the linewidth measurements obtained for three WGM resonances of different quality factors (linewidths) in the same microtoroid resonator in water. Standard deviation is higher for resonances of lower quality factors (larger linewidths). (c) Dependence of the standard deviations of the estimated linewidths as a function of the average linewidth μ. (d) Relation between the quality factor of a WGM resonance and coefficient of variation σ/μ.

Assuming that the coefficient of variation of linewidth measurements for each split mode is σ/μ, we can set a loose bound on Γ as $\Gamma > (\omega/Q)(\sigma/\mu)$. Consequently, we find that $Q > (\omega/\Gamma)(\sigma/\mu)$ should be satisfied to accurately measure the linewidth broadening (i.e., accurately estimating the polarizability and size of the particle) in a noisy system. Using the above relation, we find that for accurate estimation of linewidth broadening, quality factor of the resonance mode before the binding of the particle should satisfy $Q > \left(3 \times 10^{-4} \times \frac{\omega}{\Gamma}\right)^{1.51}$.

It is now clear that accurate size measurement in aquatic environment using split modes requires two conditions to be satisfied. (i) $Q_{sp} \geq \eta$ where η is a real number below which mode splitting cannot be resolved and single resonance appears in the transmission spectra. The value of η depends on the experimental conditions regarding the particle, the resonator and the noise in the system. $\eta \geq 1$ implies that there is more noise to deal with to clearly resolve split modes. (ii) $Q > (\omega/\Gamma)(\sigma/\mu)$ to assure accurate estimation of linewidth broadening and hence the polarizability and/or the size of the particle. Using (i) and (ii), we determine the smallest nanoparticle size R that can be detected and accurately measured using a WGM resonator of quality factor Q. Moreover, we can determine the parameter space bounded by Q and R in which the WGM resonator works in single or split mode regimes, and in which accurate size estimation is possible with mode splitting. There are four possible cases for the interaction between WGM resonators and nanoparticles. *(a) Both (i) and (ii) are satisfied simultaneously.* The sensing platform operates in the split mode regime with highly

accurate size measurement. *(b) Only (i) is satisfied.* Presence of particle is detected by splitting, however, size measurement will be erroneous due to the noise in linewidth measurement. *(c) Only (ii) is satisfied.* There is no splitting or splitting cannot be resolved as it is hidden in the broadened linewidth. Sensor operates in single mode regime and size measurement is possible if the shift in the single resonance can be detected. Note that none of the previously reported works based on reactive shift method has considered looking at the change in the linewidth of the single resonance mode. Instead, only shift in resonance has been considered. If the change in linewidth is measured in addition to the frequency shift, size measurement can be performed in such a way similar to mode splitting method. *(d) Neither (i) nor (ii) is satisfied.* Sensor is in single mode regime (either there is no mode splitting or splitting cannot be resolved) and linewidth measurement is erroneous. Particle might be detected via the changes in resonance frequency or linewidths, but accurate size measurement is not possible.

Since the size of the WGM microresonator affects the noise level and Q_{sp}, the boundaries of the four regimes discussed above should be different for resonators of different sizes. Figure 5.5 depicts the boundaries between different regimes for two microtoroids of different sizes assuming that the particle is at field maximum, and taking into account the observed noise level in our system when the measurements were done in aquatic environment. It is clear that single mode operation takes place for low Q resonators and nano-scale objects with smaller R. For a fixed particle size, mode splitting requires higher Q. In order to push the limits of measurable particle size to smaller values, resonators with higher Q values are required, which, on the other hand,

naturally leads to mode splitting. For example, from Figure 5.5(a) we see that with a resonator of $Q \geq 10^7$, mode splitting with $Q_{sp} \geq 1$ can be obtained for PS particles R≥35nm, implying that I can detect these particles but size measurement may contain error. For the present noise level I have in our system $Q > (\omega/\Gamma)(\sigma/\mu)$ is satisfied only for PS particles R≥50nm, implying that only these particles can be detected and measured with high accuracy. The amount of error decreases as Q_{sp} and Q becomes higher.
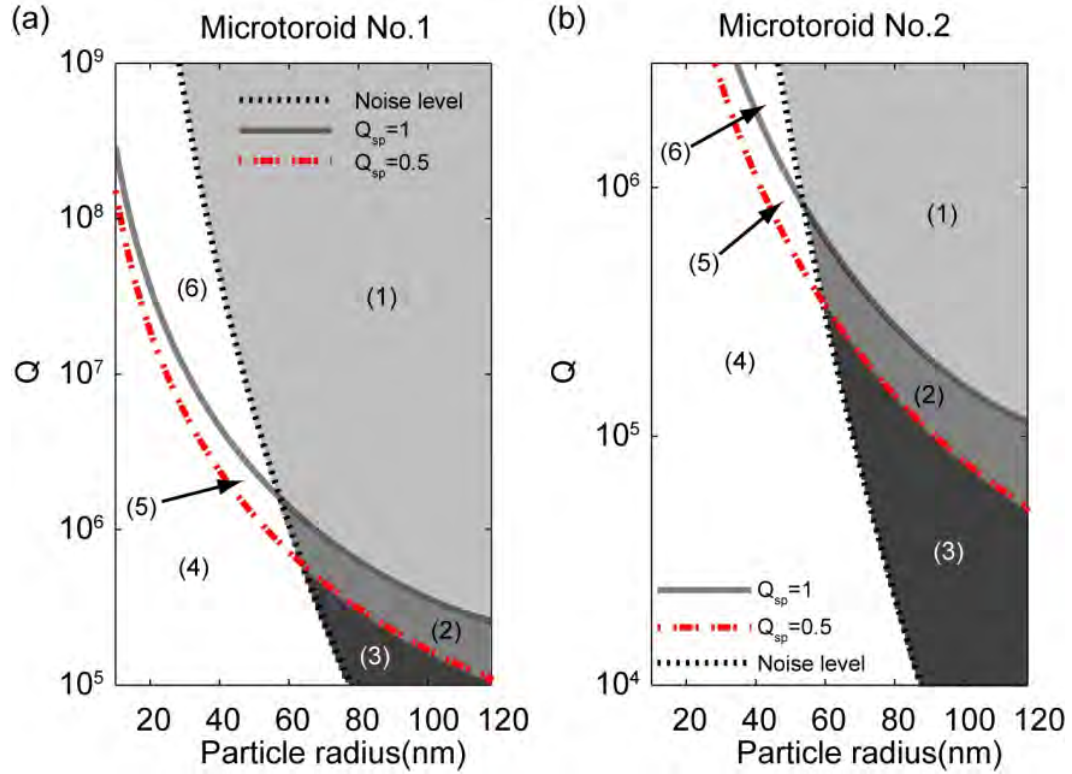
Figure 5.5. A WGM resonator will experience either reactive shift or mode splitting depending on the size of the binding PS particle, quality factor of the resonance, and the noise level in the system. There are four possible regions: (1) mode splitting with highly accurate size measurement, (2) mode splitting but with erroneous size measurement, (3) reactive shift (mode splitting cannot be resolved or does not take place) with accurate size measurement, and (4) reactive shift with erroneous size measurement. The areas of these regions depend on the diameter (D) of the resonator, (a) D=80μm, and (b) D=53μm. Dotted line shows the noise level measured in our experiments.

The four different regimes (a)-(d) characterized by the conditions (i) and (ii) are plotted in Figure 5.5 for the experimentally observed noise level, and for $\eta = 1$ and $\eta = 0.5$. For $\eta = 1$ in Figure 5.5(a), the operating regimes (a) and (b) are labeled as (1) and (6),

respectively, whereas (c) corresponds to the union of regions labeled as 2 and 3, and (d) is the region formed by the union of (4) and (5). For $\eta = 0.5$, on the other hand, (c) and (d) corresponds to regions (3) and (4), respectively, whereas (a) and (b) fall within the regions represented by the union of (1) and (2), and that of (5) and (6), respectively. Figure 5.5 clearly shows the dependence of the detection capability and the size measurement accuracy of mode splitting method on the resonator Q, PS particle size R, noise level in the system, and resonator size (i.e., mode volume). Decreasing the noise level in our system will improve our detection and size measurement limit. Also comparison of Figures 5.5(a) and 5.5(b) reveals that a smaller resonator leads to better detection limit, e.g., for $Q = 10^6$ and $\eta \geq 1$, lower detection limit for the toroid D=80μm is R=77nm (Figure 5.5(a)) whereas for the toroid D=53μm it is R=65nm (Figure 5.5(b)).

In Figure 5.5(a), I see that linewidth measurement noise is a limiting factor for accurately measurable size. For resonance shift method this limit is around R=64nm. To measure smaller particles, higher Q resonators should be used. In this case, one will inevitably enter the mode splitting region. For example, to accurately measure a particle of R=50nm, one cannot use resonance shift method. However, if Q is increased to around 10^7, mode splitting method will allow accurate measurement. Detection limit, on the other hand, is determined by the noise of resonance frequency measurement, which is much lower than the noise in linewidth measurement. For the detection limit, we have two cases. First, if initially there is no mode splitting, resonance shift method,

in principle, has lower detection limit, because for the same resonator, resolvability condition of mode splitting requires higher quality factor. Second, if there is an initial splitting (e.g., intrinsic splitting or splitting induced by a previous particle), mode splitting is more sensitive because both modes of the splitting will be affected by an incoming particle, experiencing a total shift of twice that of the shift of a single mode case. Therefore, signal arising from the same particle is larger in mode splitting case, which implies that one can lower detection limit beyond that of resonance shift.

5.4.4 Detection and size measurement of individual PS nanoparticles in aquatic environment using mode splitting

Here, I report the first experimental demonstration of mode splitting based nanoparticle detection and size measurement in aquatic environment. Previously, I have reported mode splitting in aquatic environment; however, I could not reach single nanoparticle resolution, thus size measurement could not be performed. On the other hand, Ref. [64] has reported single nanoparticle resolution without being able to perform single-shot size measurement of the binding particles. In this chapter, I have successfully detected and measured the size of individual PS nanoparticles using mode splitting in aquatic environment.

Figure 5.6 shows the results of experiments performed in aquatic environment for PS nanoparticles of R=75nm using a microtoroid resonator of major diameter D=80μm.

The resonance mode used in the experiments was initially degenerate (no observable mode splitting) and had quality factor $Q = 6 \times 10^6$. Experiments were performed using a solution of PS nanoparticles in deionized water with a concentration of approximately 1nM. The solution was injected into the chamber continuously while the transmission spectra were monitored and size was estimated continuously. Figure 5.6(a) shows a series of particle binding events reflected in the splitting amount $2g$ as discrete upward and downward jumps above the noise level. The inset depicts two typical largely separated and well-resolved split resonances in the transmission spectra. Splitting quality factors of the events in Figure 5.6(a) lay in the range $0.02 \leq Q_{sp} \leq 1.42$. I find that the estimated size of each detected particle differs although the average value of <R>=75.8nm is in good agreement with the size distribution provided by the manufacturer as R=75±2.2nm. I find that the results in Figure 5.6(b) obtained from single-shot size measurement of each detected nanoparticle in the aquatic environment have a good match with the results of DLS measurements shown in Figure 5.6(c), and those of mode splitting experiments in air which yielded <R>=76.5nm with a standard deviation of 9.2nm. I tested particles from the same batch under SEM and estimated an average size of 75.1nm. Estimated average sizes are in good agreement in all the methods tested in this study.

In Figure 5.6(b), there are three cases in which the estimated radii R=188.8nm, R=203.8nm and R=317.9nm are far larger than the nominal size of R=75nm for this batch of particles. When I looked closely to the mode splitting spectra for these three events, I found the corresponding Q_{sp} values as $Q_{sp} = 0.49$, $Q_{sp} = 0.31$, and $Q_{sp} =$

0.70. This suggests that although for the events with $Q_{sp} = 0.49$ and $Q_{sp} = 0.70$, the condition (i) is satisfied, but the condition (ii) is not, whereas for the event with $Q_{sp} = 0.31$, neither (i) nor (ii) is satisfied. Thus, for these events size estimation errors are expected.
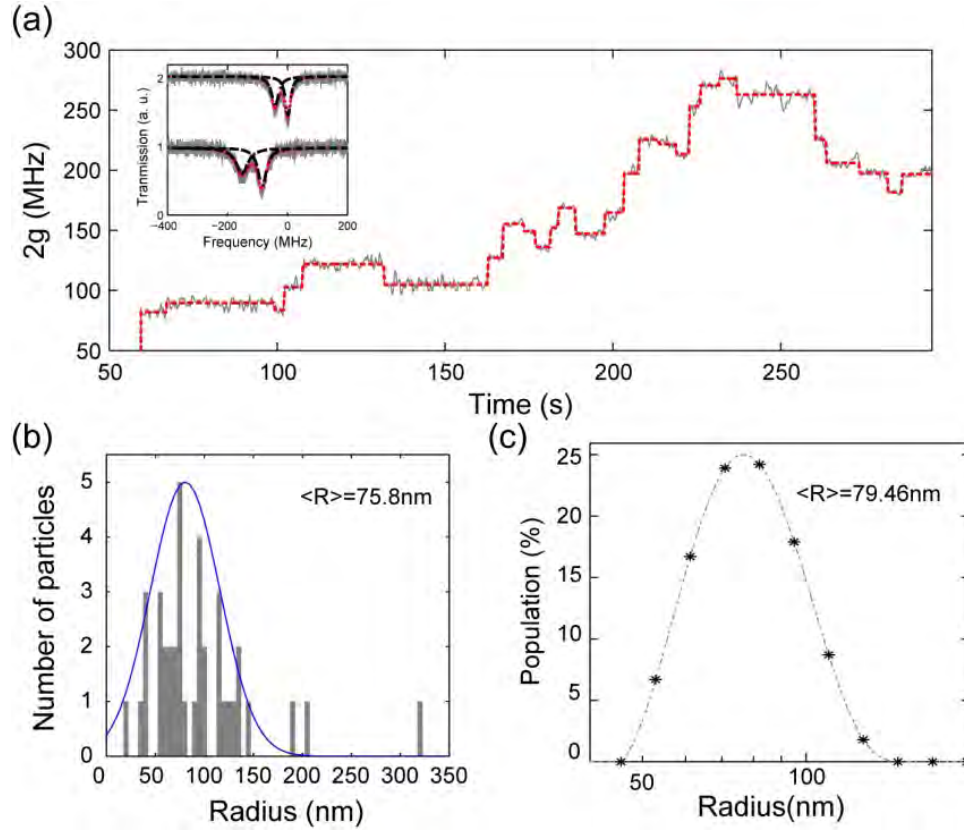
Figure 5.6. Mode splitting based detection and single-shot size measurement of individual polystyrene (PS) particles of nominal size R=75±2.2nm binding to a microtoroid placed in aquatic environment. (a) Change in the amount of mode splitting as the particles enter the mode volume of a microtoroid one by one. Inset depicts typical particle induced transitions from a doublet to another doublet in the transmission spectra. (b) Distribution of the estimated size of detected particles. (c) Size distribution obtained from dynamic light scattering measurements (DLS) for the same particles.

Results presented in Figure 5.6 and the discussions above reveal that the conditions given in (i) and (ii) are very important for accurate size measurement. I looked closer at Figure 5.6(b) and quantified how the choice of η in condition (i) affects the size

measurement in order to set a threshold η above which size measurement will be highly accurate, and below which size measurement is unreliable. I found that by taking only the events for which $Q_{sp} \geq 0.43$, size measurement yields 73.3nm≤R≤75.9nm. In the distribution depicted in Figure 5.6(b), I observed that the events falling within 1σ of the mean <R>=75.8nm have $0.26 \leq Q_{sp} \leq 1.42$ leading to estimated sizes in the range 40.4nm≤R≤102.3nm, whereas for those within 2σ, lower bound of Q_{sp} decreases down to 0.20 shifting the estimated sizes to the range 19.5nm≤R≤143.4nm. For $Q_{sp} \leq 0.43$, estimation error increases.

5.4.5 Detection and measurement of hemozoin in air and in aquatic environment

I report results of a series of experiments done to test the performance of mode splitting method in detecting and estimating the size of hemozoin crystals both in air and in aquatic environment. This is the first time hemozoin is detected and measured using a WGM optical microcavity. In mode splitting and DLS experiments, I take the refractive index of hemozoin as 1.44 as reported in the literature [71].

The first set of experiments with hemozoin crystals were performed in dry environment. First, I deposited hemozoin particles on a microtoroid resonator using the DMA, and analyzed it under SEM. Figure 5.7(a) shows an SEM image of the microtoroid with synthetic hemozoin particles. The estimated sizes of the two hemozoin crystals in the

image are R=143.2nm and R=141.0nm. Next, I continuously deposited hemozoin crystals onto a microtoroid resonator one-by-one and monitored the transmission spectra. As expected with the first particle, mode splitting took place and with each subsequently detected particle mode splitting spectra were modified. In Figure 5.7(b), I depict nine consecutive single hemozoin binding events where discrete upward and downward jumps are clearly observed. Each of these discrete jumps corresponds to one hemozoin binding event. I measured the size of each detected hemozoin crystal and estimated the mean size, R=159.2nm. Note that the size obtained from the mode splitting method here is the size of a spherical particle having the same refractive index as hemozoin and leading to the same excess polarizability as the deposited hemozoin crystal.

The second set of experiments was performed in aquatic environment. Using samples from a hemozoin solution of concentration ~1mM stirred by a sonicator, I first performed DLS measurements whose results are shown in Figure 5.7(c). The mean size of hemozoin crystals in this solution was calculated as R=160.7nm using the mean values obtained from multiple runs of DLS. Finally, I performed mode splitting experiment in aquatic environment using hemozoin crystals. The solution used in this experiment has a concentration of ~100fM. Figure 5.7(d) depicts nine consecutive discrete upward or downward jumps in $2g$ corresponding to nine hemozoin binding events. I estimated the average size of hemozoin crystals as R=160.9nm.
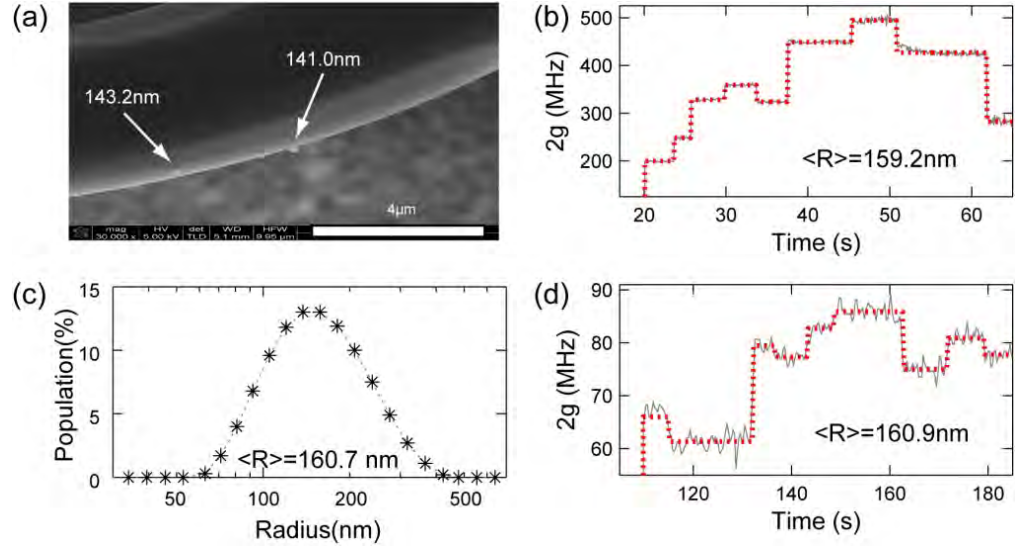
Figure 5.7. Detection and measurement of hemozoin crystals. (a) SEM image of hemozoin crystals deposited on a microtoroid resonator. (b) The amount of mode splitting induced by consecutively deposited hemozoin crystals on a microtoroid. Experiments were done in air. (c) Typical size distribution obtained from DLS measurements for the hemozoin crystals. (d) Result of mode splitting experiment performed in aquatic environment for hemozoin crystals. Discrete jumps in (b) and (d) signals that a hemozoin is within the mode volume of the resonator.

5.4.6 Polarizability of hemozoin depending on polarization and posture

The underlying physics of our experiments is the induced polarization by the cavity field on the nanoparticle or the hemozoin crystal staying within the mode volume. The strength of the induced polarization is a function of the properties of the particle (e.g., shape, dimensions, orientation, and refractive index) and the cavity field (e.g.,

polarization: transverse electric (TE) or transverse magnetic (TM)) interacting with the particle. In general, it is expected that TE and TM waves will induce different polarizabilities, because they have different field components: TE wave has only a tangential component whereas TM wave has both tangential and normal components. For microtoridal resonators with small minor diameters, non-transverse electric field components are relatively small when compared to the transverse component and hence can be neglected. Thus, for such resonators polarizing fields are tangential and normal components of TE and TM modes. Similarly, the orientation of the particle or the crystal on the resonator surface has tangential and normal components; therefore, it is expected that for particles of irregular shapes, different orientations will result in different polarizabilities for a fixed field mode.

For a particle deposited on the resonator with a fixed orientation, we can define polarizability to have a tangential a_t and a normal a_n component such that TE and TM modes, respectively, induce a_t and a_n. Note that polarizability of a spherical particle is the same for TE and TM modes and for all of its possible orientations, provided that the microsphere is completely within the cavity field, and it is simply given as

$$\alpha = 4\pi R^3 n_e^2 \frac{n_p^2 - n_e^2}{n_p^2 + 2n_e^2} = 3\pi V_p n_e^2 \frac{n_p^2 - n_e^2}{n_p^2 + 2n_e^2} \qquad (5.16)$$

where V_p is the volume of the particle. It has been shown in a series of papers by the group of S. Arnold and the others that the polarizability of a rod-like particle (i.e.,

similar to hemozoin crystals in this work) is different for different polarizations of the resonator field as well as for different orientations of the particle on the resonator surface (i.e., when it is standing or laying on the surface for fixed polarization) [42, 72-75]. For a rod-like particle making an angle θ with the surface of the resonator and φ around its axis, polarizabilities are given as

$$\alpha_{TE} = \xi_1(1 - sin^2\theta cos^2\varphi) + \xi_2 sin^2\theta cos^2\varphi \tag{5.17}$$

$$\alpha_{TM} = \xi_2 sin^2\theta + \xi_2 cos^2\theta \tag{5.18}$$

where $\xi_1 = 2(n_p^2 - n_e^2)/(n_p^2 + n_e^2)$ and $\xi_2 = 1 - n_e^2/n_p^2$. Rod-like particle is laying on the surface when $\theta = 0$, and standing on the surface when $\theta = \pi/2$. The latter is highly unlikely to be observed when a rod-like particle is deposited on microtoroid resonator. Thus, the observed mode splitting spectrum in these experiments should also change with the cavity mode and the orientation of the particles/crystals because of its dependence on the polarizability via the defining expressions $2g = -\frac{\alpha f(r)^2\omega}{V}$ and $2\Gamma = \frac{\alpha^2 f(r)^2\omega^4}{3\pi v^3 V}$. However, in these experiments I could not see any significant change in the estimated polarizabilities when the polarization was changed. Moreover, numerical simulations with COMSOL reveals that they also have different field distributions as well as slightly different mode volumes; thus $2|g|$ and 2Γ will be affected by the polarization of the mode and the orientation of the particle. However, when I take their ratio as I did for size estimation, arriving at Eq. (5.15), the dependence on generally unknown parameters $f^2(r)$ and V is eliminated. For a particle deposited

on the resonator with a fixed orientation, experiments with TE and TM modes will reveal α_{TE} and α_{TM} from the experimentally observed spectra and known resonance wavelengths of the TE and TM modes. Denoting the experimentally observed splitting amount and the linewidth differences as $2|g_{TE}|$ and $2\Gamma_{TE}$ for the TE mode and $2|g_{TM}|$ and $2\Gamma_{TM}$ for the TM mode, we arrive at

$$\frac{\alpha_{TE}}{\alpha_{TM}} = \left(\frac{\lambda_{TE}}{\lambda_{TM}}\right)^3 \frac{\Gamma_{TE}}{\Gamma_{TM}} \left|\frac{g_{TM}}{g_{TE}}\right| \sim \frac{\Gamma_{TE}}{\Gamma_{TM}} \left|\frac{g_{TM}}{g_{TE}}\right| \qquad (5.19)$$

where I have assumed that the resonance wavelengths λ_{TE} and λ_{TM} of the TE and TM modes differ only slightly and hence their ratio can be approximated to 1. Therefore, I should be able to resolve any change in the splitting spectrum when the mode is changed from TE to TM or vice versa if the particle has a non-spherical shape and the difference of polarizabilities for TE and TM modes is sufficiently large. In Figure 5.8, I show α_{TE}/α_{TM} for a spherical particle as well as for a rod-like particle with various orientations θ and φ as a function of n_p the refractive index of the particle assuming that the volume V_p of the particle is fixed. It is clear that α_{TE}/α_{TM} is always 1 for a spherical particle regardless of n_p its refractive index. However, for a rod-like particle, which is depicted as a nano-cylinder here, α_{TE}/α_{TM} changes with the orientation and refractive index of the particle. It is interesting to see that as the particle refractive index decreases, α_{TE}/α_{TM} decreases for all orientations of the particle. For a rod-like particle having refractive index 1.44 (i.e., this is the refractive index for the hemozoin crystals) or smaller, α_{TE}/α_{TM} is very close to 1 suggesting that for such rod-like particles, it is

very difficult to discriminate among orientation dependent polarizability values. For example for $\varphi = 0$, I find α_{TE}/α_{TM} equals to 1.079 and 0.93, for $\theta = 0$ (laying on the surface) and $\theta = \pi/2$ (standing on the surface), respectively. Similarly, for $\varphi = \pi/2$, I find α_{TE}/α_{TM} equals to 1.079 and 1, for $\theta = 0$ and $\theta = \pi/2$, respectively. It is clear that for the non-extreme orientations, α_{TE}/α_{TM} approaches to 1 and it becomes much more difficult to measure or observe the changes. Detecting such small differences of the resonance frequencies and linewidths of split modes with significant amount of noise (e.g., electrical noise, laser noise, and the signal processing noise) is very difficult. I believe that this is the main reason why I could not observe change in the estimated polarizabilities.
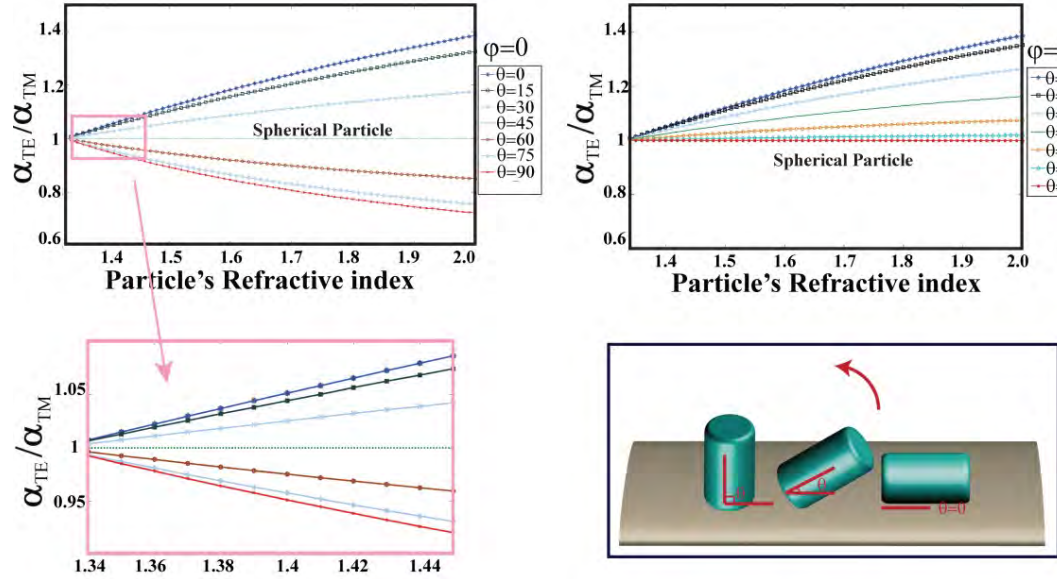
Figure 5.8. The ratio α_{TE}/α_{TM} of the polarizabilities α_{TE} and α_{TM} of a rod-like particle with fixed volume making an angle θ with the resonator surface and orientation φ when the field is TE and TM, respectively, as a function of the refractive index of the particle.

In an experiment, α_{TE}/α_{TM} is estimated by comparing the mode splitting spectra obtained for TE and TM modes. In order to do this estimation, the first condition is to be able to resolve mode splitting spectra for the same particle when the mode is TE and TM according to the resolvability criterion $2|g| > \Gamma + \omega/Q$. I performed numerical simulations using COMSOL and obtained resonance wavelengths, quality factors, mode volumes, and field distributions for a microtoroid of similar size that I used in the experiments as a function of the volume of a rod-like particle with refractive index of 1.44 and $\varphi = 0$. For each particle volume, I estimated α_{TE} and α_{TM} from Eqs. 5.17 and 5.18, and then used these values and parameters estimated from COMSOL simulations in Eqs. 5.12 and 5.13 to find $2|g_{TE}|$ and $2\Gamma_{TE}$ for the TE mode and $2|g_{TM}|$ and $2\Gamma_{TM}$ for the TM mode and plotted them in Figure 5.9. Note that in these simulations, I chose the location of the particle in the field such that maximal values are obtained for the depicted parameters. Even under these optimal conditions, it is clear that when the volume of the rod-like particle is small, it becomes very difficult to observe differences in these measurable parameters. In an experiment, additional noises will make it even more difficult to observe small changes in these measurable parameters. In short I believe that due to the low refractive index contrast between the hemozoin crystal and the water, and the small size (volume) of the hemozoin crystals the polarizability values for TE and TM modes are already very small. Moreover, the possible orientations that these crystals take on the resonator surface do not maximize polarization dependent poalrizability changes so that such changes are observed in noisy experimental conditions. It may be the case that if I deposit sufficiently large number of crystals to

achieve a higher resonator surface coverage, then such small changes may be amplified to be observed.
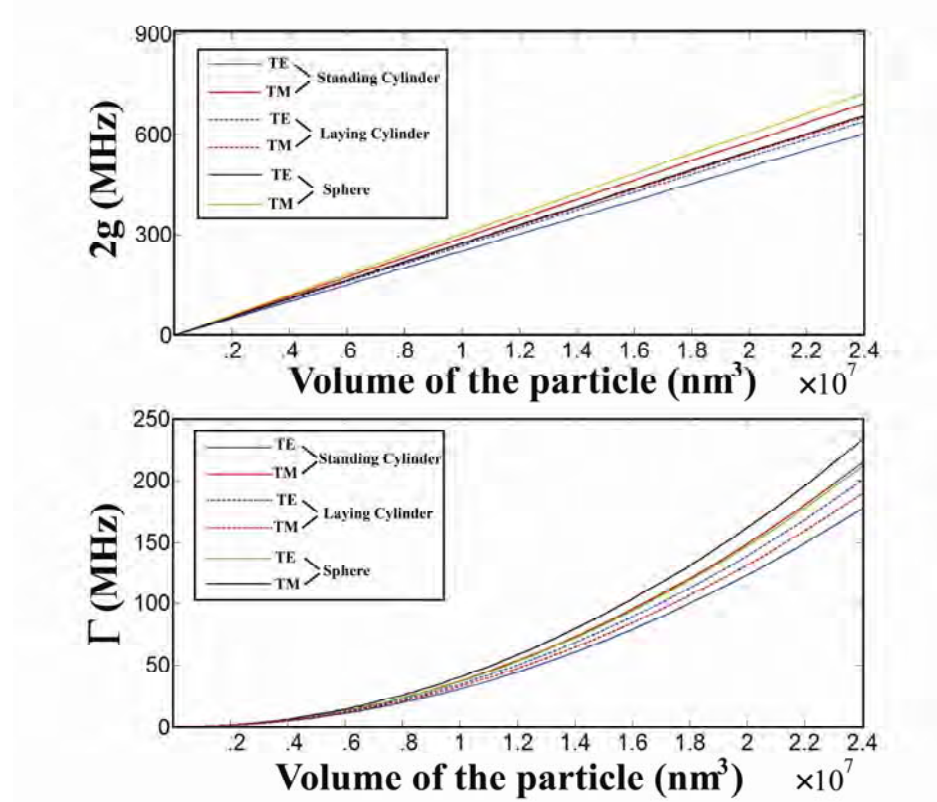

Figure 5.9. Numerical simulation results showing the dependence of the amounts of mode splitting and the linewidth broadening induced by a single rod-like particle as a function of its volume for different polarizations of the resonator field and the orientation of the particle on the resonator.

5.5　Conclusions

In conclusion, I report the first single nanoparticle detection and size measurement in aquatic environment using mode splitting in a WGM resonator. I have achieved detecting and measuring PS nanoparticles of nominal radii 75nm. In addition, I tested the performance of our platform using synthetic hemozoin crystals, showing the detection and size measurement of individual hemozoin crystals. Moreover, I have characterized splitting quality factor that can be used to determine mode splitting observability in response to light scatterers, such as nanoparticles, in the mode volume of a resonator and obtained the relation between the quality factor of a resonance mode and the noise level in the system, which have been used to identify operating regimes of a WGM resonator: (i) The non-degenerate region where mode splitting takes place, lifting the degeneracy and leading to a doublet in the transmission spectra upon binding of a particle, and (ii) The degenerate region where transmission spectra shows a single resonance which undergoes reactive shift or linewidth broadening upon the binding of a particle to the resonator. Within each of these regions, there are sub-domains within which noise level in the system determines whether accurate size measurement can be done or not. I have identified the linewidth measurement noise as the main source of error in the accuracy of size measurement.

I have found that resonators with high-Q modes favor mode splitting (non-degenerate regime) whereas those with lower Q favor reactive shift and single mode operation (degenerate regime). I believe that the findings in this chapter provide an answer to the ongoing debate on mode splitting and spectral shift methods, and can be used as a guide for the future studies.

Control and desired eradication of malaria parasites requires rapid and sensitive detection techniques for immediate and effective treatment. This study for the first time shows that detection of single hemozoin crystals, which are the signature of malaria parasites, can be achieved by WGM. Therefore, detection and measurement of individual hemozoin crystals in aquatic environment opens the way for highly sensitive early-phase detection of malaria infection from serum. These results bring us one step closer to single particle or single molecule detection in aquatic environment using mode splitting.

Chapter 6

Computational investigation for an arbitrary shape scatterer polarizability

In this chapter, I performed a computational study for an abtrary shape nanoparticle polarizability by using discrete dipole approximation (DDA) theory. As I briefly presnted in the previous chapter, nanoparticle shape affects sensing signal. Because amount mode splitting and particle polarizability are directly related, an arbtrary shape nanoparticle polarizability which differs from spherical shape one is studied.

6.1 Summary

Hemozoin crystal shape looks like a rod, instead of a spherical shape. Here, I computationally investigate arbitrary shape nanoparticle polarizability. As described previously, since our sensing scheme, mode splitting, is related with particle polarizability, its study is necessary. Discrete dipole approximation (DDA) provides powerful solution to understand an arbitrary shape nanoparticle. By breaking down a big particle into multiple small spherical particles, DDA calculates particle properties individually. Then, it considers interaction among particles, and ultimately DDA results in overall optical property of the arbitrary particle. Here, I prove the validity of DDA

compared to published works, define particle geometry by using a mathematical guideline, and investigate feasibility of distinguishing sensing signal induced by TE or TM mode.

6.2   Introduction

Shapes of many biological nanoscale objects are illregular, for instance, heart-shaped protein and hemozoin crystal. Especially, hemozoin crystal is rod-shape nanoscale object. Recent studies show that TM mode incident light induced polarizability of rod-shape nanoscle object is different from TE mode incident light induced polarizability [72, 74]. Definition of particle geometry is important, because depending on the definition polarizability can be different as shown in [72, 74]. For instance, standing rod TE polarizability is defined as

$$\frac{\alpha_{TE}}{\varepsilon_0 V_p} = 2\varepsilon_e \left(\varepsilon_p + \varepsilon_e\right)^{-1} \left(\varepsilon_p - \varepsilon_e\right) \qquad (6.1)$$

, where V_p is particle volume, ε_p is particle permittivity, and ε_e is environment permittivity. In other case, if it is a disk lying on the surface, the polarizability becomes

$$\frac{\alpha_{TE}}{\varepsilon_0 V_p} = \varepsilon_p - \varepsilon_e \qquad (6.2)$$

However, these studies didn't provide the definition of rod. Therefore, polarizability calculation can be errorous, which leads to inaccurate coupling strength and additional damping ratio.

In order to provide detailed optical property of an arbitraty shape particle, advanced computational is introduced, discrete dipole approximation (DDA) [76-81]. DDA treats a big object as a group of small dipoles as shown in Figure 6.1. As an example, a red blood cell (RBC) constructed with multiple dipoles as Fung et al. [82] work that describes the structural geometry. Based on their work, the RBC can be modeled as a biconcave discoid. Following equation describes its shape:

$$T(x) = 0.65d\sqrt{1-x^2}(0.1583 + 1.5262x^2 - 0.8579x^4) \qquad (6.3)$$

, where T represents the RBC thickness, x is the ratio of radial cylindrical coordinate to diameter of the RBC. As shown here, each dot is considered as an individual dipole constructing the target object.
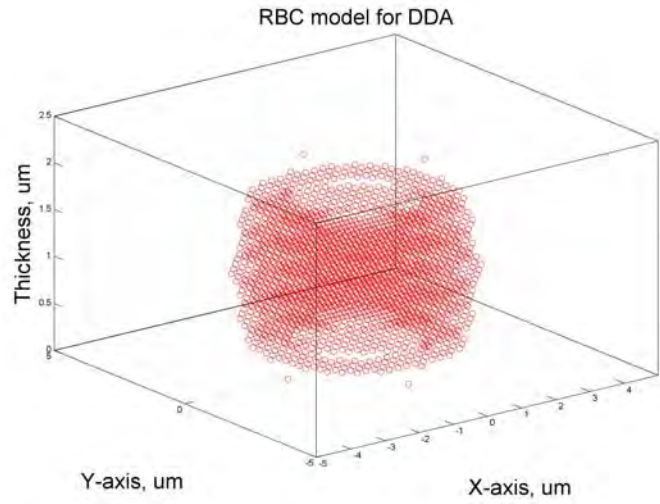
Figure 6.1. Red bood cell model for DDA calculation. Each hollow circle is considered as individual dipole.

DDA calculation is based on classical electromagnetic theory interacting with a small dipole. Main goal of DDA is to calculate dipole moment of each dipole by solving linear equation shown in Figure 6.2 [79]. The dipole moment is used for advanced calculation.

Figure 6.2. Linear equation for dipole moment calculation, consisting of the interaction matrix (A), the unknown dipole moments (P), and the incident field (E$_{inc}$) (Copy from Loke et al.'s 2011 work)

The dipole memoent calculation procedure is following.

1. Create dipole coordinate

2. Assign the polarizability α to each dipole

3. Calculate the incident field E$_{inc}$ at each dipole

4. Define the interaction matrix A

5. Solve the linear equation for P

6.2.1   Defining dipole lattice

Note: DDA simulation description is based on Loke et al.'s work [79].

The scatterer is assumed to be Rayleigh scatterer with polarizability α located on a position, r, as shown in Figure 6.1. The variable r indicates each location of the dipole. Note that the coordinate values should be converted proper wavelength units. If the conversion is not proper, all calculations are not valid. The minimum number of dipole required to represent the scatterer is determined by overall volume and operating wavelength [81]. In order to consider an object as a Rayleigh scatterer, the lattice spacing should be defined as

$$d \leq \left(\frac{1}{k|m|} \right) \qquad (6.4)$$

, where d is equal spaced lattice, m is the relative refractive index to environment and k is wavenumber.

6.2.1   Assigning polarizability

Dipole moment P is product of polarizability α and applied electric field E.

$$P_j = \alpha_j E_j \qquad (6.5)$$

In this DDA lattice dispersion relation [80] is applied based on Clausius-Mossotti polarizability.

$$\alpha_j^{CM} = \frac{3d^3}{4\pi}\left(\frac{m_j^2-1}{m_j^2+2}\right) = \frac{3d^3}{4\pi}\left(\frac{\varepsilon_j-1}{\varepsilon_j+2}\right) \tag{6.6}$$

$$\alpha_j^{LDR} = \frac{\alpha_j^{CM}}{1 + \frac{\alpha_j^{CM}}{d^3}\left[(b_1 + m^2 b_2 + m^2 b_3 S)(kd)^2 - \frac{2}{3}i(kd)^3\right]}$$

$$, b_1 = -1.89, b_2 = 0.16, b_3 = -1.77, S \equiv \sum_{j=1}^{3}\left(\hat{a}_j\hat{e}_J\right)^2 \tag{6.7}$$

, where $\hat{a}_j$ and $\hat{e}_j$ are the unit vectors defining the direction and polarization of the incident light.

Based on above equations, polarizability calculation is performed all three directions, x, y, and z, because it depends on incident light field. In the Matlab toolbox that Loke et al. provided, 'alph=polarizability_CM(lattice, refractive index)' and 'alph=polarizability_LDR(lattice spacing, refractive index, wave vector, electric field polarization)' are the functions for polarizability calculation.

6.2.3   Multiple dipoles interaction

Now let's consider the interaction among individual dipoles, defining interaction matrix A. From Eq. (6.5), the diagonal tensor can be defined as $A_{jj} = \alpha_j^{-1}$. Relationship between applied field and dipole moment can be expressed as [37]

$$E_{inc,j} = \sum_{k=1}^{N} A_{jk} P_k \qquad (6.8)$$

Here, A_{jk} is considered as interaction tensor matrix for all dipoles and directions. The dipole responds not only to the incident light, but also it re-radiates so that surrounding dipoles respond to the incident light from the dipole. This relationship leads to the interaction matrix.

$$A_{jk} = \frac{\exp(ikr_{jk})}{r_{jk}} \left[k^2 \left(\hat{r}_{jk} \hat{r}_{jk} - 1_3 \right) + \frac{ikr_{jk}-1}{r_{jk}^2} \left(3\hat{r}_{jk} \hat{r}_{jk} - 1_3 \right) \right], j \neq k \qquad (6.9)$$

, where r_{jk} is the distance between two dipoles. Toolbox function 'A=interaction_A(k, r, alph)' constructs the interaction matrix.

6.2.4   Incident field

The dipole can be influenced by any types of incident electric field, for example, plane wave and evanescent field. Electric field can be described as, $E_{inc,j} = E_0 \exp(ikr_j)$.

'Ei=E_inc(E0, kvec, r)' function provides the incident electric field, where E0 is electric field amplitude, wave vector, and r is the coordinate vector. For the microtoroid application, the incident field needs to be evanescent field. Matlab toolbox also provides it, '[kvec, E2s, E2p]=evanescent_E(E1s, E1p, gamma, n_1, n_2)', given the incident TE (E1s) and TM (E1p) E-field. 'gamma' is incident angle. The outcome feeds into the standard function for electric field calculation, Ei=E_inc(E2s+E2p, kvec, r).

6.2.5   Solving the linear equation

With knowing how to construct interaction matrix and defining the incident electric field, solve the linear equation in Figure 6.2 can be done. Since the accuracy of least square solution of Matlab is not enough, P=A|Ei is not appropriate methodology to choose. However, accurate iterative method requires significant amount of time. Therefore, there are intermediate iterative functions to solve the linear equation, minres(A, Ei), gmres(A, Ei), and qmr(A, Ei). Different approaches can be found in [83].

6.3   DDA validation

Particle polarizability tensor matrix is important parameter, because it implies particle size information. In DDA computation, the polarizability is calculated by taking inverse

matrix of the interaction tensor matrix. In accordance to TE and TM mode polarizability definitions in previous works [72, 74], TE mode polarizability is when the scatterer feels the propagating field parallel to the interface between resonator and environment, while TM mode polarizability is when the scatterer feels the propagating field perpendicular to the interface. Here, I focus on a rod-shape scatterer. For instance, if the rod-shape scatterer is standing on the surface, TE and TM mode polarizabilities are defined as Eq. 6.1 and 6.2, respectively.

I verify the DDA is properly functioning by comparing with published works or cross methodology. In Yi et al.'s work [72], they provided analytical expression of TE(TM) mode polarizability as a function of scatterer posture angle shown in Figure 6.3.

$$\frac{\alpha_{TE}}{V_p} = \frac{2(\varepsilon_p - \varepsilon_e)}{(\varepsilon_p + \varepsilon_e)}(1 - \sin^2\theta\cos^2\varphi) + \left(1 - \frac{\varepsilon_e}{\varepsilon_p}\right)\sin^2\theta\cos^2\varphi, \text{ for TE} \qquad (6.10)$$

$$\frac{\alpha_{TE}}{V_p} = \frac{2(\varepsilon_p - \varepsilon_e)}{(\varepsilon_p + \varepsilon_e)}\sin^2\theta + \left(1 - \frac{\varepsilon_e}{\varepsilon_p}\right)\cos^2\varphi, \text{ for TM} \qquad (6.11)$$
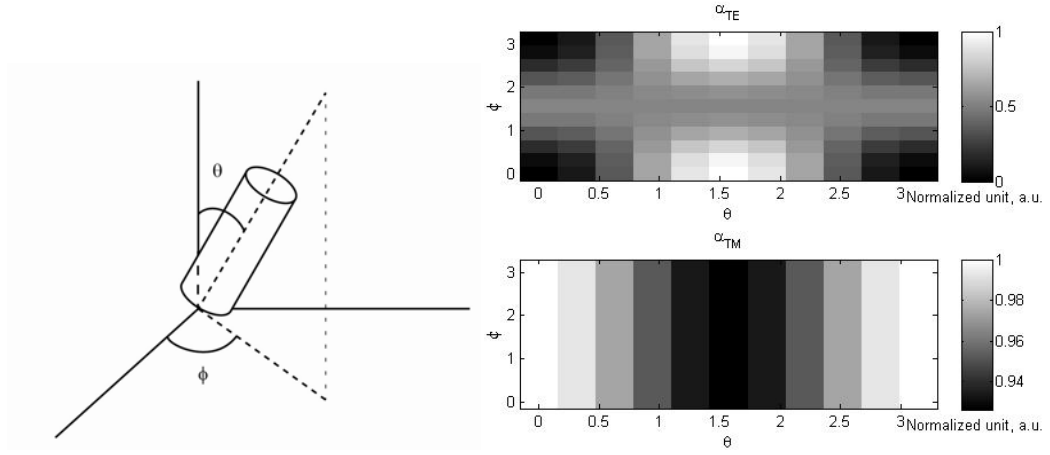
Figure 6.3. Based on analytical expression, TE and TM mode polarizability of a rod-shape

For comparison, DDA calculated polarizabilities in each direction when the incident light propagates in x-direction are shown in Figure 6.4. Thus, α_x and α_y are considered as TE mode polarizability, while α_z is considered as TM mode polarizability. As shown, the DDA calculated polarizability (Figure 6.4) agrees with the published work (Figure 6.3). In this simulation, the radius and height of rod are 100nm and 200nm, respectively. The refractive index of the particle and environment are 1.44 and 1.33, respectively. For DDA calculation, 670nm wavelength source is used and lattice distance is 25nm.
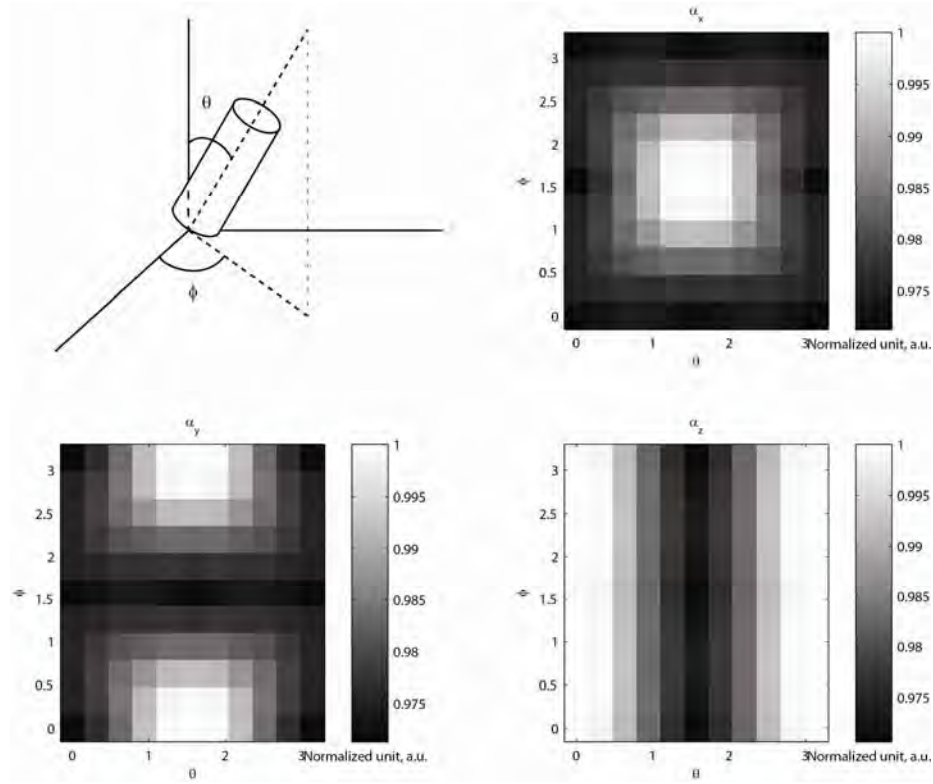
Figure 6.4. DDA calculated polarizability on each direction.

Second verification was done by comparing two different methodologies for polarizability calculation. First method is same as previous method, inverse matrix of interaction tensor matrix. Second method is following. By applying randomly propagating incident light, dipole moment can be obtained. Then, input incident light becomes system matrix and one axis dipole moment is output matrix. Ultimately, linear system equation solver finds out input matrix, which is equivalent to polarizability tensor matrix for one axis. Figure 6.5 shows the comparison between these two methodologies. Direct inverse matrix method and linear equation solver method show identical polarizability tensor matrix.

119
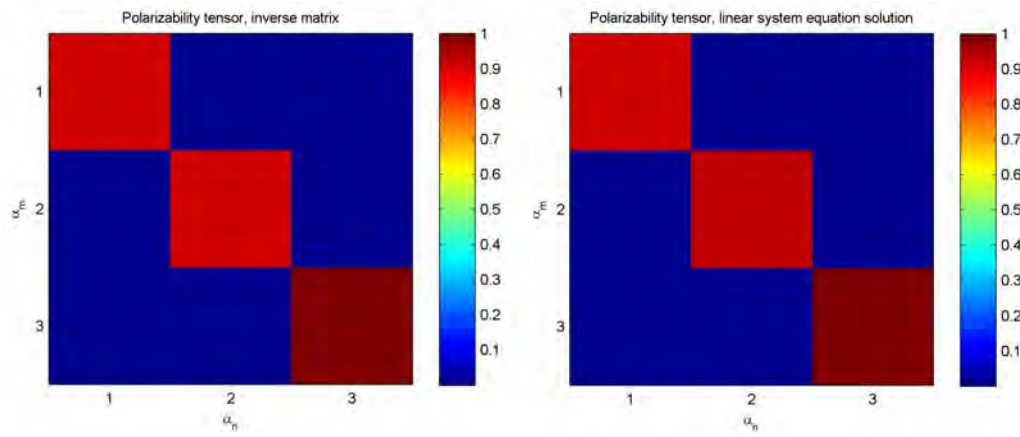
Figure 6.5. Polarizability tensor matrix comparison between 'inverse matrix method' and 'linear equation solver method'. α_{nm} represents tensor directionality.

6.4   Results

This section will describe 1) how to define rod-shape scatterer, 2) TE/TM mode polarizability dependency on scatterer posture on the surface, and 3) polarizability of a fixed posture scatterer dependency on incident light polarization angle.

In the published papers [72, 74], the TE and TM polarizabilities are constant values given scatterer volume. In other words, ratio between TE and TM mode polarizabilities should be constant, if the volume is same. However, intuitively, if the radius and height ratio within same volume is changed, TE and TM mode polarizabilities should change. Figure 6.6 shows the ratio between TE and TM mode polarizabilities as a function of radius. Height is changed, in order to maintain same volume. The fixed volume is based

on a rod having 100nm radius and 200nm height. Two different refractive indices are tested within water. As shown in the figure, as radius increases, TE mode polarizability increases compared to TM mode polarizability. At certain radius and height ratio, polarizability ratio is also saturated. In addition, the refractive index difference between scatterer and environment affects the TE and TM mode polarizability ratio. Because Figure 6.6 shows saturated polarizability ratio for the rod-shape scatterer, radius 50nm rod-shape is used.
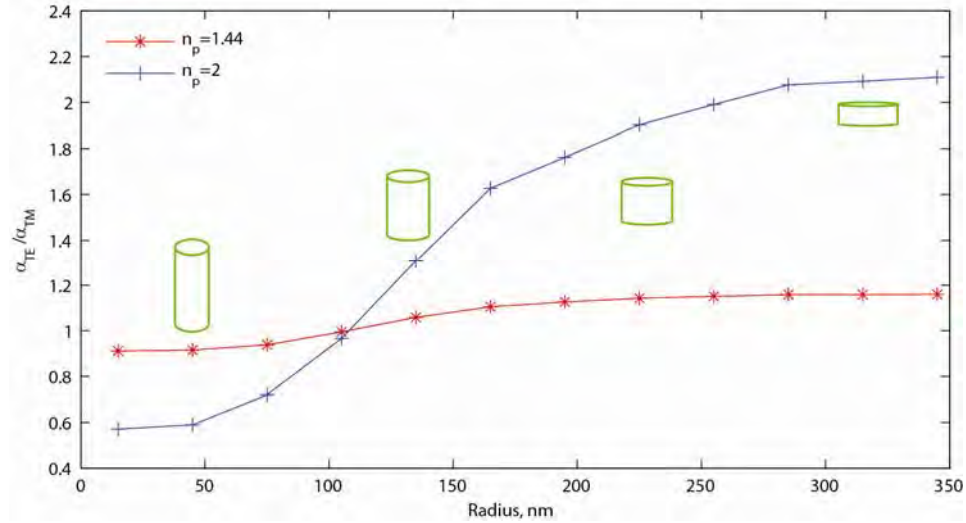
Figure 6.6. Rod-shape definition. By looking to the ratio between TE and TM mode polarizabilities calculated by DDA, scatterer geometry can be identified from rod- to disk-shape. Scatterer refractive index 2 shows more change of the polarizability ratio than its refractive index 1.44. The shapes are for illustration purpose.

The rod-shape scatterer can be standing on or lying down the surface of microresonator, when it enters mode volume. Depending on the posture, polarizability

is different, resulting in different sensing signal, $2g$ and Γ. In real situation, from obtained signals scatterer size is extracted. In other words, if the observed signal is in error, size estimation is in error. In this section, the significance of scatterer posture given incident polarization is investigated. The scatterer refractive index is set to be 1.44 and environment refractive index is 1.33. Figure 6.7 shows TE and TM mode ratio of polarizability, $2g$, and Γ. The resonance mode volume, field strength, and quality factors are obtained from COMSOL based on $D = 50\mu m$ and $d = 5\mu m$ resonator. The particle posture angle is shown on the top left plot. Polarizability ratio between TE and TM is not more than 10 percent difference. Difference of mode splitting amount is up to 20% and additional damping shows about 25% difference.
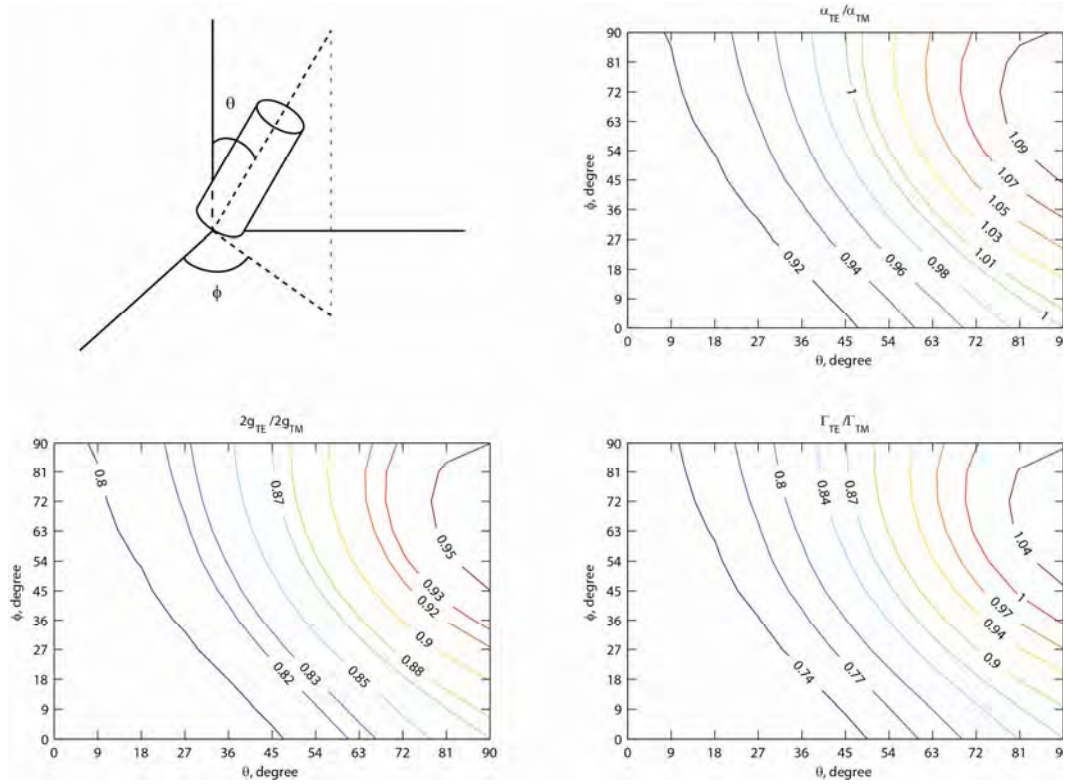
Figure 6.7. Sensing signal dependency on sactterer posture. The schematic shows how the scatterer is interfacing to the resonator surface.

For better understanding, individual components are presented in Figure 6.8. Absolute value of mode splitting difference is <10MHz and its additional damping is <0.2MHz. Therefore, the conclusion solely based on this simulation is hard to reach. The signal difference may be distinguishable depending on noise level.
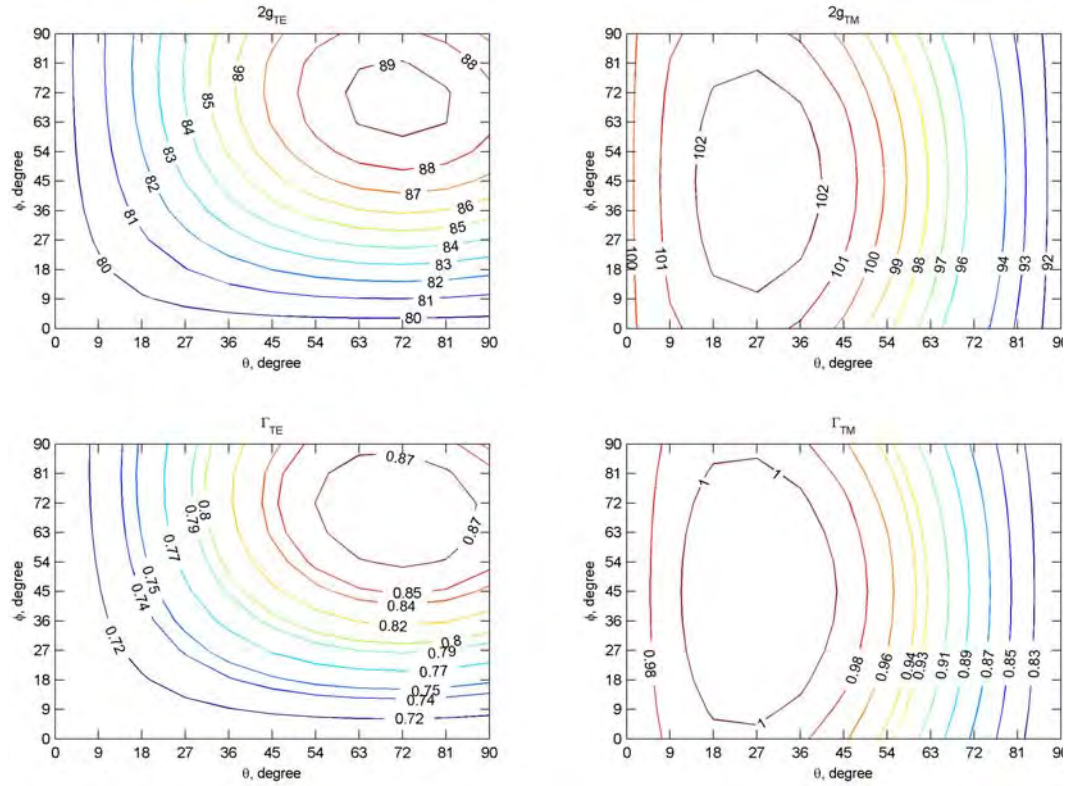
Figure 6.8. Individual sensing signal dependency on sactterer posture. The scatterer posture angle is same as Figure 6.7

Lastly, incident light polarization influence on sensing signal is investigated. In actual situation, it is hard to know the scatterer posture on the resonator. However, it is possible to change incident light polarization, for instance from TE to TM. Thus, in this section, I investigated changes of polarizability, $2g$, and Γ, when incident light polarization is changed. Both rod- and disk-shape scatterers are assumed to be facing their flat surface on the resonator surface. For instance, disk is lying down on the resonator surface. Figure 6.9 shows the changes as a function of polarization angle. The angle is defined as $\mathrm{atan}\left(\frac{TM}{TE}\right)$. As expected, spherical scatterer doesn't show any

changes, while rod- and disk-shape scatterers show monotonic changes. Thus, theoretically, it is possible to distinguish scatterer shape, if the posture is known. However, as mentioned in previous section, experimentally it needs to be confirmed, because noise level is significant role for the sensing signal acquisition, which hinders distinguishing small changes in $2g$, and Γ.
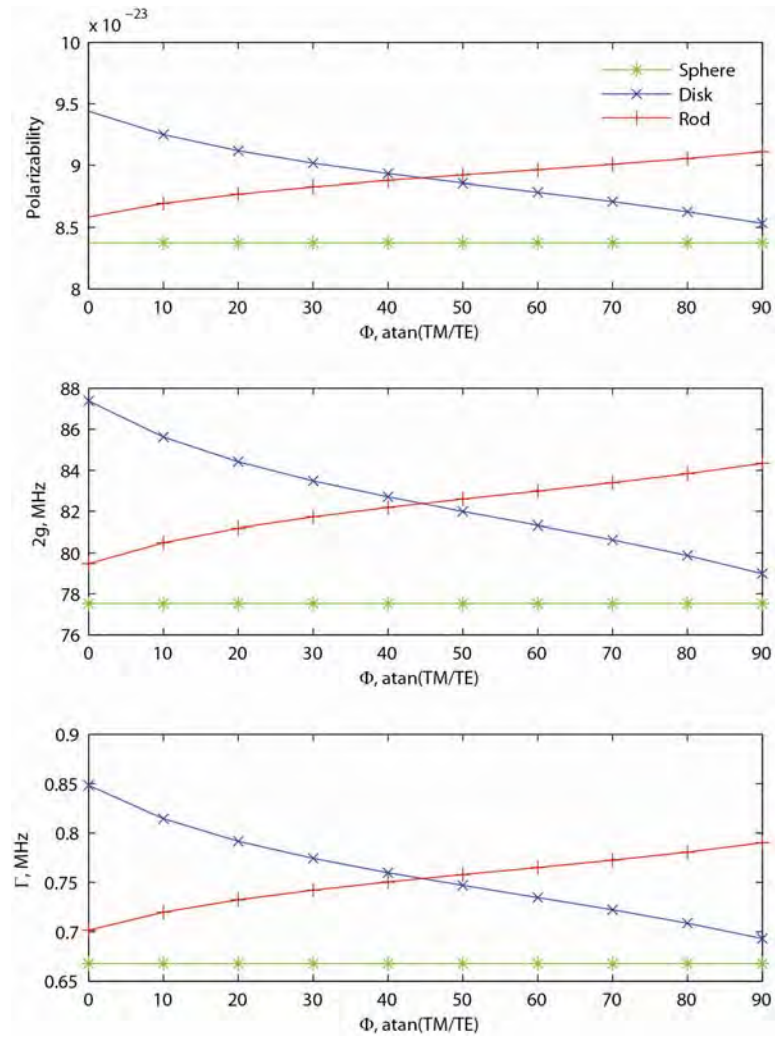

Figure 6.9. Sensing signal dependency on incident light polarization. The postures of scatterers are fixed. Legend on the top figure is applied to all three figures.

6.5   Discussion

Understanding nanoparticle size and shape is comprehensive task, since light polarization and particle geometry are commingled together within the microresonator evanescent field leading to observation of sensing signal. DDA is well known mathematical tool to understand an arbitrary shape sactterer. By using multiple dipoles constructing the target object, DDA calculates dipole moment of the target object and further properties.

In this chapter, I investigated rod-shape scatterer which is considered as hemozoin crystal by using DDA. First, I suggested how to define the rod-shape scatterer based on the ratio between TE and TM mode polarizabilities. Second, polarizabiilty, $2g$, and Γ were studied as a function of the scatterer posture on the microresonator surface with fixed incident light polarization. Third, the same properties were investigated with a fixed scatterer posture for rod-, disk-, and spherical-shape as a function of incident light polarization. Clearly, there are some distinctive features for different posture and geometries. However, the absolute amount of the difference needs to be confirmed through experiment, because system noise level plays a significant role on acquiring sensing signals, $2g$, and Γ . Furthermore, the experiment may not be easily accomplished, because each case has unknown factors. For instance, posture dependent polarizability change assumes known incident light polarization, which is not well-

known inside of mircoresonator. Even though TE and TM polarizations are distinguished in a published work [74], I was not able to replicate their result. However, since this approach can open new research, further experimental investigation would be interesting.

Chapter 7

Summary and future work

This disseration focuses on the demonstration of nanoparticle induced mode splitting capability in water environment. First, multi-particles induced mode splitting is observed by using microtoroid. Second, nanoparticle induced mode splitting is demonstrated with a microsphere and identify optimum condition to observe mode splitting in water. As shown, microtoroid has advantage to observe mode splitting compared to microsphere, because of smaller mode volume given the same quality factor. Thrid, single particle resolution detection and sizing are demonstrated. In this work, synthetic hemozoin crystal also induces mode splitting. Lastly, in order to understand scatterer optical property, DDA is employed. By using DDA, scatterer polarizability in various conditions is studied.

Impact of this work is to open new sensing flatform for biosensing and chemical sensing. The main difficulty of this experiment is to optimize resonator size, resonator quality, nanoparticle size, and nanoparticle refractive index.

Futher works might be selectivity sensing, high refractive index resonator development, and integrated microfluidics platform development. I have tried to functionalize the microresonator surface for the selectivity sensing. However, quality factor degradation

hinders sensing experiment. Thus, if the resonator can retain photons better after the functionalization process, the quality factor will be remained high enough to perform sensing experiment in water. To prove this, silicon nitride microtoroid was fabricated. However, reflow process didn't work as silica microtoroid. All the silicon nitride disk becomes illegular shape after shaning CO_2 laser. Lastly, the sensing platform is not close system. Microfludic is not well controlled. If the sensing platform is closed and integrated system, sensing will be more accurate and well controlled.

Another way of selectivity sensing experiment to be realized is to Raman spectroscopy. For instance, better understanding of hemozoin crystal can be realized cavity enhanced Raman spectrum measurement. Figure 7.1 shows a preliminary result of hemozoin Raman spectrum. The spectrum is measured through free space optics Raman spectroscopy with 514nm laser. The spectrum is quite similar to reported ones, $1367cm^{-1}$, $1576cm^{-1}$, and $1628cm^{-1}$. However, shorter range small peaks are hard to be defined [84]. Reference is silica microsphere Raman spectrum. Microsphere is used for better focusing, no resonance effect. Raman is measured first without hemozoin, 5 times. Then, the microsphere is dipped in the hemozoin solution, and measured Raman spectrum of the dipped microsphere (N=5). Since each measurement intensity is different (for both baseline microsphere and hemozoin solution dipped microsphere Raman measurements), it is normalized with its maximum. Then the five trials were averaged. Finally, Matlab function 'smooth' is used for low pass filtering. If we can utilize our cavity as an enhancement source, low concentration or single crystal level Raman sepctrum might be able to be measured.
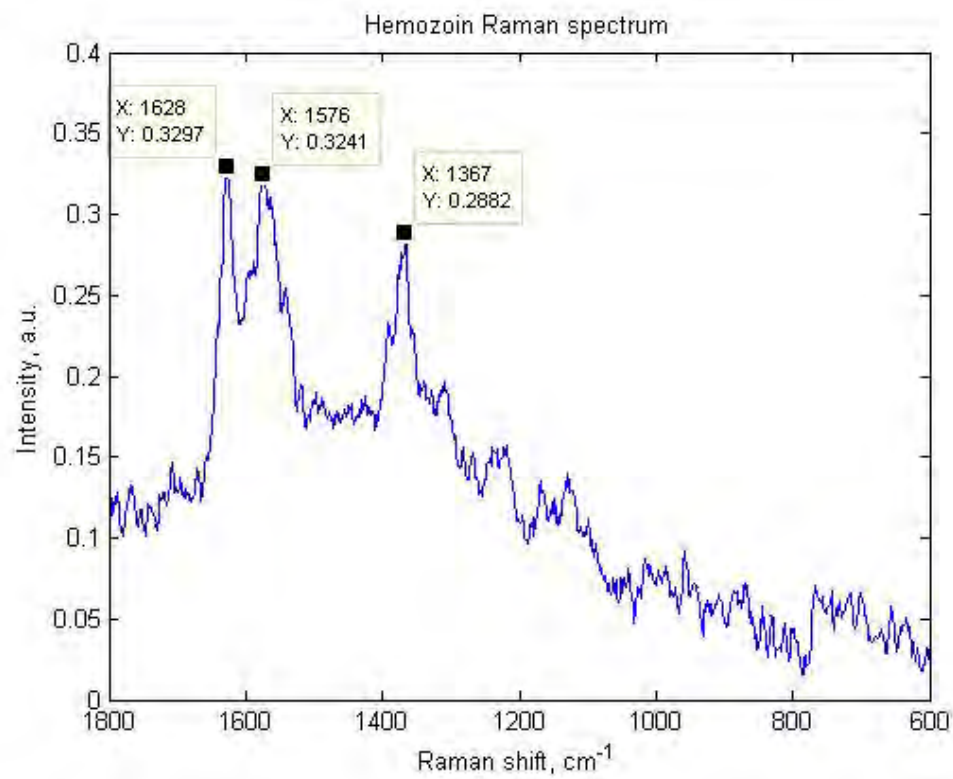
Figure 7.1. Hemozoin crystal Raman spectrum.

With all these improvements, I expect new bio- and chemical-sensing experiments reveal important scientific findings.

References

[1] X. D. Fan, I. M. White, S. I. Shopoua, H. Y. Zhu, J. D. Suter, and Y. Z. Sun, "Sensitive optical biosensors for unlabeled targets: A review," *Analytica Chimica Acta*, vol. 620, pp. 8-26, 2008.

[2] W. Min, C. W. Freudiger, S. Lu, and X. S. Xie, "Coherent nonlinear optical imaging: beyond fluorescence microscopy," *Annu Rev Phys Chem*, vol. 62, pp. 507-30, 2011.

[3] F. Vollmer, S. Arnold, and D. Keng, "Single virus detection from the reactive shift of a whispering-gallery mode," *Proceedings of the National Academy of Sciences of the United States of America*, vol. 105, pp. 20701-20704, 2008.

[4] J. W. Lichtman and J. A. Conchello, "Fluorescence microscopy," *Nat Methods*, vol. 2, pp. 910-9, 2005.

[5] J. Hihath, B. Xu, P. Zhang, and N. Tao, "Study of single-nucleotide polymorphisms by means of electrical conductance measurements," *Proc Natl Acad Sci U S A*, vol. 102, pp. 16979-83, 2005.

[6] J. Homola, "Present and future of surface plasmon resonance biosensors," *Anal Bioanal Chem*, vol. 377, pp. 528-39, 2003.

[7] M. Alvarez, A. Calle, J. Tamayo, L. M. Lechuga, A. Abad, and A. Montoya, "Development of nanomechanical biosensors for detection of the pesticide DDT," *Biosens Bioelectron*, vol. 18, pp. 649-53, 2003.

[8] F. Vollmer and S. Arnold, "Whispering-gallery-mode biosensing: label-free detection down to single molecules," *Nature Methods*, vol. 5, pp. 591-596, 2008.

[9] L. Rayleigh, "The problem of the whispering gallery," *Philosophical Magazine*, pp. 1001-1004, 1910.

[10] G. Mie, "Beitrage zur Optik truber Medien, speziell kolloidaler Metallosungen," *Annalen der Physik*, vol. 330, pp. 377-445, 1908.

[11] V. B. Braginsky, M. L. Gorodetsky, and V. S. Ilchenko, "Quality-Factor and Nonlinear Properties of Optical Whispering-Gallery Modes," *Physics Letters A*, vol. 137, pp. 393-397, 1989.

[12] M. Soltani, S. Yegnanarayanan, and A. Adibi, "Ultra-high Q planar silicon microdisk resonators for chip-scale silicon photonics," *Optics Express*, vol. 15, pp. 4694-4704, 2007.

[13] D. K. Armani, T. J. Kippenberg, S. M. Spillane, and K. J. Vahala, "Ultra-high-Q toroid microcavity on a chip," *Nature*, vol. 421, pp. 925-928, 2003.

[14] Q. Xu, D. Fattal, and R. G. Beausoleil, "Silicon microring resonators with 1.5\mum radius," *Optics Express*, vol. 16, pp. 4309-4315, 2008.

[15] I. M. White, H. Oveys, and X. Fan, "Liquid-core optical ring-resonator sensors," *Optics Letters*, vol. 31, pp. 1319-1321, 2006.

[16] M. Sumetsky, Y. Dulashko, and R. S. Windeler, "Demonstration of the Optical Microbubble Resonator," presented at Conference on Lasers and Electro-Optics, 2010.

[17] L. He, "Whispering Gallery Mode Microresonators for Lasing and Single Nanoparticle Detection," *Washington university in St.Louis, Electrical engineering department Ph. D. dissertation*, 2011.

[18]   B. E. Little, S. T. Chu, H. A. Haus, J. Foresi, and J. P. Laine, "Microring resonator channel dropping filters," *Lightwave Technology, Journal of*, vol. 15, pp. 998-1005, 1997.

[19]   J. Zhu, S. K. Ozdemir, Y. F. Xiao, L. Li, L. He, D. Chen, and L. Yang, "On-chip single nanoparticle detection and sizing by mode splitting in an ultrahigh-Q microresonator," *Nature Photonics*, vol. 4, pp. 46-49, 2010.

[20]   Y. Okawachi, K. Saha, J. S. Levy, Y. H. Wen, M. Lipson, and A. L. Gaeta, "Octave-spanning frequency comb generation in a silicon nitride chip," *Optics letters*, vol. 36, pp. 3398-3400, 2011.

[21]   L. Fan, J. Wang, H. Shen, L. T. Varghese, B. Niu, J. Ouyang, and M. Qi, "A CMOS compatible microring-based on-chip isolator with 18dB optical isolation," presented at Frontiers in Optics, 2010.

[22]   K. J. Vahala, "Optical microcavities," *Nature*, vol. 424, pp. 839-846, 2003.

[23]   T. J. Kippenberg, "Nonlinear Optics in Ultra-high-Q Whispering-Gallery Optical Microcavities," *California Institute of Technology, Applied Physics, Ph. D. dissertation*, 2004.

[24]   B. E. Little, J.-P. Laine, and H. A. Haus, "Analytic theory of coupling from tapered fibers and half-blocks into microsphere resonators," *Lightwave Technology, Journal of*, vol. 17, pp. 704-715, 1999.

[25]   M. L. Gorodetsky, A. D. Pryamikov, and V. S. Ilchenko, "Rayleigh scattering in high-Q microspheres," *Journal of the Optical Society of America B-Optical Physics*, vol. 17, pp. 1051-1057, 2000.

[26]   M. L. Gorodetsky and V. S. Ilchenko, "Optical microsphere resonators: optimal coupling to high-Q whispering-gallery modes," *Journal of the Optical Society of America B*, vol. 16, pp. 147-154, 1999.

[27]   D. W. Vernooy, V. S. Ilchenko, H. Mabuchi, E. W. Streed, and H. J. Kimble, "High-Q measurements of fused-silica microspheres in the near infrared," *Optics Letters*, vol. 23, pp. 247-249, 1998.

[28]   K. Srinivasan, M. Borselli, O. Painter, A. Stintz, and S. Krishna, "Cavity Q, mode volume, and lasing threshold in small diameter AlGaAs microdisks with embedded quantum dots," *Optics Express*, vol. 14, pp. 1094-1105, 2006.

[29]   S. M. Spillane, T. J. Kippenberg, K. J. Vahala, K. W. Goh, E. Wilcut, and H. J. Kimble, "Ultrahigh-Q toroidal microresonators for cavity quantum electrodynamics," *Physical Review A*, vol. 71, pp. 013817, 2005.

[30]   E. M. Purcell, "Proceedings of the American Physical Society," *Physical Review*, vol. 69, pp. 674, 1946.

[31]   A. Yariv, "Universal relations for coupling of optical power between microresonators and dielectric waveguides," *Electronics Letters*, vol. 36, pp. 321-322, 2000.

[32]   S. Schiller, "Asymptotic expansion of morphological resonance frequencies in Mie scattering," *Applied Optics*, vol. 32, pp. 2181-2185, 1993.

[33]   S. Arnold, S. I. Shopova, and S. Holler, "Whispering gallery mode bio-sensor for label-free detection of single molecules: thermo-optic vs. reactive mechanism," *Optics Express*, vol. 18, pp. 281-287, 2010.

[34]   J. Homola, "Surface plasmon resonance sensors for detection of chemical and biological species," *Chem Rev*, vol. 108, pp. 462-93, 2008.

[35]   T. Lu, H. Lee, T. Chen, S. Herchak, J. H. Kim, S. E. Fraser, R. C. Flagan, and K. Vahala, "High sensitivity nanoparticle detection using optical microcavities," *Proceedings of the National Academy of Sciences of the United States of America*, vol. 108, pp. 5976-5979, 2011.

[36]   A. Mazzei, S. Goetzinger, L. D. Menezes, G. Zumofen, O. Benson, and V. Sandoghdar, "Controlled coupling of counterpropagating whispering-gallery modes by a single Rayleigh scatterer: A classical problem in a quantum optical light," *Physical Review Letters*, vol. 99, pp. 173603, 2007.

[37]   J. D. Jackson, *Classical Electrodynamics*: Wiley, 1998.

[38]   S. J. Adams, *Electromagnetic Theory*: Adams Press, 2008.

[39]   D. S. Weiss, V. Sandoghdar, J. Hare, V. Lefevreseguin, J. M. Raimond, and S. Haroche, "Splitting of High-Q Mie Modes Induced by Light Backscattering in Silica Microspheres," *Optics Letters*, vol. 20, pp. 1835-1837, 1995.

[40]   V. S. Ilchenko and M. L. Gorodetsky, "Thermal Nonlinear Effects in Optical Whispering Gallery Microresonators," *Laser Physics*, vol. 2, pp. 1004-1009, 1992.

[41]   W. Kim, S. K. Ozdemir, J. Zhu, L. He, and L. Yang, "Demonstration of mode splitting in an optical microcavity in aqueous environment," *Applied Physics Letters*, vol. 97, pp. 071111, 2010.

[42]   S. Arnold, M. Khoshsima, I. Teraoka, S. Holler, and F. Vollmer, "Shift of whispering-gallery modes in microspheres by protein adsorption," *Optics Letters*, vol. 28, pp. 272-274, 2003.

[43]   A. M. Armani, R. P. Kulkarni, S. E. Fraser, R. C. Flagan, and K. J. Vahala, "Label-free, single-molecule detection with optical microcavities," *Science*, vol. 317, pp. 783-787, 2007.

[44]   A. Yalcin, K. C. Popat, J. C. Aldridge, T. A. Desai, J. Hryniewicz, N. Chbouki, B. E. Little, O. King, V. Van, S. Chu, D. Gill, M. Anthes-Washburn, and M. S. Unlu, "Optical sensing of biomolecules using microring resonators," *Ieee Journal of Selected Topics in Quantum Electronics*, vol. 12, pp. 148-155, 2006.

[45]   H. C. Ren, F. Vollmer, S. Arnold, and A. Libchaber, "High-Q microsphere biosensor - analysis for adsorption of rodlike bacteria," *Optics Express*, vol. 15, pp. 17410-17423, 2007.

[46]   H. Y. Zhu, I. M. White, J. D. Suter, P. S. Dale, and X. D. Fan, "Analysis of biomolecule detection with optofluidic ring resonator sensors," *Optics Express*, vol. 15, pp. 9139-9146, 2007.

[47]   H. Zhu, P. S. Dale, C. W. Caldwell, and X. Fan, "Rapid and Label-Free Detection of Breast Cancer Biomarker CA15-3 in Clinical Human Serum Samples with Optofluidic Ring Resonator Sensors," *Anal. Chem.*, vol. 81, pp. 9858-9865, 2009.

[48]   L. He, S. K. Ozdemir, J. Zhu, and L. Yang, "Scatterer induced mode splitting in poly(dimethylsiloxane) coated microresonators," *Applied Physics Letters*, vol. 96, pp. -, 2010.

[49]   S. Arnold, D. Keng, S. I. Shopova, S. Holler, W. Zurawsky, and F. Vollmer, "Whispering gallery mode carousel-a photonic mechanism for enhanced nanoparticle detection in biosensing," *Opt Express*, vol. 17, pp. 6230-8, 2009.

[50]   J. Zhu, S. K. Ozdemir, L. He, D. Chen, and L. Yang, "Single virus and nanoparticle size spectrometry by whispering-gallery-mode microcavities," *Optics Express*, vol. 19, pp. 16195-16206, 2011.

[51]   L. Chantada, N. I. Nikolaev, A. L. Ivanov, P. Borri, and W. Langbein, "Optical resonances in microcylinders: response to perturbations for biosensing," *Journal of the Optical Society of America B-Optical Physics*, vol. 25, pp. 1312-1321, 2008.

[52]   I. Teraoka and S. Arnold, "Resonance shifts of counterpropagating whispering-gallery modes: degenerate perturbation theory and application to resonator sensors with axial symmetry," *Journal of the Optical Society of America B-Optical Physics*, vol. 26, pp. 1321-1329, 2009.

[53]   S. K. Ozdemir, J. Zhu, L. He, and L. Yang, "Estimation of Purcell factor from mode-splitting spectra in an optical microcavity," *Physical Review A*, vol. 83, pp. 033817, 2011.

[54]   S. I. Shopova, R. Rajmangal, Y. Nishida, and S. Arnold, "Ultrasensitive nanoparticle detection using a portable whispering gallery mode biosensor driven by a periodically poled lithium-niobate frequency doubled distributed feedback laser," *Rev Sci Instrum*, vol. 81, pp. 103110, 2010.

[55]   W. Kim, S. K. Ozdemir, J. Zhu, and L. Yang, "Observation and characterization of mode splitting in microsphere resonators in aquatic environment," *Applied Physics Letters*, vol. 98, pp. 141106, 2011.

[56]   M. Li, H. X. Tang, and M. L. Roukes, "Ultra-sensitive NEMS-based cantilevers for sensing, scanned probe and very high-frequency applications," *Nat Nanotechnol*, vol. 2, pp. 114-20, 2007.

[57]   F. Vollmer, D. Braun, A. Libchaber, M. Khoshsima, I. Teraoka, and S. Arnold, "Protein detection by optical shift of a resonant microcavity," *Applied Physics Letters*, vol. 80, pp. 4057-4059, 2002.

[58]   P. F. Scholl, D. Kongkasuriyachai, P. A. Demirev, A. B. Feldman, J. S. Lin, D. J. Sullivan, Jr., and N. Kumar, "Rapid detection of malaria infection in vivo by laser desorption mass spectrometry," *Am J Trop Med Hyg*, vol. 71, pp. 546-51, 2004.

[59]   T. Hanscheid, C. M. Ribeiro, H. M. Shapiro, and N. G. Perlmutter, "Fluorescence microscopy for tuberculosis diagnosis," *Lancet Infect Dis*, vol. 7, pp. 236-7, 2007.

[60]   C. Coban, M. Yagi, K. Ohata, Y. Igari, T. Tsukui, T. Horii, K. J. Ishii, and S. Akira, "The malarial metabolite hemozoin and its potential use as a vaccine adjuvant," *Allergol Int*, vol. 59, pp. 115-24, 2010.

[61]   J. M. Belisle, S. Costantino, M. L. Leimanis, M. J. Bellemare, D. S. Bohle, E. Georges, and P. W. Wiseman, "Sensitive detection of malaria infection by third harmonic generation imaging," *Biophys J*, vol. 94, pp. L26-8, 2008.

[62]   B. R. Wood, E. Bailo, M. A. Khiavi, L. Tilley, S. Deed, T. Deckert-Gaudig, D. McNaughton, and V. Deckert, "Tip-enhanced Raman scattering (TERS) from

hemozoin crystals within a sectioned erythrocyte," *Nano Lett*, vol. 11, pp. 1868-73, 2011.

[63]   F. Vollmer, S. Arnold, D. Braun, I. Teraoka, and A. Libchaber, "Multiplexed DNA quantification by spectroscopic shift of two microsphere cavities," *Biophysical Journal*, vol. 85, pp. 1974-1979, 2003.

[64]   L. He, K. Ozdemir, J. Zhu, W. Kim, and L. Yang, "Detecting single viruses and nanoparticles using whispering gallery microlasers," *Nature Nanotechnology*, vol. 6, pp. 428-432, 2011.

[65]   S. Pagola, P. W. Stephens, D. S. Bohle, A. D. Kosar, and S. K. Madsen, "The structure of malaria pigment beta-haematin," *Nature*, vol. 404, pp. 307-10, 2000.

[66]   C. Coban, Y. Igari, M. Yagi, T. Reimer, S. Koyama, T. Aoshi, K. Ohata, T. Tsukui, F. Takeshita, K. Sakurai, T. Ikegami, A. Nakagawa, T. Horii, G. Nunez, K. J. Ishii, and S. Akira, "Immunogenicity of whole-parasite vaccines against Plasmodium falciparum involves malarial hemozoin and host TLR9," *Cell Host Microbe*, vol. 7, pp. 50-61, 2010.

[67]   B. Y. H. Liu and D. Y. H. Pui, "A submicron aerosol standard and the primary, absolute calibration of the condensation nuclei counter," *J. Colloid Interface Sci.*, vol. 47, pp. 155-171, 1974.

[68]   E. O. Knutson and K. T. Whitby, "Aerosol classification by electric mobility: apparatus, theory, and applications," *J. Aerosol Sci.*, vol. 6, pp. 443-451, 1975.

[69]   J. M. Schurr and K. S. Schmitz, "Dynamic light scattering studies of biopolymers: effects of charge, shape, and flexibility," *Annual Review of Physical Chemistry*, vol. 37, pp. 271-305, 1986.

[70]   W. C. Hinds, "Aerosol technology: properties, behavior, and measurement of airborne particles," 1982.

[71]   Y. Park, M. Diez-Silva, G. Popescu, G. Lykotrafitis, W. Choi, M. S. Feld, and S. Suresh, "Refractive index maps and membrane dynamics of human red blood cells parasitized by Plasmodium falciparum," *Proc Natl Acad Sci U S A*, vol. 105, pp. 13730-5, 2008.

[72]   X. Yi, Y. F. Xiao, Y. Li, Y. C. Liu, B. B. Li, Z. P. Liu, and Q. H. Gong, "Polarization-dependent detection of cylinder nanoparticles with mode splitting in a high-Q whispering-gallery microresonator," *Applied Physics Letters*, vol. 97, 2010.

[73]   I. Teraoka, S. Arnold, and F. Vollmer, "Perturbation approach to resonance shifts of whispering-gallery modes in a dielectric microsphere as a probe of a surrounding medium," *JOSA B*, vol. 20, pp. 1937-1946, 2003.

[74]   M. Noto, D. Keng, I. Teraoka, and S. Arnold, "Detection of protein orientation on the silica microsphere surface using transverse electric/transverse magnetic whispering gallery modes," *Biophysical Journal*, vol. 92, pp. 4466-4472, 2007.

[75]   I. Teraoka and S. Arnold, "Theory of resonance shifts in TE and TM whispering gallery modes by nonradial perturbations for sensing applications," *JOSA B*, vol. 23, pp. 1381-1389, 2006.

[76]   B. K. Wilson, M. R. Behrend, M. P. Horning, and M. C. Hegg, "Detection of malarial byproduct hemozoin utilizing its unique scattering properties," *Opt. Express*, vol. 19, pp. 12190-12196, 2011.

[77]   M. A. Taubenblatt and T. K. Tran, "Calculation of light scattering from particles and structures on a surface by the coupled-dipole method," *J. Opt. Soc. Am. A*, vol. 10, pp. 912-919, 1993.

[78]   E. M. Purcell, Pennypacker, C. R., "Scattering and absorption of light by nonspherical dielectric grains," *The Astrophysical Journal*, vol. 186, pp. 705-714, 1973.

[79]   V. L. Y. Loke, M. Pinar Menguc, and T. A. Nieminen, "Discrete-dipole approximation with surface interaction: Computational toolbox for MATLAB," *Journal of Quantitative Spectroscopy and Radiative Transfer*, vol. 112, pp. 1711-1725, 2011.

[80]   B. T. G. Draine, Jeremy, "Beyond Clausius-Mossotti - Wave propagation on a polarizable point lattice and the discrete dipole approximation," *Astrophysical Journal*, vol. 405, pp. 685-697, 1993.

[81]   B. T. Draine and P. J. Flatau, "Discrete-dipole approximation for scattering calculations," *J. Opt. Soc. Am. A*, vol. 11, pp. 1491-1499, 1994.

[82]   Y. Fung, W. Tsang, and P. Patitucci, "High-resolution data on the geometry of red blood cells.," *Biorheology*, vol. 18, pp. 369, 1981.

[83]   R. Schmehl, B. M. Nebeker, and E. D. Hirleman, "Discrete-dipole approximation for scattering by features on surfaces by means of a two-dimensional fast Fourier transform technique," *J. Opt. Soc. Am. A*, vol. 14, pp. 3026-3036, 1997.

[84]   B. R. Wood, S. J. Langford, B. M. Cooke, F. K. Glenister, J. Lim, and D. McNaughton, "Raman imaging of hemozoin within the food vacuole of *Plasmodium falciparum* trophozoites," *FEBS letters*, vol. 554, pp. 247-252, 2003.